

---

# THE KORI–ULB ICE FLOW MODEL

---

## REFERENCE MANUAL

---



FRANK PATTYN

Contributors: J. Blasco Navarro, V. Coulon, E. Kazmierczak,  
D. Moreno Parada, T. Gregov, O. Raspoet, S. Sun, L. Zipf

Laboratoire de Glaciologie, Université libre de Bruxelles,  
Avenue F.D. Roosevelt 50, B-1050 Brussels, Belgium (Frank.Pattyn@ulb.be)

**Kori–ULB v0.92 — September 18, 2025**



***kori*** (*noun*):

1. ice (Japanese)
2. movement (Maori)
3. ice flow model of intermediate complexity

## TERMS AND CONDITIONS

The Kori-ULB Ice Flow Model is a 2.5-dimensional finite difference numerical ice flow model of intermediate complexity.

MIT License

Copyright (c) 2017–2025 Frank Pattyn

Permission is hereby granted, free of charge, to any person obtaining a copy of this software and associated documentation files (the "Software"), to deal in the Software without restriction, including without limitation the rights to use, copy, modify, merge, publish, distribute, sublicense, and/or sell copies of the Software, and to permit persons to whom the Software is furnished to do so, subject to the following conditions:

The above copyright notice and this permission notice shall be included in all copies or substantial portions of the Software.

THE SOFTWARE IS PROVIDED "AS IS", WITHOUT WARRANTY OF ANY KIND, EXPRESS OR IMPLIED, INCLUDING BUT NOT LIMITED TO THE WARRANTIES OF MERCHANTABILITY, FITNESS FOR A PARTICULAR PURPOSE AND NONINFRINGEMENT. IN NO EVENT SHALL THE AUTHORS OR COPYRIGHT HOLDERS BE LIABLE FOR ANY CLAIM, DAMAGES OR OTHER LIABILITY, WHETHER IN AN ACTION OF CONTRACT, TORT OR OTHERWISE, ARISING FROM, OUT OF OR IN CONNECTION WITH THE SOFTWARE OR THE USE OR OTHER DEALINGS IN THE SOFTWARE.

Copyright © 2017–2025 Frank Pattyn (Frank.Pattyn@ulb.be)

## Contents

<b>1</b>	<b>Introduction</b>	<b>7</b>
1.1	From f.ETISH to Kori–ULB . . . . .	7
1.2	Reference manual . . . . .	9
<b>2</b>	<b>Installing Kori–ULB</b>	<b>10</b>
2.1	MATLAB® and toolboxes . . . . .	10
2.2	Download Kori–ULB and installation . . . . .	11
<b>3</b>	<b>Model basics: core equations and numerics</b>	<b>13</b>
3.1	Geometry . . . . .	13
3.2	Field equations . . . . .	13
3.2.1	Mass conservation . . . . .	13
3.2.2	Momentum balance . . . . .	14
3.2.3	Conservation of energy . . . . .	14
3.2.4	Constitutive equations and the equation of motion . . . . .	15
3.3	Basic numerical features . . . . .	16
3.3.1	Numerical grid . . . . .	16
3.3.2	SSA velocities . . . . .	16
3.3.3	Ice thickness equation . . . . .	17
<b>4</b>	<b>Getting started with Kori–ULB</b>	<b>18</b>
4.1	Model run in the MATLAB® environment . . . . .	18
4.2	Mandatory control parameters . . . . .	18
4.3	Optional control parameters . . . . .	19
4.4	Example: A square isothermal ice sheet . . . . .	20
<b>5</b>	<b>Input and output data</b>	<b>21</b>
5.1	Input file: <code>infile</code> . . . . .	21
5.2	Output file: <code>outfile</code> . . . . .	22
5.3	Output file: <code>outfile_toto</code> . . . . .	22
5.3.1	Spatially varying variables . . . . .	22
5.3.2	Time-dependent variables . . . . .	27
5.4	Global parameters: file <code>KoriInputParams.m</code> . . . . .	28
<b>6</b>	<b>Ice velocities</b>	<b>30</b>
6.1	Approximations . . . . .	30
6.2	Shallow-Ice Approximation (SIA) . . . . .	30
6.3	HySSA approximation . . . . .	30
6.4	Depth-Integrated Velocity Approximation (DIVA) . . . . .	31
6.5	Shallow-Shelf Approximation (SSA) . . . . .	32
6.6	Control parameters for ice velocity . . . . .	32
6.7	Global parameters for ice velocity . . . . .	33

<b>7 Ice temperature and rheology</b>	<b>34</b>
7.1 Ice temperature . . . . .	34
7.2 Thermomechanical coupling . . . . .	35
7.3 Enthalpy . . . . .	36
7.4 Control parameters for thermodynamics . . . . .	37
7.5 Global parameters for thermodynamics . . . . .	38
7.6 Example: a square thermomechanically-coupled ice sheet . . . . .	39
<b>8 Basal sliding and subglacial conditions</b>	<b>41</b>
8.1 Regularized Coulomb friction and Weertman law . . . . .	41
8.2 Effective pressure at the ice sheet base . . . . .	42
8.2.1 Height above buoyancy . . . . .	42
8.2.2 Subglacial water film . . . . .	43
8.2.3 Sliding related to water flux . . . . .	44
8.2.4 Effective pressure in till . . . . .	44
8.3 Efficient and inefficient basal hydrology on hard and soft beds . . . . .	45
8.4 Control parameters for basal sliding and hydrology . . . . .	48
8.5 Global parameters for basal sliding and hydrology . . . . .	49
<b>9 Calving, hydrofracturing, sub-shelf pinning and damage</b>	<b>51</b>
9.1 Preamble . . . . .	51
9.2 Description . . . . .	51
9.2.1 Crevasse-Depth Calving Law . . . . .	51
9.2.2 Divergence-based Calving Law . . . . .	53
9.2.3 Von Mises Calving Law . . . . .	53
9.2.4 Thickness-dependent Calving Law . . . . .	53
9.3 Control parameters for calving . . . . .	53
9.4 Global parameters for calving . . . . .	55
<b>10 Glacial Isostatic Adjustment (GIA)</b>	<b>56</b>
10.1 Bedrock deformation for a plate with constant thickness . . . . .	56
10.2 Plate with constant thickness on a viscous substratum . . . . .	57
10.3 Plate with spatially-varying thickness . . . . .	58
10.4 Time-dependent bedrock response . . . . .	58
10.5 Geoid changes . . . . .	59
10.6 Control parameters for GIA and geoid changes . . . . .	59
10.7 Global parameters for GIA and geoid changes . . . . .	61
<b>11 Grounding-line flux condition for power-law sliding</b>	<b>62</b>
11.1 Description . . . . .	62
11.2 Control parameters for grounding-line flux . . . . .	63
<b>12 Model initialization</b>	<b>64</b>
12.1 Methodology . . . . .	64
12.2 Control parameters for optimization . . . . .	65
12.3 Global parameters for optimization . . . . .	65
12.4 Example: Initialization of the Antarctic ice sheet . . . . .	66

<b>13 Atmospheric forcing</b>	<b>70</b>
13.1 Parameterisations of the near-surface air temperature and the precipitation rate using a scalar temperature offset . . . . .	70
13.2 Reading atmospheric boundary conditions from files . . . . .	71
13.3 Positive Degree Day (PDD)-based melt-and runoff scheme . . . . .	71
13.4 Control parameters for atmosphere forcing . . . . .	74
13.5 Forcing parameters for atmosphere forcing . . . . .	77
13.6 Global parameters for atmosphere forcing . . . . .	78
<b>14 Ocean forcing</b>	<b>80</b>
14.1 Sub-shelf melting . . . . .	80
14.1.1 Simple parameterizations . . . . .	80
14.1.2 Non-local melt-rate parametrization (ISMIP6) . . . . .	81
14.1.3 The PICO ocean-coupler model . . . . .	81
14.1.4 PICOP and plume model . . . . .	84
14.2 Scalar ocean temperature offset . . . . .	85
14.3 Reading oceanic boundary conditions from files . . . . .	85
14.4 Imposing a sea-level offset . . . . .	86
14.5 Control parameters for ice-ocean interaction . . . . .	86
14.6 Forcing parameters for ice-ocean interactions . . . . .	87
14.7 Global parameters for ice-ocean interaction . . . . .	89
<b>15 Basins and synthetic experiments</b>	<b>91</b>
15.1 Basin modelling . . . . .	91
15.2 Synthetic geometries . . . . .	91
15.3 Control parameters for basins and synthetic experiments . . . . .	93
15.4 Global parameters for basins and synthetic experiments . . . . .	93
<b>16 Publications involving Kori–ULB and f.ETISH</b>	<b>94</b>
<b>References</b>	<b>97</b>

# 1 Introduction

## 1.1 From f.ETISh to Kori–ULB

Kori–ULB is an ice flow model applicable to ice sheets and glaciers on Earth (both land-terminating and marine ice sheets), as well as ice masses on other planets (such as the Martian North Pole Layered Deposits). It reduces the three-dimensional nature of ice sheet flow and its dynamics to a two-dimensional problem, while keeping the essential characteristics of ice sheet and ice stream flow<sup>1</sup>. Kori–ULB is the follow-up of f.ETISh (fast Elementary Thermomechanical Ice Sheet model; Pattyn, 2017). While f.ETISh was essentially designed for large-scale simulations of the Antarctic ice sheet (Pattyn, 2017; Bulthuis et al., 2019; Coulon et al., 2021), it has been extended to high-resolution simulations of glacier flow, specific drainage basins of ice sheets and specific ice geometries, such as MISMIP3d (Pattyn et al., 2013) and MISMIP+ (Cornford et al., 2020). Furthermore, the model has recently been coupled to ocean and atmosphere models (Pelletier et al., 2021). All these features are neither ‘Elementary’ nor ‘fast’, which solicited a change in name for the model. Compared to the initial version of f.ETISh (Pattyn, 2017), several improvements have been made and extensions have been implemented, the most important are listed below:

1. The temperature field within the ice sheet can also be calculated using the enthalpy method, which accurately solves for the cold-temperate transition surface (Raspoet and Pattyn, 2025).
2. Besides the Shallow-Shelf Approximation (SSA) and hybrid flow model (combined SSA and Shallow-Ice Approximation), the Depth-Integrated-Viscosity Approximation (DIVA) has been implemented (Goldberg, 2011; Lipscomb et al., 2019; Robinson et al., 2022). This allows for the calculation of the three-dimensional velocity field that is coupled to the temperature and enthalpy calculation.
3. To facilitate the integration of the Earth-system model output with ice sheet models, several sub-shelf melt models have been implemented, such as PICO (Potsdam Ice-shelf Cavity mOdel; Reese et al., 2018a) that links far-field ocean temperature and salinity to sub-shelf melting via a box model of overturning circulation within ice-shelf cavities (Olbers and Hellmer, 2010). Furthermore, the plume parametrization (Lazeroms et al., 2018, 2019) has been implemented as well as its combination with PICO, called PICOP (Pelle et al., 2019).
4. Kori–ULB can easily be forced with atmospheric and oceanic output from General and/or Regional Circulation Models as used in ISMIP6 (Seroussi et al., 2020; Edwards et al., 2021). Coupling with atmosphere and ocean models has been done recently (Pelletier et al., 2021).
5. A revised Positive Degree Day (PDD) model has been developed (Coulon et al., 2023).
6. Basal sliding has been significantly improved through the implementation of a general sliding law, based on regularized Coulomb friction (Gagliardini et al., 2007; Joughin et al., 2019; Zoet and Iverson, 2020). This allows to control a higher plasticity of

---

<sup>1</sup>However, thermodynamics (temperature and enthalpy) are calculated in three dimensions, as vertical diffusion and advection are main characteristics.

the fast-flowing outlet glaciers, while keeping a power-law relationship (Weertman-type sliding law) for slower-moving ice. The standard Weertman and Budd (including effective pressure) sliding laws are equally represented.

7. Subglacial hydrology has been implemented through subglacial water flow based on a thin water film and a porous water model in subglacial till (Kazmierczak et al., 2022). Subglacial hydrology for hard and soft beds has been introduced that is also capable of switching from efficient to inefficient drainage (Kazmierczak et al., 2024).
8. Calving and hydrofracturing result in a dynamic boundary for floating ice shelves in contact with the ocean. A few common calving laws have been implemented (Pollard and DeConto, 2012a), as well as Von Mises calving. A LSF (Level Set Function) has been introduced to evolve the calving front.
9. Ice sheet and ice shelf damage has been introduced following the Continuum Damage Model (CDM) developed by Sun et al. (2017). This model establishes a direct link between the amount of damage and ice viscosity, as the propagation of damage reduces the ice viscosity through Glen's flow law, leading to faster ice flow.
10. Changes in the geoid due to mass changes of ice sheets are taken into account, leading to non-uniform sea level changes that may impact grounding-line stability. The standard bedrock adjustment based on an elastic lithosphere and relaxed asthenosphere (ELRA-model) has been extended to spatially varying characteristics of both lithosphere effective thickness and mantle viscosity (Coulon et al., 2021).
11. Ice sheet model initialization has been improved with a two-step method, allowing to optimize basal melt rates underneath ice shelves, akin to optimizing basal sliding coefficients, to keep the ice sheet in steady-state (Bernales et al., 2017).
12. Model experiments are not limited to a full ice sheet, but can be done at high (10–1000 m) spatial resolutions by simulating separate drainage basins of ice sheets. As such, Kori–ULB allows for a direct comparison to high-resolution models, such as ISSM (Larour et al., 2012), BISICLES (Cornford et al., 2013), or Elmer/Ice.
13. A few specific boundary conditions at the edge of the domain have been introduced to cope with specific idealized experiments, such as MISMIP+ and a domain with two symmetry axes to reduce computational cost for idealized experiments at high spatial and temporal resolution.

Kori–ULB can be applied to any ice mass, which has been done for extraterrestrial ice (Mars NPLD), glaciers (McCall, Alaska, USA), the Greenland ice sheet, Pine Island and Thwaites Glaciers, and several idealized geometries.

## 1.2 Reference manual

This Reference Manual gives examples of how to run Kori–ULB using publicly-available data for the Greenland and Antarctic ice sheets, and a number of idealized cases. It documents all the Kori–ULB options and configuration parameters. It also summarizes the continuum models used by Kori–ULB.

### WARNING

Kori–ULB is an ongoing research project from the Laboratoire de Glaciologie at the Université libre de Bruxelles (ULB), Brussels, Belgium. Ice sheet modelling requires many choices. Please do not trust the results of Kori–ULB or any other ice sheet model without a fair amount of exploration. Also, do not expect all your questions to be answered here. Ice sheet modelling requires patience, a lot of patience. Do not expect that in a couple of hours you will be able to run a fully-fledged high-resolution ice sheet model with complex atmosphere and ocean forcing. A step-by-step approach, starting from simple and idealized experiments and gradually adding complexity to the model run is the most appropriate. Since the development of Kori–ULB lacks dedicated funding, technical support for Kori–ULB is therefore limited.

## 2 Installing Kori–ULB

### 2.1 MATLAB® and toolboxes

The Kori–ULB model is built in MATLAB® and makes use of standard MATLAB® toolboxes. You will need to have MATLAB® installed on your computer or mainframe and the code works with MATLAB® versions from R2016b onward. With a standard MATLAB® version it is possible to run most of the experiments. However, additional toolboxes are needed when you use the following subroutines in Kori–ULB:

1. *Signal Processing Toolbox*: this toolbox is needed for the Elastic Lithosphere–Relaxed Astenosphere (ELRA) model for bedrock adjustment with a constant effective lithosphere thickness, as it employs the `xcorr2` function;
2. *Statistics and Machine Learning Toolbox*: this toolbox is used with ice shelves for outlining and identifying the different ice shelves, by making use of the function `bwboundaries`.
3. *Symbolic Math Toolbox*: **Not sure and need to find out where.**
4. *Image Processing Toolbox*: **Not sure need to find out where.**

The complete Kori–ULB model code has been developed at ULB in the framework of several projects, and this development is still ongoing. A few subroutines are developed by others, whom we like to acknowledge here:

1. `crameri`: Suite of scientific, colour-vision deficiency friendly and perceptually-uniform colour maps from Fabio Crameri's scientific colourmaps, version 8.0 (<https://www.fabiocrameri.ch/colourmaps/>), that include all readers and significantly reduce visual errors. Code developed by Chad Greene (<http://www.chadagreene.com> and <https://nl.mathworks.com/matlabcentral/fileexchange/68546-crameri-perceptually-uniform-scientific-colormaps>).
2. `convnfft` and `conv2fft`: As opposed to Matlab CONV, CONV2, and CONVN implemented as straight forward sliding sums, CONVNFFT uses Fourier transform (FT) convolution theorem, i.e., FT of the convolution is equal to the product of the FTs of the input functions. Developed by Bruno Luong (<https://nl.mathworks.com/matlabcentral/fileexchange/24504-fft-based-convolution>).
3. `imagescn`: This function provides a quick and easy way to use `imagesc` where NaN pixels are transparent. Developed by Chad Greene (<http://www.chadagreene.com> and <https://nl.mathworks.com/matlabcentral/fileexchange/61293-imagescn>).

All other code/subroutines has been developed over the years by ULB.

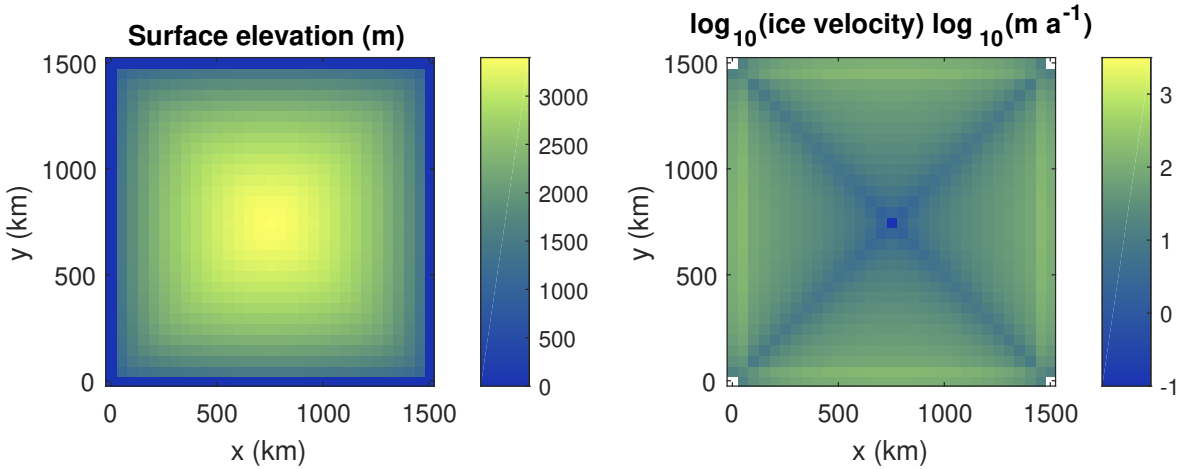


Figure 1: Basic output figure of the simple square ice sheet model. The left panel shows the change in ice thickness (starting from zero thickness). The right panel displays a logarithmic plot of the ice velocities.

## 2.2 Download Kori–ULB and installation

The Kori–ULB model files in MATLAB® can be downloaded from <https://github.com/FrankPat/Kori-ULB>. Unzip the directory of the version/branch you need to your computer in a directory of your choice. The basic model scripts are `KoriModel.m` and `KoriInputParams.m`, as well as the subdirectory subroutines. In order to call the model from any working directory, add the directory of `KoriModel.m` and its subdirectories to the MATLAB® path (In 'Home', select 'Set Path', select the directory where you unzipped the model scripts and select 'Add with Subfolders ...'). To test whether the installation is successful, you can run the model in MATLAB® by typing `KoriModel` at the prompt:

```
>> KoriModel
---Kori-ULB v1.0---
[(c) Frank.Pattyn@ulb.be]
... Running ...
t =      25000.00
... End model run ...
Elapsed time is 51.342856 seconds.
CPU time: 53.75 seconds
>>
```

If the installation is successful, the model runs as shown above for 25 000 years and a graphical window of two panes will pop up (Figure 1) showing the evolution of the surface elevation and velocity field of a square ice sheet on a flat surface. Finally, at the end of the run, a second graphic window will open showing the evolution of the ice volume in time, expressed in terms of contribution to sea level (negative in this case, as the ice sheet builds up; Figure 2). After the model run, there will be two files saved in your directory, i.e., `KoriModelTest.mat` and `KoriModelTest_toto.mat`. Details on the content of those files is given in Section 5.

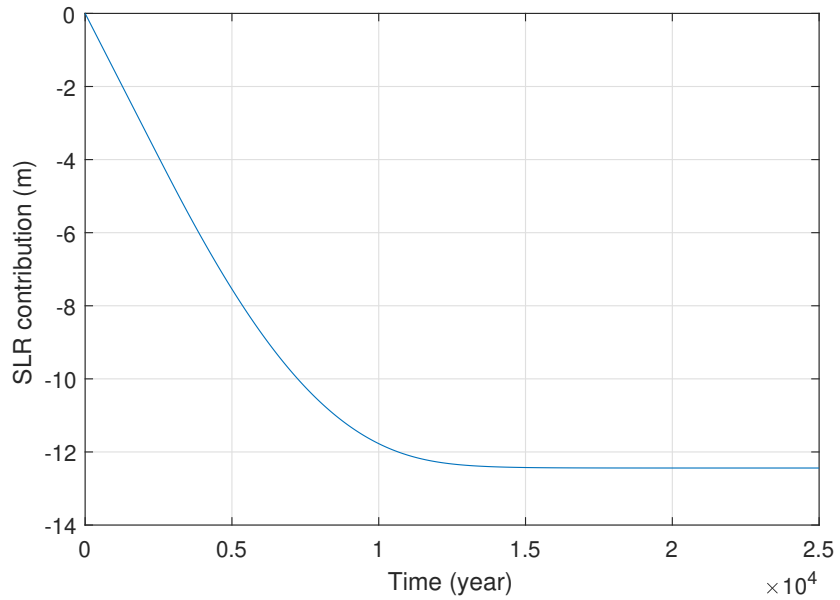


Figure 2: Basic output figure at the end of the model run displaying the ice volume change (above floatation) in terms of sea level contribution as a function of time.

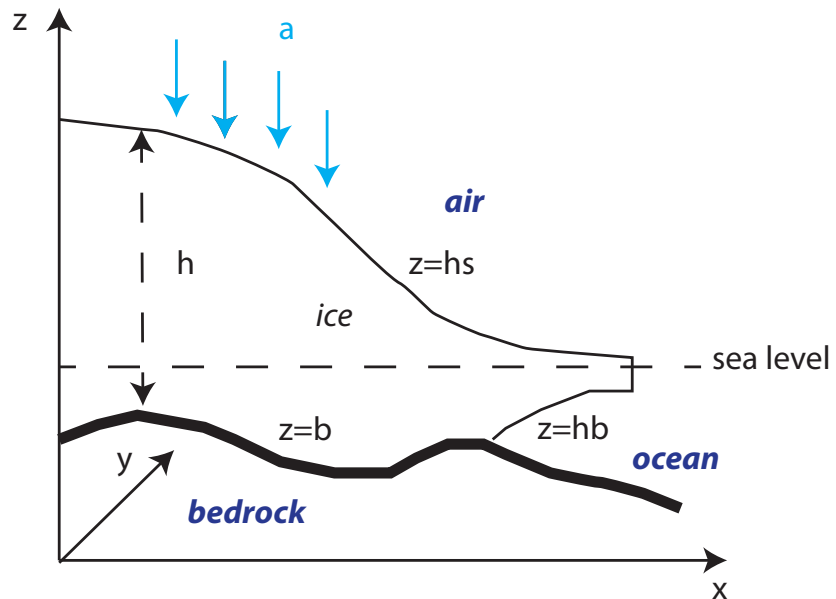


Figure 3: General Cartesian geometry of the Kori–ULB model.

### 3 Model basics: core equations and numerics

#### 3.1 Geometry

The core of the Kori–ULB model consists of diagnostic equations for ice velocities, and three prognostic equations for the temporal evolution of ice thickness, ice temperature and/or enthalpy, and bedrock deformation beneath the ice. Prescribed boundary fields are equilibrium bedrock topography, basal sliding coefficients, geothermal heat flux, and sea level. Present-day mean surface air temperatures and precipitation are generally provided from data assimilation within climate models. Optionally, ablation is determined from a Positive Degree-Day model and sub-shelf melt through simplified ocean circulation models. The Cartesian geometry used is given in Figure 3. For the coupled ice sheet/ice shelf system the surface elevation  $h_s$  is defined as

$$h_s = \max \left[ b + h, \left(1 - \frac{\rho_i}{\rho_s}\right) h + z_{\text{sl}} \right], \quad (1)$$

where  $h$  is the ice thickness,  $b$  is the bedrock elevation,  $z_{\text{sl}}$  is the sea-level height with respect to the chosen datum,  $\rho_i$  and  $\rho_s$  are the ice and seawater density, respectively. It follows that the bottom of the ice sheet equals  $h_b = h_s - h$ , and that  $h_b = b$  holds for the grounded ice sheet.

#### 3.2 Field equations

The Stokes equations then approximate the Navier-Stokes equations for fluid flow, by neglecting momentum advection and inertia terms. Despite these approximations, the flow of ice is in a sense more complicated than the flow of air or water because it is not a Newtonian fluid. In other words, there is a non-linear relationship between the applied stress and the resulting strain rates. Deriving the Stokes equations requires a series of equations that relate conservation laws to the mechanical and thermal properties of the material. These are the conservation of mass, momentum and energy, known as the field equations. In order to link them, they are substituted into the field equations to obtain a system of numerically solvable equations, which is demonstrated below.

##### 3.2.1 Mass conservation

Conservation of mass is described by the continuity equation,

$$\frac{d\rho_i}{dt} + \nabla \cdot (\mathbf{v}\rho_i) = 0 \quad (2)$$

where  $\mathbf{v}$  is the velocity vector. Considering ice as an incompressible material ( $\rho_i = \text{constant}$ ), this can be reduced to the incompressibility condition,

$$\nabla \cdot \mathbf{v} = 0 \quad (3)$$

where  $\mathbf{v} = (u, v, w)$  are the velocity components in  $(x, y, z)$  and from which it follows that

$$w(s) - w(b) = - \int_b^s \nabla \cdot \mathbf{v}_H(z) dz \quad (4)$$

where  $\mathbf{v}_H$  are the components of the horizontal velocity ( $u, v$ ). At the upper and lower surfaces, respectively, kinematic boundary conditions apply, i.e.,

$$w(b) = \frac{\partial b}{\partial t} + \mathbf{v}_H(b) \cdot \nabla b - M \quad (5)$$

$$w(s) = \frac{\partial h_s}{\partial t} + \mathbf{v}_H(h_s) \cdot \nabla h_s - \dot{a} \quad (6)$$

where  $\dot{a}$  (positive in case of accumulation) and  $M$  (positive in case of melt) are the surface and basal mass balance, respectively. Using the Leibniz integration rule, the combination with the kinematic boundary conditions leads to

$$\frac{\partial h}{\partial t} = -\nabla \cdot (\mathbf{v}_H h) + \dot{a} - M \quad (7)$$

For the specific case of calculating ice velocities with the Shallow-ice approximation (SIA), Eq. (7) is written as a diffusion equation, i.e.,

$$\frac{\partial h}{\partial t} = \nabla \cdot (d \nabla h_s) + \dot{a} - M, \quad (8)$$

where  $d$  are diffusion coefficients for the velocity defined as

$$d = -\frac{2}{n+2} A h^{n+2} (\rho_i g)^n |\nabla h_s|^{n-1} - u_b h (\nabla h_s)^{-1} \quad (9)$$

and where  $h_b$  is the bottom of the ice sheet (or the bedrock elevation  $b$  for the grounded ice sheet) and where  $d$  contains both the deformational  $u_d$  and sliding  $u_b$  contributions (Huybrechts, 1992).

### 3.2.2 Momentum balance

Conservation of linear momentum is defined as:

$$\rho_i \frac{d\mathbf{v}}{dt} = \nabla \cdot \boldsymbol{\sigma} - \rho_i \mathbf{g} \quad (10)$$

where  $\boldsymbol{\sigma}$  is the Cauchy stress tensor and  $|\mathbf{g}| = 9.81 \text{ m s}^{-2}$  is the gravitational acceleration. For an ice sheet, the acceleration term (left hand side of Eq. (10)) and the Coriolis force can be safely neglected. For a constant ice density, the momentum balance can be rewritten as

$$\nabla \cdot \boldsymbol{\sigma} + \rho_i \mathbf{g} = 0 \quad (11)$$

The conservation of angular momentum ensures that the Cauchy tensor is symmetric, i.e.  $\boldsymbol{\sigma} - \boldsymbol{\sigma}^T = 0$ , where  $\boldsymbol{\sigma}^T$  is the transpose of  $\boldsymbol{\sigma}$ .

### 3.2.3 Conservation of energy

The final field equation is conservation of energy, which solves the thermodynamics of the ice, i.e.,

$$\rho_i c_p \frac{\partial T}{\partial t} = \nabla \cdot (K \nabla T) - \rho_i c_p \mathbf{v} \nabla T + 2\dot{\epsilon} \boldsymbol{\sigma} \quad (12)$$

where  $K$  is the thermal conductivity of ice,  $c_p$  is the heat capacity of ice, and  $T$  is the ice temperature. This can also be solved using an enthalpy formulation, which is detailed in Section 7.

### 3.2.4 Constitutive equations and the equation of motion

To solve the field equations, a constitutive equation is required, which is the material law equation that relates stress to strain. Glacier ice is a polycrystalline fluid with a stress-dependent viscosity. Due to its structure, there is a non-linear relationship between the applied stress and the resulting deformation, which can be expressed through Glen's flow law. Stress and deformation rates (represented by the strain tensor  $\dot{\epsilon}$ ) are assumed to follow a power law with a proportionality factor that depends on the ice rheology, which in turn depends on local ice temperature, i.e.,

$$\dot{\epsilon} = A\sigma_e^{n-1}\tau \quad (13)$$

where  $\tau$  is the deviatoric stress tensor, which are those stresses remaining once the hydrostatic stresses  $p\mathbf{I}$  are removed from  $\sigma$ ,

$$\tau = \sigma + p\mathbf{I} \quad (14)$$

where

$$p = -\frac{1}{3}\text{tr}\sigma \quad (15)$$

Since ice is considered incompressible, deformation does not depend on the total stress, but the deviation from the isotropic pressure  $p$  (defined positive when compressed).  $\sigma_e$  is the effective stress, defined as the second invariant of the stress tensor  $\sigma$  and defined by (making use of the Einstein summation convention)  $\sigma_e^2 = \frac{1}{2}\sum\tau_{ij}\tau_{ji}$ , or written in terms of tensor components,

$$2\sigma_e^2 = \tau_{xx}^2 + \tau_{yy}^2 + \tau_{zz}^2 + 2(\tau_{xy}^2 + \tau_{xz}^2 + \tau_{yz}^2) \quad (16)$$

$A$  is the temperature-dependent rate factor that obeys an Arrhenius law and may vary over several orders of magnitude within an ice sheet. This is the reason why modelling large ice sheets requires thermomechanical coupling and solving conservation of energy. For simplicity, rather than accuracy, we will continue with a constant value for  $A$ . The power law exponent  $n$  is generally assigned a value of 3. For application of this flow relation in the momentum equation, it is required that  $\tau$  is a function of  $\dot{\epsilon}$ . For this purpose, the inverse of Glen's flow law is used,

$$\tau = 2\eta\dot{\epsilon} \quad (17)$$

where  $\eta$  is the effective viscosity of the ice, which is strain-dependent due to the non-linear nature of the flow law,

$$\eta = \frac{1}{2}A^{-1/n}\dot{\epsilon}_e^{(1-n)/n} \quad (18)$$

where  $\dot{\epsilon}_e$  is the effective strain rate, defined as the second invariant of  $\dot{\epsilon}$ , i.e.,  $\dot{\epsilon}^2 = \frac{1}{2}\sum\dot{\epsilon}_{ij}\dot{\epsilon}_{ji}$ . The components of  $\dot{\epsilon}$  are defined as,

$$\dot{\varepsilon}_{ij} = \frac{1}{2} \left( \frac{\partial v_i}{\partial x_j} + \frac{\partial v_j}{\partial x_i} \right) \quad (19)$$

Substituting Eq. (17) into the simplified momentum balance equation (11), results in the equation of motion,

$$-\nabla p + \nabla \cdot [\eta (\nabla \mathbf{v} + (\nabla \mathbf{v})^T)] + \rho_i \mathbf{g} = 0 \quad (20)$$

In Kori–ULB, the Stokes equations (20) are approximated by the shallow-ice and shallow-shelf equations, which are detailed in Section 6.

### 3.3 Basic numerical features

#### 3.3.1 Numerical grid

The Kori–ULB model uses a finite-difference staggered grid, where horizontal velocities ( $u, v$ ) are calculated on two separate staggered Arakawa C-grids, as is usual for vector fields (Rommelaere and Ritz, 1996), while diffusion coefficients for the ice-sheet equation according to the shallow-ice approximation  $d$  are calculated on an Arakawa B-grid, staggered in both  $x$  and  $y$  direction, since these are scalar quantities (Figure 4). The Kori–ULB model uses no vertical coordinate, except for the temperature field calculation. Here, the scaled vertical coordinate system consists of 11 (default) irregularly-spaced layers, with a minimum layer thickness of  $\Delta\zeta = 0.015$  at the bottom. This way, the number of vertical layers can be greatly reduced, as most of the variability of the vertical temperature profile is situated close to the bed (Huybrechts, 1992).

The Kori–ULB model takes advantage of inherent matrix computation to optimize the model in terms of calculation time, through omission of all *for*-loops (with exception of the time loop). The bulk of computational time is devoted to the solution of the sparse matrix systems, which are natively optimized in MATLAB® using multi-threading.

#### 3.3.2 SSA velocities

The SSA velocity field Eqs. (24–25) is solved as a sparse linear system where both  $u$  and  $v$  component are solved as once in one matrix  $\mathbf{A}$  with size  $(2 \times N_x \times N_y)$  by  $(2 \times N_x \times N_y)$ :

$$\mathbf{A} \cdot \mathbf{u} = \mathbf{b} \quad (21)$$

where  $N_x, N_y$  are the number of grid points in the  $x, y$  direction, respectively. In order to improve both stability and convergence,  $u$  and  $v$  velocities are interleaved (Quiquet et al., 2018), so that  $\mathbf{u}$  alternates between  $u$  and  $v$  values for each grid point in the solution matrix. The velocity field is solved using a stabilized bi-conjugate gradients method, which is also preconditioned and further initialized by the velocity field solution from the previous time step. The use of iterative solvers in combination with preconditioning limits the number of iterations needed to reach convergence. They are considerably faster compared to the direct solution.

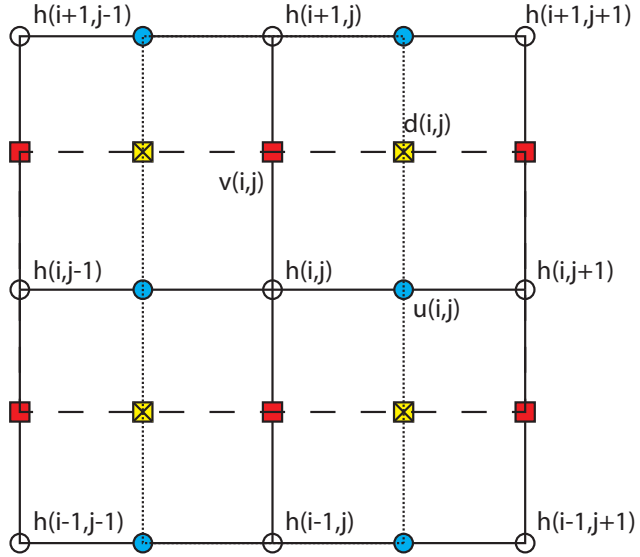


Figure 4: Staggered grids used in the model: the basic grid is the ice-thickness grid (shown in open circles).  $u$  and  $v$  velocities for the ice shelves (and ice streams) are calculated on two different staggered Arakawa C grids (filled circles and squares, respectively). Diffusion coefficients  $d$  in the ice-sheet equation are solved on an Arakawa B grid (crossed squares).

### 3.3.3 Ice thickness equation

A similar solution approach is taken for solving the continuity equation for ice thickness (Payne and Dongelmans, 1997), which was favoured over an Alternating Direct Implicit scheme used in several ice-sheet models (Huybrechts, 1992; Pollard and DeConto, 2012a). To furthermore increase computational stability, upstream differences are employed for SSA velocity gradients in Eq. (7) in combination with an over-implicit Crank-Nicholson scheme (Hindmarsh, 2001; Pattyn, 2006). This allows for the use of larger time steps than nominally would be the case. The Crank-Nicholson scheme is written, as

$$\frac{h_{t+1} - h_t}{\Delta t} = (1 - \omega) \frac{\partial h}{\partial t}|_t + \omega \frac{\partial h}{\partial t}|_{t+1} \quad (22)$$

where  $\partial h / \partial t$  is defined in Eq. (7) and Eq. (8), and where  $\omega = 2.5$  for an over-implicit scheme (1 for a semi-implicit, 0 for an explicit numerical scheme). A preconditioned conjugate gradient method is used for solving the ice sheet/ice shelf continuity equation.

## 4 Getting started with Kori–ULB

### 4.1 Model run in the MATLAB® environment

Kori–ULB is based on two MATLAB® script files, i.e., `KoriModel.m` containing the main model code and subroutines and `KoriInputParams.m` containing the main input parameters and constants, excluding parameters that control the model. A further script is needed that creates a MATLAB® file with all controlling variables to call `KoriModel.m`. The Kori–ULB model is called with the following command line in MATLAB®:

```
KoriModel(infile,outfile,ctr);
```

or

```
KoriModel(infile,outfile,ctr,fc);
```

where `ctr` is a  $1 \times 1$  `struct` containing values and settings of parameters that control the model run, `fc` is a  $1 \times 1$  `struct` with fields containing time-dependent forcing as well as climate forcing control of the model, `infile.mat` is the input file with either the observed ice sheet geometry or the results of a previous model run. The output file `outfile.mat` is similar to the input file in structure and saves all required matrices to produce a follow-up run. Finally, a variable dump file is automatically created after each model run containing all variables of the model run. This file is named `outfile_toto.mat`. Note that `infile.mat` does not need to exist (it can just be replaced by ” in the call no input file is defined — see example below). In that case, all initial field values will be set to default values. Also, `fc` is an optional `struct` field that by default is set to zero (no forcing). More information on this field is given in Section 13.

### 4.2 Mandatory control parameters

The control file is a MATLAB® (.mat) file listing all control parameters necessary to run the model. It can be created with a simple script. Most parameters are set to their default values and should not explicitly be defined. One particularity of the input files is the definition of  $(x, y)$  corresponding to  $(j, i)$  in the numerical code. In other words, the first element of a matrix corresponds to its vertical position, the second element to its horizontal one. It suffices to transpose input data sets to make the visualization of data fully compliant with other models and model code.

`ctr.dt` : time step (years).

`ctr.imax` : number of grid points in the  $y$ -direction.

`ctr.jmax` : number of grid points in the  $x$ -direction.

`ctr.delta` : grid size (m), equal in both  $x$  and  $y$ -directions.

`ctr.nsteps` : number of iterations in time, so that  $(\text{ctr.nsteps} - 1) \times \text{ctr.dt} = \text{total model run time in years}$ .

### 4.3 Optional control parameters

Optional control parameters define the output of the model, how and whether plots are made, and define what domain is considered (full ice sheet, basin, or synthetic experiments).

**ctr.diagnostic :**

- 0** : Normal model run (default);
- 1** : Run model without ice-thickness evolution (all other model components run normally).

**ctr.plotH :**

- 0** : plot changes in surface elevation compared to initial state (default)
- 1** : plot surface elevation
- 2** : plot ice thickness

**ctr.plotGL :**

- 1** : Plot grounding line in output graphs, when grounding line exists (default);
- 0** : No grounding line plotting.

**ctr.restart :**

- 0** : Normal model run (default);
- 1** : Restart from latest dump file (when `ctr.runmode=1` or `ctr.runmode=3`).

**ctr.runmode :**

- 0** : Run model with graphics that are shown every `ctr.snapshot` (default). A dump file is written at the end of the model run. The name of the dump file is `outfile_toto.mat`;
- 1** : Run model with graphics and output dump is written every `ctr.snapshot`. This allows for restarting the model after failure;
- 2** : As in 0 but run without graphics (especially useful when using batch jobs)
- 3** : As in 1 but run without graphics (especially useful when using batch jobs and securing recovery);

**ctr.snapshot** : number of snapshots in time dependency and graphical output; will create `ctr.snapshot` output files when `ctr.timeslice=1`. `snapshot` should preferentially be smaller than 250, since it may increase the number of output files dramatically (limit = 999). Default value = 100.

**ctr.starttime** : Define start time of model run in years. Default=0.

**ctr.timeslice :**

- 0** : no extra output (default);

**1** : will provide extra output for forcing experiments saved sequentially in a file (snapshot times). The variable list is defined by `par.varlist` and consists of a list of 2-D matrices to be saved in each file.

**ctr.YearlyMeans** : Output of yearly mean values, typical for ISMIP experiments. Should only be used with climate forcing data (default=0).

**ctr.SnapList** : Output of yearly values of the 2D fields that are defined in `par.varlist`. Should only be used with climate forcing data (default=0).

#### 4.4 Example: A square isothermal ice sheet

This example is probably the simplest setup of running an ice sheet model. We consider an isothermal ice sheet on a square flat bedrock, forced by a constant surface mass balance, starting from zero ice thickness. Ice deformation is according to the shallow-ice approximation (SIA). The script is given below:

```
% Simple fixed margin experiment for an isothermal ice sheet

ctr.imax=31;
ctr.jmax=31;
ctr.delta=50.e3;
ctr.nsteps=501;
ctr.dt=50.;
ctr.MbConst=0.3;

KoriModel('', 'simple_out', ctr);
```

Basic input is the number of elements in  $x$  and  $y$  (given by `ctr.jmax` and `ctr.imax`, respectively), the spatial resolution  $\Delta$  (m) (`ctr.delta`), the number of iterations (`ctr.nsteps`) and the time step  $\Delta t$  (a) in years (`ctr.dt`). We apply a constant surface mass balance Additional information is given in the input file, where the surface mass balance Mb (m a<sup>-1</sup>) through the parameter `MbConst`, which creates a matrix of the size of the domain filled with constant values (see Section 13). An input file is not used here, so the first argument is kept empty. The output will be written in two files, i.e., `simple_out.mat` and `simple_out_toto.mat`. The latter contains all the variables (dump file) at the end of the model run, while the former contains essential matrix information that is used as input for a follow-up run. Thanks to the exhaustive use of default values for parameters, only a limited amount of data needs to be defined to run a model in its simplest way. This specific run is the same as the one that is obtained by running `KoriModel` without any arguments (test case). Therefore, the same graphic information will be displayed during the run (default), which is shown in Figures 1 and 2.

## 5 Input and output data

### 5.1 Input file: `infile`

`infile` is the name of a .mat input file with following (optional) 2d variables that can be compiled separately: `MASK`, `MASKo`, `H`, `Ho`, `B`, `Bo`, `Bor`, `G`, `stdB`, `Ts`, `Mb`, `Pr`, `Evp`, `To`, `So`, `Db`, `Btau`, `v`, `vx`, `vy`, `lat`, `lon`, `ZB`, where

**MASK** : grounded = 1; floating = 0

Note that when `ctr.shelf=0` and `ctr.schoof=0`, the model domain will be restricted to `MASK=1`, irrespective of whether the bed is below sea level or not. `MASKo` = 0 does not make a difference between ice shelves and open ocean (that is defined through the variable `gMASK`).

**MASKo** : observed `MASK` (invariable in time) and corresponding to `MASK` prior to any simulation. Note that contrary to `MASK`, `MASKo` has a value of 3 for ice shelves and 0 for the ocean.

**H** : ice thickness (m)

**Ho** : observed ice thickness (m), invariable in time

**B** : bedrock elevation (m)

**Bo** : observed bedrock elevation (m), invariable in time. Note that on the borders of the domain, for Antarctic and Greenland configurations, `B` is set to -4000 m to prevent grounding lines to move outside the domain.

**Bor** : original observed bedrock elevation (m), invariable in time (not altered as in `Bo`).

**G** : geothermal heat flux ( $\text{W m}^{-2}$ )

**stdB** : Standard deviation of bedrock variability within a grid cell (based on Bedmap or BedMachine data).

**Ts** : Annual mean surface temperature ( $^{\circ}\text{C}$ ).

**Mb** : Surface mass balance ( $\text{m a}^{-1}$ ). Can be provided directly, or is computed as the balance between precipitation, evaporation and surface runoff, if provided separately.

**Pr** : Precipitation ( $\text{m a}^{-1}$ ). This variable is required when surface mass balance is estimated via a PDD model (see Section 13).

**Evp** : Evaporation ( $\text{m a}^{-1}$ ). Used in conjunction with `Pr`.

**To** : Ocean temperatures on the continental shelf ( $^{\circ}\text{C}$ ).

**So** : Ocean salinity on the continental shelf (PSU).

**Db** : Flexural rigidity of the lithosphere. Filled with constant values corresponding to `par.FlexRigid` when `Db` is not initially defined.

**Btau** : Relaxation time of the asthenosphere. Filled with constant values corresponding to `par.bedrelax` when `Btau` is not initially defined.

**v** : observed surface velocity  $v$ .

**vx** : observed surface velocity  $v$  in  $x$  (on staggered  $u$ -grid)

**vy** : observed surface velocity  $v$  in  $y$  (on staggered  $v$ -grid)

**lat** : Latitude (degrees)

**lon** : Longitude (degrees)

**ZB** : Delineation of drainage basins.

If the input file is non-existent, the model will be initialized with zero matrices of  $H$ ,  $B$ ,  $As$ ,  $stdB$ ,  $Ts$ ,  $Mb$ , and  $tmp$ .  $MASK$  will be set to 1 everywhere, and  $G$  will contain a constant value of geothermal heat flow of  $G=0.042 \text{ W m}^{-2}$ . The extension ‘.mat’ should not be given as part of the name `infile`.

## 5.2 Output file: `outfile`

`outfile` is the name of a .mat output file (same structure as `input`). This file will contain all necessary matrices to be used as an input file for a subsequent experiment. During successive runs, more input will be added, such as the basal melt rate underneath the grounded ice sheet (`Bmelt`), basal sliding coefficients (`As`) and their initial value (`Asor`), the 3d temperature field (`tmp`) or the enthalpy field (`E`), the two components of the horizontal velocity field (`uxsa` and `uysa`), ice damage (`damage`), the subglacial water layer thickness (`Wd`), the subglacial till layer thickness (`Wtil`), as well as the sub-shelf melt and accretion rates with the optimization (`Meltinv`). These variables are produced by the model and used for successive model runs.

## 5.3 Output file: `outfile_toto`

All model data and parameters are stored in a file with the name `outfile_toto.mat`. The extension ‘.mat’ should not be given as part of the name `infile`. For `ctr.snapshot=1`, file names starting from `outfile_000.mat` with an increment of 1 will be created where variables listed in `par.varlist` will be saved. A list of the basic variables that are created within the Kori–ULB model is given below.

### 5.3.1 Spatially varying variables

Spatially-varying parameters are matrices of size `ctr.imax` by `ctr.jmax`. All variables are written out at the end of the model run in the file `output_toto.mat`. The  $x$  and  $y$ -grids correspond to the Arakawa C grid, while the  $d$ -grid corresponds to the Arakawa B grid. The list of variables is, however, not exhaustive.

**A**= Glen’s flow factor (temperature dependent) on the  $H$ -grid. **Ax** and **Ay** is the same variable on the staggered  $u$  and  $v$  grid, respectively, while **Ad** is its value on the staggered  $d$  grid.

**A3d** = Same as A, but in three dimensions and used with the DIVA velocity solver. It employs a different Arrhenius relationship compared to the 2d version of A.

**As** = Initial or optimized sliding parameters  $A_s$  for the power-law sliding law.

**Asf** = Corrected values of  $A_s$  for dependence on temperature, bedrock variability and scaling for the power in the sliding law; Asf is the sliding coefficient that is used in the sliding law. Asfx and Asfy are the values on the staggered  $u$  and  $v$  grid, respectively, while Asfd is its value on the staggered  $d$  grid.

**B** = Bedrock elevation  $B$  (m). Bmx and Bmy is the same variable on the staggered  $u$  and  $v$  grid, respectively.

**B0** = Bedrock elevation  $B$  at the start of the model run (m)

**Bo** = Bedrock elevation  $B$  from original dataset (Bedmap2/BedMachine) (m), but corrected at the edges to reach a bedrock depth of -4000 m to prevent the grounding line to extend beyond the model domain. Bor is the value without that correction (original bedrock data).

**beta2** = Basal friction parameter  $\beta^2$ . For output purposes only, as its values on the staggered  $u, v$  grids is used in the calculation for the velocity field

**bMASK** = Mask for basin model runs. bMASK = 0 corresponds to the area inside the basin; bMASK = 1 represents the grounded area outside the basin. bMASK exists on different grids, i.e., bMASKx, bMASKy, and bMASKm.

**bload** = Bedrock load for isostasy. Only calculated when a bedrock model is selected.

**Bmelt** = Basal melt rate underneath the grounded ice sheet.

**Bn** = Bedrock elevation  $B$  on time step  $t + 1$

**CMB** = Calving rates in the mass balance (m a<sup>-1</sup>)

**CTS<sub>m</sub>** = Lower boundary of the Cold Transition Surface in the enthalpy model.

**CTS<sub>p</sub>** = Upper boundary of the Cold Transition Surface in the enthalpy model.

**d** = Diffusion coefficients of ice sheet equation on staggered  $d$ -grid. These contain sliding and deformation for the SIA model and only deformation for the Hybrid model (SSA+SIA).

**damage** = Spatial damage field of the ice sheet and ice shelf.

**D<sub>b</sub>** = Spatially varying (can be constant) flexural rigidity of the lithosphere

**D<sub>bw</sub>** = Total englacial meltwater drained to the bed (m a<sup>-1</sup>)

**D<sub>fw</sub>** = fraction of drained englacial meltwater for each englacial layer.

**dHdt** = Ice sheet imbalance  $\partial H / \partial t$  (m a<sup>-1</sup>)

**dudx** = Ice flow stretching rate in the  $x$  direction ( $\partial u / \partial x$ )

**dvdy** = Ice flow stretching rate in the  $y$  direction ( $\partial v / \partial y$ )

**dudy** =  $\partial u / \partial y$

**dvdx** =  $\partial v / \partial x$

**E** = 3d matrix of enthalpy

**Epmp** = 3d matrix of enthalpy at pressure melting point

**eta** = effective viscosity in SSA solution.

**etaD** = 3d effective viscosity in DIVA solution.

**Evp** = Evaporation ( $\text{m a}^{-1}$ ).

**f1w** = Subglacial water flux

**FMB** = Vertical cliff melting ( $\text{m a}^{-1}$ )

**G** = Geothermal heat flux ( $\text{W m}^{-2}$ )

**gMASK** = Complete mask for ice sheet-ice shelf-ocean system

- 1:** Grounded ice sheet
- 2:** Last grounded grid point (grounding line)
- 3:** First floating grid point
- 4:** Ice shelf
- 5:** Calving front (last floating grid point, may replace the first floating grid point in absence of ice shelf)
- 6:** Open ocean (covered by `par.SeaIceThickness`)

**gradm** = square of the surface gradients ( $\nabla h_s$ )<sup>2</sup> on staggered  $d$ -grid

**gradmx** = square of the surface gradients ( $\nabla h_s$ )<sup>2</sup> on staggered  $x$ -grid

**gradmy** = square of the surface gradients ( $\nabla h_s$ )<sup>2</sup> on staggered  $y$ -grid

**H** = ice thickness (m).  $H_{mx}$  and  $H_{my}$  are the values on the staggered  $u$  and  $v$  grid, respectively, while  $H_m$  is its value on the staggered  $d$  grid.

**H0** = ice thickness at the start of the model run

**HAF** = Height above floatation (positive for grounded ice; negative for floating ice). The values  $HAF_{mx}$  and  $HAF_{my}$  are those corresponding to the staggered grid in  $x$  and  $y$ , respectively.

**HB** = lower ice boundary; for grounded ice  $h_b = b$

**HB0** = lower ice boundary at the start of the model run

**HB0** = Same as HB0 but for the original data set (Bedmap2/BedMachine)

**he** = Edge ice thickness (for calving; m)

**Hn** = ice thickness (m) on time step  $t + 1$

**Ho** = ice thickness (m) for the original dataset (Bedmap2/BedMachine)

**Ht** = thickness of the temperate ice layer (m); is a boundary conditions for enthalpy

**Hw** = thickness of the water layer (m); is a boundary condition for enthalpy

**LSF** = Level Set Function field

**MASK** = Grounded-non-grounded mask; 1 for grounded ice sheet; 0 otherwise; Note that when **shelf**=0 and **schoof**=0, the model domain will be restricted to **MASK**=1. **MASKmx** and **MASKmy** are the values on the staggered  $u$  and  $v$  grid, respectively.

**MASK0** = Mask at the start of the model run

**MASKo** = MASK for the original dataset (Bedmap2/BedMachine). Note that **MASK**=3 refers to the ice shelves

**Mb** = Surface mass balance (including surface accumulation, ablation, surface melt determined from PDD model, sub-ice shelf melt and calving)

**Mb0** = Surface mass balance (accumulation/ablation) at start of the model run

**Mbend** = Surface mass balance **Mb** at the end of the model run (including all losses, i.e. surface melting with PDD model, sub-shelf melting and calving); At the end of the model run **Mb0** is copied on **Mb**

**Mbm** = Surface mass balance (accumulation/ablation) on staggered  $d$ -grid

**Melt** = Sub-ice shelf melting rate ( $\text{m a}^{-1}$ )

**MeltInv** = Sub-ice shelf melting rate obtained from optimization of sub-hself melt rates ( $\text{m a}^{-1}$ )

**Neff** = Effective pressure at the base of the ice sheet (Pa)

**p** = Power coefficient for shape functions of the horizontal and vertical velocity profiles, taking into account thermomechanical coupling.

**Pr** = Annual precipitation rate (m/a)

**PDD** = Number of positive degree days (degree days)

**pwv** = Subglacial water pressure (Pa)

**r** = Fraction of subglacial sliding/freezing as a function of basal temperature and bedrock variability, so that:  $A_{sf} = (1 - r)A_{sFroz} + A_s r$

**runoff** = Annual runoff rate (m/a)

**S0** = Surface elevation (m) at the start of the model run

**ShelfN** = PICO: ice shelf number

**shMASK** = PICO: ice shelf mask (1 for floating ice)

**signx** = Flow direction in  $x$  (positive/negative)

**signy** = flow direction in  $y$  (positive/negative)

**SLR** = Height of sea level (m)

**Smelt** = Surface melt rate from PDD model ( $\text{m a}^{-1}$ )

**sn** = Surface elevation (m)

**sn0** = Surface elevation (m) from original dataset (Bedmap2/BedMachine)

**So** = Ocean salinity (PSU)

**stdB** = Standard deviation of bedrock variability in each grid cell, based on original Bedmap2/BedMachine data

**taud** = Driving stress on staggered  $d$  grid

**taudxy** = Driving stress on  $H$  grid

**Tb** = Basal temperature ( $^{\circ}\text{C}$ )

**Tbc** = Basal temperature corrected for pressure melting ( $^{\circ}\text{C}$ )

**tmp** = 3d englacial temperature field ( $\text{ctr}.\text{imax} \times \text{ctr}.\text{jmax} \times \text{ctr}.\text{kmax}$ ). Note that this is the only temperature related field that is given in Kelvin!

**To** = Ocean temperature ( $^{\circ}\text{C}$ )

**Ts** = Surface temperature ( $^{\circ}\text{C}$ )

**Ts0** = Surface temperature ( $^{\circ}\text{C}$ ) at the start of the model run

**Tsend** = Surface temperature ( $^{\circ}\text{C}$ ) at the end of the model run; At the end of the model run  $\text{Ts0}$  is copied on  $\text{Ts}$

**u** = vertical mean horizontal velocity ( $\text{m a}^{-1}$ ),  $u = u_s + u_d$  on staggered  $d$ -grid

**ud** = vertical mean deformation al velocity ( $\text{m a}^{-1}$ ) on staggered  $d$  grid

**ub** = sliding velocity ( $\text{m a}^{-1}$ ) on staggered  $d$ -grid

**ux** = vertical mean horizontal velocity in  $x$  direction ( $\text{m a}^{-1}$ ) on staggered  $x$ -grid

**uxssa** = sliding/ice shelf velocity in  $x$  direction ( $\text{m a}^{-1}$ ) on staggered  $x$ -grid

**uxsia** = SIA velocity in  $x$  direction ( $\text{m a}^{-1}$ ) on staggered  $x$ -grid

**uxsch** = Flux-adjusted grounding-line velocity in  $x$  direction ( $\text{m a}^{-1}$ ) on staggered  $x$ -grid  
**uy** = vertical mean horizontal velocity in  $y$  direction ( $\text{m a}^{-1}$ ) on staggered  $y$ -grid  
**uyssa** = sliding/ice shelf velocity in  $y$  direction ( $\text{m a}^{-1}$ ) on staggered  $y$ -grid  
**uysia** = SIA velocity in  $y$  direction ( $\text{m a}^{-1}$ ) on staggered  $y$ -grid  
**uysch** = Flux-adjusted grounding-line velocity in  $y$  direction ( $\text{m a}^{-1}$ ) on staggered  $y$ -grid  
**v** = Observed surface velocity from Rignot et al. (2011) on staggered  $d$ -grid  
**VAF0** = Volume above floatation at start of the model run  
**VAFi** = Volume above floatation  
**vx** = Observed surface velocity in  $x$  direction from Rignot et al. (2011) on staggered  $x$ -grid  
**vy** = Observed surface velocity in  $y$  direction from Rignot et al. (2011) on staggered  $y$  grid  
**wat** = Englacial water content in enthalpy  
**wd** = Subglacial water layer depth (m)  
**Wtil** = Height of subglacial water in porous till (m)  
**X** = Horizontal  $x$  coordinates (km)  
**Y** = Horizontal  $y$  coordinates (km)  
**ZB** = Delineation of basins (e.g., Zwally basins).

### 5.3.2 Time-dependent variables

The following series of variables are produced (or provided) at every time step.

**time** = Time (a)  
**Ag** = Grounded ice sheet area ( $\text{m}^2$ )  
**Af** = Floating ice shelf area ( $\text{m}^2$ )  
**dHdt** = Total ice sheet imbalance ( $\text{m a}^{-1}$ )  
**glflux** = Total grounding-line ice flux ( $\text{m}^3 \text{ a}^{-1}$ )  
**IVg** = Grounded ice sheet volume ( $\text{m}^3$ )  
**IVf** = Floating ice shelf volume ( $\text{m}^3$ )  
**mbcomp** = Components of mass balance integrated over the whole ice sheet

- 1. surface mass balance
- 2. ice sheet imbalance  $\partial H / \partial t$

3. surface accumulation
4. surface melt
5. surface runoff
6. rain
7. basal melt of grounded ice sheet
8. sub-shelf melt
9. calving flux
10. ice shelf frontal melt
11. ice dynamical component (difference between input and output)
12. surface mass balance of grounded ice sheet
13. ice sheet imbalance  $\partial H / \partial t$  for grounded ice sheet
14. surface accumulation over grounded ice sheet
15. surface melt over grounded ice sheet
16. surface runoff over grounded ice sheet
17. rain over grounded ice sheet
18. basal melt of grounded ice sheet
19. grounding line flux
20. Rate of change in VAF
21. dynamical VAF component

**mb\_basin** = Components of mass balance (similar to **mbcomp**), but for each drainage basin.

**SLC** = Sea-level contribution (different from VAF)

**VAF** = Contribution to sea level rise (m), based on the volume above floatation (positive = ice loss)

## 5.4 Global parameters: file **KoriInputParams.m**

All major parameters and constants that are generally considered to be invariant for a series of model experiments are stored in the file **KoriInputParams.m**. The general control parameters for simple ice sheet model calculations are listed below. More specific parameters are detailed in the forthcoming sections.

**par.dcolor** = 'broc': Crameri color scale for plots of changes in ice thickness or surface elevation; See Figure 5 for all options. A minus sign can be used for a reversed scale.

**par.color** = 'imola': Crameri color scale for plots of velocity; See Figure 5 for all options. A minus sign can be used for a reversed scale.

**par.omega** = 0–2.5: Implicit factor in the Crank-Nicholson scheme for the ice-sheet equation solver: 0=explicit; 1=implicit; 2.5=over-implicit.



Figure 5: Cramer v8.0 color scale used in Kori–ULB.

**par.secperyear** = 31556926: number of seconds per year.

**par.varlist** = A list of variables that will be saved in the sequential output file when **ctr.timeslice** = 1. Applies only to 2-D matrices. The number of output files is controlled with **ctr.snapshot**.

**par.g** = 9.81 m s<sup>-2</sup>: gravitational acceleration.

**par.rho** = 917 kg m<sup>-3</sup>: ice density.

**par.n** = 3: Glen's flow law exponent.

**par.Hiter** = 20: Maximum number of iterations on the iterative ice thickness solver.

**par.Htol** = 1e-6: Tolerance on the iterative ice thickness solver.

**par.Z** =  $2(\rho g)^n$ : SIA isothermal pre-term.

## 6 Ice velocities

### 6.1 Approximations

The ice sheet model has several modes of operation, depending on the boundary conditions that are applied. The most elementary flow regime of the grounded ice sheet is according to the Shallow-Ice approximation (SIA; Hutter, 1983), extended with a Weertman-type (or regularized Coulomb friction) law for basal sliding. A more appropriate mode of operation for most applications is the hybrid mode, in which the flow regime of the grounded ice sheet is governed by a combination of SIA, responsible for ice-deformational flow, and the Shallow-Shelf approximation (SSA; Morland, 1987; MacAyeal, 1989) for basal sliding, which exerts a given friction at the ice sheet base (Bueler and Brown, 2009; Martin et al., 2011; Winkelmann et al., 2011). Ice shelf flow is governed by the SSA, defined by zero basal drag and extended by a water-pressure condition at the seaward edge.

### 6.2 Shallow-Ice Approximation (SIA)

The Shallow-Ice approximation (SIA; Hutter, 1983) is commonly used in ice sheet modelling. This approximation is valid for ice sheets of small aspect ratios  $h \ll L$ , where  $L$  is the horizontal length scale of the ice sheet domain, and further characterized by a low curvature and low sliding velocities. The approximation is, however, not valid near grounding lines nor for ice shelf flow, for which other approximations are applied (see below). According to SIA, the vertical mean horizontal velocity in an ice sheet is given by

$$\mathbf{v}_{\text{SIA}} = \mathbf{v}_b + \frac{2A}{n+2} h |\tau_d|^{n-1} \tau_d, \quad (23)$$

where  $\tau_d = -\rho_i g h \nabla h_s$  is the driving stress,  $\mathbf{v}_b = (u_b, v_b)$  is the basal sliding velocity and  $\mathbf{v}_{\text{SIA}} = (u, v)$  is the vertical mean horizontal velocity according to SIA.

### 6.3 Hybrid Shallow-Shelf/Shallow-Ice approximation (HySSA)

The flow velocity in an ice shelf or an ice stream characterized by low drag is derived from the Stokes equations (Stokes, 1845) by neglecting vertical shear terms and by integrating the force balance over the vertical (Morland, 1987; MacAyeal, 1989). The hybrid (HySSA) model considers that inland ice flow is governed by both deformational velocity (represented by Eq. (23)) and membrane stresses incorporated in basal sliding  $\mathbf{v}_b = \mathbf{v}_{\text{SSA}}$ . Bueler and Brown (2009) use a weighing function to ensure a continuous solution of the velocity from the interior of the ice sheet across the grounding line to the ice shelf. However, Winkelmann et al. (2011) have demonstrated that a simple addition (for the grounded ice sheet velocities) still guarantees a smooth transition for ice-stream flow, i.e.,  $\mathbf{v} = \mathbf{v}_{\text{SIA}} + \mathbf{v}_{\text{SSA}}$ . Here, we incorporate both into one equation, which leads to the following set of equations for both horizontal components of the ice velocity  $\mathbf{v} = (u, v)$ ,

$$2 \frac{\partial}{\partial x} \left( 2\eta h \frac{\partial u}{\partial x} + \eta h \frac{\partial v}{\partial y} \right) + \frac{\partial}{\partial y} \left( \eta h \frac{\partial u}{\partial y} + \eta h \frac{\partial v}{\partial x} \right) - \beta^2 u = -\tau_{d_x} - \beta^2 u_{\text{SIA}}, \quad (24)$$

$$2 \frac{\partial}{\partial y} \left( 2\eta h \frac{\partial v}{\partial y} + \eta h \frac{\partial u}{\partial x} \right) + \frac{\partial}{\partial x} \left( \eta h \frac{\partial v}{\partial x} + \eta h \frac{\partial u}{\partial y} \right) - \beta^2 v = -\tau_{d_y} - \beta^2 v_{\text{SIA}}, \quad (25)$$

where

$$\eta = \frac{A^{-1/n}}{2} \left[ \left( \frac{\partial u}{\partial x} \right)^2 + \left( \frac{\partial v}{\partial y} \right)^2 + \frac{\partial u}{\partial x} \frac{\partial v}{\partial y} + \frac{1}{4} \left( \frac{\partial u}{\partial y} + \frac{\partial v}{\partial x} \right)^2 + \dot{\varepsilon}_0^2 \right]^{(1-n)/2n}, \quad (26)$$

and where  $\tau_{d_x} = \rho_i g h (\partial h_s / \partial x)$  (similar for  $\tau_{d_y}$ ), and by definition  $\tau_{b_x} = \beta^2 u$  (similar for  $\tau_{b_y}$ ).  $\dot{\varepsilon}_0 = 10^{-20} \text{ a}^{-1}$  is a small factor to keep  $\eta$  finite, hence to prevent singularities when velocity gradients are zero. For the ice shelf,  $\beta^2 = 0$ . The SSA stress-equilibrium equations (24) and (25) require boundary conditions to be specified along the contour which defines the boundary to the ice-shelf domain, which is taken as the edge of the computational domain, irrespective of whether or not calving is considered. Dynamic conditions (specification of stress) are applied at this seaward edge, so that the vertically-integrated pressure balance then reads

$$2\eta h \left[ \left( 2 \frac{\partial u}{\partial x} + \frac{\partial v}{\partial y} \right) n_x + \frac{1}{2} \left( \frac{\partial u}{\partial y} + \frac{\partial v}{\partial x} \right) n_y \right] = n_x \frac{1}{2} \rho_i g h^2 \left( 1 - \frac{\rho_i}{\rho_s} \right), \quad (27)$$

$$2\eta h \left[ \left( 2 \frac{\partial v}{\partial y} + \frac{\partial u}{\partial x} \right) n_y + \frac{1}{2} \left( \frac{\partial u}{\partial y} + \frac{\partial v}{\partial x} \right) n_x \right] = n_y \frac{1}{2} \rho_i g h^2 \left( 1 - \frac{\rho_i}{\rho_s} \right), \quad (28)$$

where  $n_x, n_y$  are the outward-pointing normal vectors in the  $x$  and  $y$  direction, respectively. These boundary conditions are applied at the edges of the domain, or to specific domain boundaries only when `ctr.mismip > 0`.

## 6.4 Depth-Integrated Velocity Approximation (DIVA)

Following Goldberg (2011), the horizontal velocity gradients in the effective strain rate are replaced by their vertical averages:

$$\dot{\varepsilon}_{\text{DIVA}}^2 = \left( \frac{\partial \bar{u}}{\partial x} \right)^2 + \left( \frac{\partial \bar{v}}{\partial y} \right)^2 + \frac{1}{4} \left( \frac{\partial \bar{u}}{\partial y} + \frac{\partial \bar{v}}{\partial x} \right)^2 + \frac{1}{4} \left( \frac{\partial \bar{u}}{\partial z} \right)^2 + \frac{1}{4} \left( \frac{\partial \bar{v}}{\partial z} \right)^2 \quad (29)$$

where

$$\bar{u} = \frac{1}{h} \int_b^s u(z) dz, \quad \bar{v} = \frac{1}{h} \int_b^s v(z) dz. \quad (30)$$

The equations of motion can then be written as (Lipscomb et al., 2019)

$$2 \frac{\partial}{\partial x} \left( 2 \bar{\eta} h \frac{\partial \bar{u}}{\partial x} + \bar{\eta} h \frac{\partial \bar{v}}{\partial y} \right) + \frac{\partial}{\partial y} \left( \bar{\eta} h \frac{\partial \bar{u}}{\partial y} + \bar{\eta} h \frac{\partial \bar{v}}{\partial x} \right) - \beta_{\text{eff}}^2 \bar{u} = -\tau_{d_x}, \quad (31)$$

$$2 \frac{\partial}{\partial y} \left( 2 \bar{\eta} h \frac{\partial \bar{v}}{\partial y} + \bar{\eta} h \frac{\partial \bar{u}}{\partial x} \right) + \frac{\partial}{\partial x} \left( \bar{\eta} h \frac{\partial \bar{v}}{\partial x} + \bar{\eta} h \frac{\partial \bar{u}}{\partial y} \right) - \beta_{\text{eff}}^2 \bar{v} = -\tau_{d_y}, \quad (32)$$

where

$$\beta_{\text{eff}} = \frac{\beta}{1 + \beta F_2}. \quad (33)$$

Following Arthern et al. (2015), the integral  $F_n$  can be defined as

$$F_n \equiv \int_b^s \frac{1}{\eta} \left( \frac{s-z}{h} \right)^n dz. \quad (34)$$

The horizontal terms in  $\dot{\varepsilon}_{\text{DIVA}}^2$  are found using the mean velocities from the previous iteration. The vertical shear terms are then computed as follows:

$$\frac{\partial u}{\partial z} = \frac{\tau_{bx}(s-z)}{\eta(z)h}, \quad \frac{\partial v}{\partial z} = \frac{\tau_{by}(s-z)}{\eta(z)h}, \quad (35)$$

where both  $\eta(z)$  and  $\tau_b$  are from the previous iteration. The same boundary conditions apply as to the HySSA model.

## 6.5 Shallow-Shelf Approximation (SSA)

The SSA solution is similar to the hybrid model, but with omission of the deformational velocity according to the SIA in the stress balance. This simplifies Eqs. (31) and (32) to:

$$2 \frac{\partial}{\partial x} \left( 2\eta h \frac{\partial u}{\partial x} + \eta h \frac{\partial v}{\partial y} \right) + \frac{\partial}{\partial y} \left( \eta h \frac{\partial u}{\partial y} + \eta h \frac{\partial v}{\partial x} \right) - \beta^2 u = -\tau_{d_x}, \quad (36)$$

$$2 \frac{\partial}{\partial y} \left( 2\eta h \frac{\partial v}{\partial y} + \eta h \frac{\partial u}{\partial x} \right) + \frac{\partial}{\partial x} \left( \eta h \frac{\partial v}{\partial x} + \eta h \frac{\partial u}{\partial y} \right) - \beta^2 v = -\tau_{d_y}, \quad (37)$$

The same boundary conditions apply as to the HySSA model.

## 6.6 Control parameters for ice velocity

**ctr.SSA :**

- 0** : SIA solution for grounded ice sheet (default);
- 1** : calculation of SSA for grounded ice sheet and ice shelf
- 2** : calculation of the hybrid HySSA model (SSA+SIA) for the grounded ice sheet.
- 3** : DIVA solver for both ice sheet and ice shelf

**ctr.shelf :**

- 0** : no ice shelves (default);
- 1** : add ice shelves (requires that **ctr.SSA > 0**).

**ctr.shelftune** : Tuning factor for the ice shelf to take into account anisotropy (Ma et al., 2010). Lower values make ice shelf more viscous. Default = 0.5. **ctr.shelftune** can also be defined as a 2d matrix to take into account spatial differences for different ice shelves. When using the DIVA solver, higher values for **ctr.shelftune** are required, as the thermomechanical coupling is based on the vertical integration of the flow factor  $A$ , instead of using its basal value.

**ctr.upstream :**

**1** : Upstream differences for ice velocities  $u, v$  in advection part of the ice-thickness equation (default). Does not apply to the SIA model.

**0** : Central differences

**ctr.BetaIter** : Number of iterations on recalculating  $\beta^2$  in the nonlinear part of the SSA velocity calculations; can be set throughout to **ctr.nsteps**. (Default: **ctr.BetaIter** = 5).

**ctr.ItSolv** : Iterative solver for both the ice thickness and the SSA/HySSA velocities (default=1).

**0** : Direct solver in MatLab

**1** : Iterative solver (BICGSTAB for SSA and PCG for ice thickness solver)

**2** : Force iterative solver and prevent direct solver to take over when tolrence is exceeded (only for BICGSTAB in SSA solver).

**ctr.shelfBC** : Force a ice-ocean shelf condition directly on the calving front instead of only on edge of model domain. Useful for synthetic experiments, but not very efficient for real ice sheets (default=0).

**ctr.OceanVisc** : default=1e8

**ctr.NumCheck** : When set to 1, this creates a time-dependent matrix with information on the numerical performance of the SSA velocity solver. The resulting matrix contains several columns (Default=0)

**1** : Number of iterations in the nonlinear viscosity iteration of the SSA velocity solver

**2** : Limit value on the same iteration

**3** : Relative residual in the BICGSTAB solver

**4** : Number of iterations in the iterative BICGSTAB solver

**5** : Flag indicating whether convergence of BICGSTAB has been reached

## 6.7 Global parameters for ice velocity

**par.maxspeed** = 40 000 m a<sup>-1</sup>: Maximum tolerated flow speed of ice sheet/ice shelf system.

**par.rhow** = 1028 917 kg m<sup>-3</sup>: sea-water density

**par.visciter** = 50: Maximum number of iterations on the nonlinear part of the SSA equation.

**par.visctol** = 5e-1: Tolerance for calculation of the nonlinear part of the SSA equation.

**par.veliter** = 50: Maximum number of iterations for the iterative SSA velocity solver.

**par.veltol** = 1e-4: Tolerance for the iterative SSA velocity solver.

## 7 Ice temperature and rheology

### 7.1 Ice temperature

The diffusion–advection equation for an ice sheet (and ice shelf) is given by (Huybrechts, 1992):

$$\frac{\partial T}{\partial t} = \kappa \frac{\partial^2 T}{\partial z^2} - u \frac{\partial T}{\partial x} - v \frac{\partial T}{\partial y} - w \frac{\partial T}{\partial z} + \frac{\Phi_d}{\rho_i c_p}, \quad (38)$$

where  $\kappa = K/\rho_i c_p$  is the thermal diffusivity of ice,  $K$  is the thermal conductivity,  $c_p$  is the heat capacity of ice,  $T$  is the ice temperature, and

$$\Phi_d = -\rho_i g (h_s - z) \nabla h_s \frac{\partial \mathbf{v}_d}{\partial z} \quad (39)$$

represents deformational heating, where  $\mathbf{v}_d$  is the deformational velocity component ( $\mathbf{v}_d = \mathbf{v} - \mathbf{v}_b$ ). Note that we consider both  $K$  and  $c_p$  as constants, hence independent of temperature. The basal boundary condition is given by

$$\frac{\partial T_b}{\partial z} = \frac{G + \tau_d \mathbf{v}_b}{K}, \quad (40)$$

where  $G$  is the geothermal heat flux and the second term represents frictional heating at the base. The last term in Eq. (40) represents strain heating. Phase changes at the base are incorporated in the model by keeping the basal temperature at the pressure melting point whenever it is reached or basal melt water is present. The basal melt rate  $\dot{b}$  (positive when melting) is calculated from the difference between the basal temperature gradient in Eq. (40) and the gradient corrected for pressure melting,

$$\dot{b} = \frac{K}{\rho L} \left[ \left( \frac{\partial T_b}{\partial z} \right)_c - \frac{G + \tau_d \mathbf{v}_b}{K} \right] \quad (41)$$

where the subscript  $c$  denotes the gradient corrected for pressure melting, and  $L$  is the specific latent heat for fusion. Given the two-dimensional nature of the model, the temperature field employs shape functions for vertical profiles of deformational velocity  $\vec{v}_d$ , its vertical gradient, and the vertical velocity, based on SIA (Hindmarsh, 1999). Eq. 38 is then solved in scaled vertical coordinates  $\zeta = (h_s - z)/h$ , with  $\zeta = 0$  at the surface and  $\zeta = 1$  at the bottom of the ice sheet.

Since the solutions of SIA, SSA and the hybrid model are two-dimensional, we use shape functions for the three-dimensional horizontal and vertical velocity field in the thermodynamic model. We follow the approach by Lliboutry (1979) and Ritz (1992) that take into account a higher power of the horizontal velocity profile due to softer ice at the bed, hence higher shear strain rates, i.e.,

$$\mathbf{v} = \frac{\dot{\gamma}_b h}{p_r + 2} \quad (42)$$

where

$$\dot{\gamma}_b = B_0 \tau_d^n \exp \left[ \frac{Q}{R} \left( \frac{1}{T_{mb}} - \frac{1}{T_b} \right) \right] \quad (43)$$

and

$$p_r = n - 1 + \frac{QGh}{RT_b^2} \quad (44)$$

so that,

$$\mathbf{v}(\zeta) = \mathbf{v}_b + \frac{p_r + 2}{p_r + 1} (1 - \zeta^{p_r+1}) \mathbf{v} \quad (45)$$

and following Pattyn (2010),

$$w(\zeta) = -\dot{a} \left( 1 - \frac{p_r + 2}{p_r + 1} (1 - \zeta) + \frac{1}{p_r + 1} (1 - \zeta)^{p_r+2} \right) - \dot{b} + \mathbf{v} \nabla b + (1 - \zeta) \mathbf{v} \nabla h \quad (46)$$

For an isothermal ice sheet,  $p_r = n$ . For the DIVA model, the three-dimensional velocity field is obtained from the vertical integration of the effective viscosity, by making use of Eq. (34) Lipscomb et al. (2019), i.e.,

$$u(s) = u_b(1 + \beta^2 F_1) \quad (47)$$

## 7.2 Thermomechanical coupling

For the SIA, SSA and hybrid models that determine the velocity field based on the shape factors  $p_r$ , the flow parameter  $A$  and its temperature dependence on temperature are specified as in Ritz (1987, 1992):

$$\begin{aligned} A &= \frac{1}{2} E_f 1.66 \times 10^{-16} \exp \left[ \frac{78.20 \times 10^3}{R} \left( \frac{1}{T_m} - \frac{1}{T^*} \right) \right] \\ &\quad \text{if } T^* \geq 266.65 \text{K} \\ A &= \frac{1}{2} E_f 2 \times 10^{-16} \exp \left[ \frac{95.45 \times 10^3}{R} \left( \frac{1}{T_m} - \frac{1}{T^*} \right) \right] \\ &\quad \text{if } T^* < 266.65 \text{K}, \end{aligned} \quad (48)$$

where  $T^* = T - T_m$  is the homologous basal temperature, with  $T_m = -8.66 \times 10^{-4}(1 - \zeta)h$  the pressure melting correction and  $R$  the gas constant. Units of  $A$  are  $\text{Pa}^{-3} \text{yr}^{-1}$  corresponding to  $n = 3$ . The enhancement factor  $E_f$  is set to 1 for the main ice sheet model, and to  $E_f = 0.5$  for ice shelves. The ratio of enhancement factors represent differences in fabric anisotropy between grounded and ice shelf ice (Ma et al., 2010).

For the DIVA model, the thermomechanical coupling is obtained through vertical integration of the effective viscosity and the temperature-dependent flow factor  $A$ . For each vertical layer, the flow factor is determined as (Huybrechts, 1992; Greve and Blatter, 2009):

$$A = E_f a \exp \left( -\frac{Q}{RT^*} \right), \quad (49)$$

where  $a = 3.985 \times 10^{-13} \text{ Pa}^{-3} \text{s}^{-1}$  and  $Q = 60 \times 10^3 \text{ kJ mol}^{-1}$  for  $T^* < 263.15 \text{ K}$ , and  $a = 1.916 \times 10^3 \text{ Pa}^{-3} \text{s}^{-1}$  and  $Q = 139 \times 10^3 \text{ kJ mol}^{-1}$  for  $T^* \geq 263.15 \text{ K}$ . Note that for ice shelves, the factor  $E_f$  may have to be adjusted to a slightly higher value, as the thermomechanical coupling function is different.

### 7.3 Enthalpy

The so-called cold-ice method to calculate the temperature field (as given above) fails to conserve energy in temperate ice, as variations in latent heat and water content are not accounted for. Alternatively, enthalpy formulations (e.g., Aschwanden et al., 2012; Kleiner et al., 2015; Hewitt and Schoof, 2017) have been developed to ensure energy conservation in the presence of polythermal conditions. The three-dimensional enthalpy field  $E$  ( $\text{J kg}^{-1}$ ) can be computed from:

$$\frac{\partial E}{\partial t} = \frac{\partial}{\partial z} \left( k_{c,t} \frac{\partial E}{\partial z} \right) - w \frac{\partial E}{\partial z} - u \frac{\partial E}{\partial x} - v \frac{\partial E}{\partial y} + \frac{\Phi_d}{\rho_i} - \frac{\rho_w}{\rho_i} LD(\omega), \quad (50)$$

were  $k_{c,t} = K_c = K/(c\rho_i)$  and  $k_{c,t} = K_0 = K_c \times 10^{-5}$  is the diffusivity in cold ( $E < E_{pmp}$ ) and temperate ice ( $E \geq E_{pmp}$ ), respectively,  $E_{pmp} = c(T_{pmp} - T_{ref})$  is the enthalpy of ice at the pressure melting point without water content, and  $T_{ref} = 223.15$  K is a reference temperature. The term  $-(\rho_w/\rho_i)LD(\omega)$ , where  $D(\omega)$  is a drainage function (Aschwanden et al., 2012), is added to prevent unrealistic high water content (Aschwanden et al., 2012; Greve and Blatter, 2016; Hewitt and Schoof, 2017). We explicitly enforce the continuity condition on the cold-temperate transition surface (CTS), considering the melting conditions on the CTS only, following the ENTM scheme of Blatter and Greve (2015) and Greve and Blatter (2016). This is achieved through a two-step procedure. First, the enthalpy field is calculated for the entire vertical ice column, and the CTS is defined as the highest grid point of the temperate layers. Then, a corrector step is applied for the cold part of each ice column that possesses a CTS by applying the continuity condition as a boundary condition at the CTS. The final enthalpy profiles combine the corrected profiles for the cold part and the initial estimates for the temperate part. The temperature  $T$  and the water content  $\omega$  are then diagnostically determined from the modelled enthalpy field:

$$T = \begin{cases} E/c + T_{ref}, & E < E_{pmp}, \\ T_{pmp}, & E \geq E_{pmp}. \end{cases} \quad (51)$$

$$\omega = \begin{cases} 0, & E < E_{pmp}, \\ (E - E_{pmp})/L, & E \geq E_{pmp}. \end{cases} \quad (52)$$

The surface boundary condition is given by  $E_s = c(T_s - T_{ref})$ . The basal boundary conditions are determined from Aschwanden et al. (2012):

$$\begin{cases} K_c \partial E_b / \partial z = G + F_b, & E_b < E_{pmp} \text{ and } H_w = 0, \\ E_b = E_{pmp}, & E_b < E_{pmp} \text{ and } H_w > 0, \\ E_b = E_{pmp}, & E_b \geq E_{pmp} \text{ and } H_w > 0 \text{ and } H_t = 0, \\ K_0 \partial E_b / \partial z = 0, & E_b \geq E_{pmp} \text{ and } H_w > 0 \text{ and } H_t > 0, \end{cases} \quad (53)$$

where  $0 \leq H_w \leq 2$  is the thickness of the water layer and  $H_t$  is the thickness of the temperate layer. The water layer thickness is determined by:

$$\frac{\partial H_w}{\partial t} = \dot{b} - C_d, \quad (54)$$

where  $C_d = 0.001 \text{ m a}^{-1}$  is a constant drainage rate. The basal melt rate is computed from:

$$\dot{b} = \frac{G + F_b - q_i}{(1 - \omega)\rho_i L}, \quad (55)$$

where  $q_i = K_c \partial E_b / \partial z$  is the heat flux in the ice (Aschwanden et al., 2012; Kleiner et al., 2015). Equation (55) allows for refreezing as long as  $H_w > 0$ . Furthermore, the basal melt increases with the drainage of excess englacial meltwater production (Aschwanden et al., 2012).

## 7.4 Control parameters for thermodynamics

**ctr.Tcalc :**

- 0** : No temperature calculation (default)
- 1** : Calculate temperature field in ice sheet (and ice shelf), isothermal ice sheet ( $A = A_0$ )
- 2** : Calculate temperature field and thermomechanical coupling, , i.e.  $A = f(T)$

**ctr.Enthalpy :**

- 0** : No enthalpy calculation (default);
- 1** : Temperature based on enthalpy calculation (ctr.Tcalc defines whether thermo-mechanical coupling is engaged or not).

**ctr.drain :**

- 1** : Activates the drainage of englacial meltwater (produced within the temperate ice) when a threshold is reached (1-3%) (default);
- 0** : No drainage.

**ctr.Tinit :**

- 0** : Initial temperature field read from input file or when not available kept constant at values of surface temperature (default);
- 1** : Initialization of temperature field from semi-analytical steady-state temperature solution;
- 2** : Always use the steady-state semi-analytical solution.

**ctr.Ao** : Isothermal value of Glen's flow law parameter  $A$  ( $\text{Pa}^{-n} \text{ a}^{-1}$ ); Default =  $10^{-16}$ .

**ctr.kmax** : number of vertical layers for temperature calculation (default = 11).

## 7.5 Global parameters for thermodynamics

**par.T0** = 273.15 K: absolute temperature

**par.K** = 2.1: thermal conductivity

**par.kdif** = 1.1487e-6:  $k = K/(\rho c_p)$ , where  $c_p = 2009$

**par.cp** = 2009; Heat capacity of ice

**par.K0** =  $10^5 K/c_p$ ; Thermal conductivity of temperate ice

**par.Kc** =  $K/c_p$

**par.Tref** = 223.15 K

**par.pmp** = 8.66e-4: Clausius Clapeyron dependence of melt on pressure; taken as a function of ice thickness  $H$  (Payne et al., 2000)

**par.atune** = 1: tuning factor in Arrhenius equation (for ice sheet; scales with tuning factor for ice shelf)

**par.R** = 8.314: Gas constant

**par.udfrac** = 0.25: fraction of deformational velocity in heat dissipation for initialization of the temperature field with semi-analytical solution (when **ctr.Tinit** = 1).

**par.intT** = 10: Temperature calculation every **intT** iterations.

**par.TrTemp** = -5: Basal temperature for which ice is frozen to bed (-5°C).

**par.Q1** = 78.2e3: factor in Arrhenius equation (Ritz, 1992)

**par.Q2** = 95.45e3: factor in Arrhenius equation (Ritz, 1992)

**par.a1** = 1.66e-16: factor in Arrhenius equation (Ritz, 1992)

**par.a2** = 2e-16: factor in Arrhenius equation (Ritz, 1992)

**par.a1D** =  $3.985^{-13} \times \text{par.secperyear}$ , used for the DIVA model

**par.a2D** =  $1.916 \times \text{par.secperyear}$ , used for the DIVA model

**par.Q1D** =  $60 \times 10^3$ , used for the DIVA model

**par.Q2D** =  $139 \times 10^3$ , used for the DIVA model

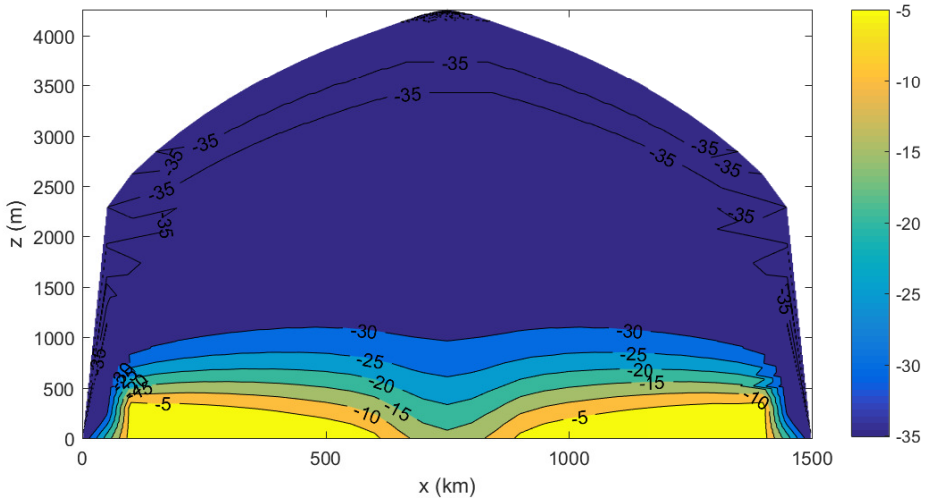


Figure 6: Englacial temperature distribution along the central flowline of the rectangular domain. Note that the wiggles are due to the poor contouring algorithm and not an artefact of the model.

## 7.6 Example: a square thermomechanically-coupled ice sheet

Using the same simple setup as before, we will consider a thermomechanically-coupled ice sheet on a square flat bedrock, forced by a constant surface mass balance. Ice deformation is according to the shallow-ice approximation (SIA). The script looks like the following:

```
% Fixed margin experiment for a thermo-coupled ice sheet

ctr.imax=31;
ctr.jmax=31;
ctr.delta=50.e3;
ctr.nsteps=1001;
ctr.dt=50.;
ctr.Tcalc=2;
ctr.kmax=21;
ctr.MbConst=0.3;
ctr.TsConst=-35;

KoriModel('','simple_out',ctr);
```

The resulting temperature field along the central axis of the domain and the horizontal velocity field along the same axis and according to (45) are displayed in Figs. 6 and 7, respectively.

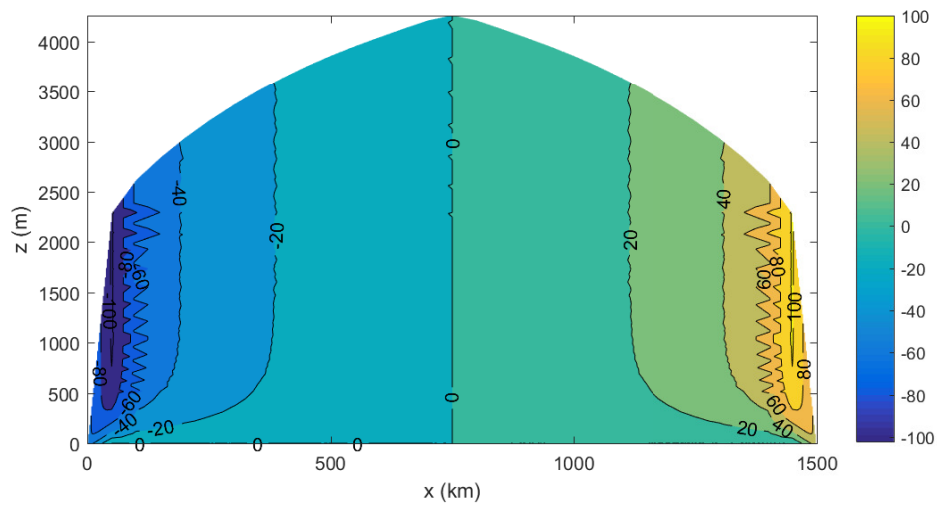


Figure 7: Horizontal velocities along the central flowline of the rectangular domain. Note that the wiggles are due to the poor contouring algorithm and not an artefact of the model.

## 8 Basal sliding and subglacial conditions

### 8.1 Regularized Coulomb friction and Weertman law

We use a generalized slip law, or regularized Coulomb friction law, that reconciles both Weertman/Budd and Coulomb slip laws (Schoof, 2005; Gagliardini et al., 2007; Joughin et al., 2019; Zoet and Iverson, 2020; Helanow et al., 2021):

$$\tau_b = CN \left( \frac{|\mathbf{v}_b|}{|\mathbf{v}_b| + u_0} \right)^{1/m} \frac{\mathbf{v}_b}{|\mathbf{v}_b|} = CN \left( \frac{|\mathbf{v}_b|}{|\mathbf{v}_b| + A'_b C^m N^m} \right)^{1/m} \frac{\mathbf{v}_b}{|\mathbf{v}_b|} \quad (56)$$

where,  $A'_b = u_0(CN)^{-m}$  is a sliding coefficient, often used when a friction law is written as a sliding law. Low speeds and high effective stresses result in viscous Weertman-style sliding; high sliding speeds and low effective stresses – conditions commonly present at the bases of ice streams – promote shallow deformation of the bed at its Coulomb strength. The main advantage of this description is that the transition from power-law slip to plastic Coulomb occurs smoothly. Please, keep in mind that by default, the value of  $u_0$  is set to a large number and the effective pressure  $N$  is considered constant, so that the friction law is essentially a Weertman law and NOT a regularized Coulomb friction law.

In the Kori–ULB model, we formulate the slip law as a function of  $f(A'_b, u_0)$ , instead of  $f(C, u_0)$  in Joughin et al. (2019) or  $f(A'_b, C)$  in Helanow et al. (2021). Since  $A'_b = u_0(CN)^{-m}$ , we can write Eq. (56) as

$$\tau_b = A'^{-1/m} \left( \frac{u_0}{|\mathbf{v}_b| + u_0} \right)^{1/m} |\mathbf{v}_b|^{1/m-1} \mathbf{v}_b \quad (57)$$

where the term between brackets varies between 0 (plastic) and 1 (viscous). This general slip law can be related to other existing laws by:

- Budd law:  $u_0 \gg |\mathbf{v}_b|$ ,
- Weertman law:  $u_0 \gg |\mathbf{v}_b|$  and  $N$  is a constant value,
- Plastic Coulomb:  $u_0 \approx 0$ , so that  $\tau_b \approx CN$ .

Through the definition of  $A'_b = u_0(CN)^{-m}$ , the general slip law can in principle be expressed as a sliding law so that it fits in with the SIA description, i.e.,

$$\mathbf{v}_b = \frac{1}{\alpha} A'_b |\tau_d|^{m-1} \tau_d \quad (58)$$

where

$$\alpha = 1 - \frac{A'_b}{u_0} |\tau_d|^m \quad (59)$$

Note that the limiting condition is that  $0 < \alpha \leq 1$ . This means that the sliding law can never be pure plastic ( $\alpha = 0$ ), but comes very close to plasticity for high sliding velocities. For  $\alpha = 1$ , the sliding law takes the form of the Budd/Weertman sliding law and corresponds to  $u_0 \rightarrow +\infty$ . The basal sliding factor  $A'_b$  implicitly incorporates  $u_0$ , is a function of the effective pressure  $N$  and is also temperature dependent. The latter allows for sliding within

a basal temperature range between -3 and 0°C. It further takes into account sub-grid sliding across mountainous terrain (Pollard et al., 2015):

$$A'_b = N^{-p} [(1 - r) A_{\text{froz}} + r A_b] , \quad (60)$$

where  $r = \max[0, \min[1, (T^* - T_r)/(-T_r)]]$ ,  $A_{\text{froz}}$  is the sliding coefficient in case of frozen bedrock (chosen to be very small but different from zero to avoid singularities in the basal friction calculation),  $T^*$  is the temperature corrected for the dependence on pressure (see Section 7.2) and  $T_r = \min[-3 - 0.02\sigma_b]$ , where  $\sigma_b$  is the standard deviation of bedrock elevation within the grid cell (Pollard et al., 2015). Basal sliding factors  $A_b$  are either considered constant in space/time or are spatially varying and obtained through optimization methods (see Sect. 12). The exponent  $p$  equals  $m$  of the sliding law when effective pressure is calculated, and takes the value  $p = 0$  otherwise.

Finally, the value for the basal sliding coefficient `ctr.Asin` is a nominal value for  $m = 2$  and automatically scaled for other values of  $m$  through a scaling factor that is multiplied with  $A_b$

$$A_{\text{scale}} = 10^{5(2-m)} \quad (61)$$

This way, the value of `ctr.Asin` can be kept more or less the same for different choices of  $m$  (see also Section 12). A typical value for `ctr.Asin` is  $A_b = 3 \times 10^{-9} \text{ m a}^{-1} \text{ Pa}^{-2}$  for the Antarctic ice sheet, corresponding to  $m = 2$  and is decreased with  $10^5$  for each increase of  $m$  by one unit.

## 8.2 Effective pressure at the ice sheet base

There are different ways to calculate the effective pressure at the base of an ice sheet. In theory, the effective pressure  $N$  represents the ice overburden pressure  $p_o$ , i.e., the downward force due to the weight of overlying ice and till, minus the subglacial water pressure ( $p_w$ ):

$$N = p_o - p_w = \rho_i g h - p_w \quad (62)$$

In the following sections, we describe in more detail on how either subglacial water pressure  $p_w$  or effective pressure  $N$  is determined.

### 8.2.1 Height above buoyancy

Subglacial water pressure is often neglected in ice sheet models and therefore its relationship with the effective pressure and the basal sliding is often neglected too. A simple way is to link  $p_w$  to the depth of the bed below sea level. Near grounding lines in direct contact with the ocean, subglacial water pressure of saturated till may be approximated by (Tsai et al., 2015):

$$p_w = -P_w \rho_s g (b - z_{sl}) , \quad (63)$$

where  $P_w$  is a fixed fraction of the overburden pressure. Eq. (63) is valid for  $b - z_{sl} < 0$ , otherwise  $p_w = 0$ . By definition,  $p_w = \rho_i g h$  at the grounding line and underneath floating ice shelves, so that the effective pressure becomes zero (or close to zero when modulated by the value of  $P_w$ ). This means that only marine terminated parts of the ice sheet are impacted

by the subglacial water. According to Lüthi et al. (2002), the pore water pressure, i.e., the pressure of the subglacial water mixed with the solid part of the till, represents a fraction slightly smaller than 100% of the ice overburden pressure. Bueler and Brown (2009) consider the pore water pressure locally as at most a fixed fraction ( $P_w = 95\%$ ) of the ice overburden pressure  $\rho_i gh$ . The fraction varies among different studies, i.e., 96% (Winkelmann et al., 2011), 97% (Van Pelt and Oerlemans, 2012), and 99% (Gandy et al., 2019). This is probably the most common representation of subglacial water pressure in large-scale Antarctic ice sheet models.

### 8.2.2 Subglacial water film

Subglacial water flow can be introduced following the method of Le Brocq et al. (2009) based on a single element type to describe the morphology of the drainage system, i.e., a Weertman-type water film (Flowers, 2015). The model assumes that water flows in a thin film of water of the order of  $10^{-3}$  m thickness. The evolution of the water film depth  $d_w$  is given by

$$\frac{\partial d_w}{\partial t} = M - \nabla \cdot (\mathbf{u}_w d_w) \quad (64)$$

where  $M$  is the basal melt rate (positive for melting) underneath the grounded ice sheet, and  $\mathbf{u}_w$  is the depth-averaged water film velocity, calculated using a theoretical treatment of laminar flow between two parallel plates, driven by differences in the water pressure (Weertman, 1966):

$$\mathbf{u}_w = \frac{d_w^2}{12\mu} \nabla \Phi \quad (65)$$

where  $\mu$  is the viscosity of water and  $\Phi$  is the hydraulic potential. The hydraulic potential represents the total mechanical energy per unit volume of water required to move the water from one state to another (Flowers, 2015), and is a function of the elevation potential and the water pressure, i.e.,

$$\Phi = \rho_w g b + p_w = \rho_w g b + \rho_i g h - N \quad (66)$$

The water pressure,  $p_w$ , is a function of the ice overburden pressure and the effective pressure  $N$ . In a distributed system, however, the water pressure will be close to, if not at, the overburden pressure. As a result, a simplification can be made to Eq. (66), assuming  $N$  to be zero (see, e.g., Budd and Jenssen, 1987; Alley, 1996). The assumption that  $N$  is zero simplifies the calculation of the hydraulic potential surface by removing the need to calculate the water pressure. With this simplification, the gradient of the potential surface is written as

$$\nabla \Phi = \rho_i g \nabla h_s + (\rho_w - \rho_i) g \nabla b \quad (67)$$

Taking  $\partial d_w / \partial t = 0$  in Eq. (64) (steady-state approach), it is possible to use a flux balance approach to calculate the steady-state water depth (in a similar way to balance velocity calculations; see, e.g., Budd and Warner (1996) or Le Brocq and others (2006), for more details). The balance approach requires the outgoing flux in any given grid cell to be equal to the incoming water flux plus the local melt rate within the cell. The routing direction of

the subglacial water is given by the hydraulic potential gradient  $\nabla\Phi$ . The water depth is then obtained from the outgoing water flux  $Q_l$ , i.e.,

$$d_w = \left( \frac{12\mu Q_l}{|\nabla\Phi|} \right)^{\frac{1}{3}} \quad (68)$$

Subglacial water thickness is then related to subglacial water pressure through

$$p_w = P_w \rho g h \left( \frac{d_w}{d_w^0} \right), \quad (69)$$

where  $d_w^0 = 0.0015$  m is a limit value to the subglacial water thickness.

### 8.2.3 Sliding related to water flux

Alternatively, Goeller et al. (2013) propose to introduce a simple physically plausible correlation of the sliding rate factor and the subglacial water flux:

$$A_b = A_o \exp \left( \frac{\Phi}{\Phi_0} \right), \quad (70)$$

where  $\Phi_0$  is a limit factor on the subglacial water flux, taken as  $10^5$  (Goeller et al., 2013), and  $A_o$  the initial value of  $A_b$ . A similar approach has been followed by Pattyn et al. (2005). The approach is rather intuitive than physical and just considers that basal sliding increases when the water flux beneath the ice sheet increases.

### 8.2.4 Effective pressure in till

Bueler and Brown (2009) employ an effective thickness of stored liquid water at the base of the ice column. This layer of thickness  $W$  is used to estimate the subglacial water pressure reduced to the pore water pressure according to

$$p_w = P_w \rho_i g h \frac{W}{W_{\max}}, \quad (71)$$

where  $W_{\max}$  is the maximum saturated till thickness, fixed at 2 m, which has an impact on the till weakening by pressurized water. A fixed fraction of ice overburden equal to one will imply that the yield stress becomes zero in the case of full till saturation (Van Pelt and Oerlemans, 2012). An alternative way, which has been used here, to derive the effective pressure in the case of a deformable bed composed by a permeable till is to express the effective pressure,  $N$ , in Eq. (62) as a function of the sediment void ratio,  $e$ , due to the changing water content in the till (van der Wel et al., 2013; Bougamont et al., 2014), i.e.,

$$N = N_0 \times 10^{-(e-e_0)/C_c}, \quad (72)$$

where  $e_0$  is the void ratio at a reference effective pressure  $N_0$  and  $C_c$  is the till compressibility. Bueler and van Pelt (2015) propose to employ Eq. (72) in a hydrological model of subglacial water drainage within an active layer of the till,  $W$ . As the water in till pore spaces is much less mobile than that in the linked-cavity system because of the very low hydraulic conductivity of till, an evolution equation for  $W_{\text{til}}$  without horizontal transport can be written (Bueler and van Pelt, 2015)

$$\frac{\partial W}{\partial t} = M - C_t \quad (73)$$

Here  $C_t$  is a fixed rate that makes the till gradually drain in the absence of water input; we choose  $C_t$  to be  $1 \text{ mm a}^{-1}$ , which is small compared to typical values of subglacial melt. We constrain the layer thickness by

$$0 \leq W \leq W_{\max} \quad (74)$$

The effective pressure  $N$  is then written as the following function of  $W$  (Bueler and van Pelt, 2015),

$$N = N_0 \left( \frac{\delta P_o}{N_0} \right)^s 10^{\left( \frac{e_0}{C_c} \right)(1-s)} \quad (75)$$

where  $s = W/W_{\max}$  and bounded by  $N = \min \{p_o, N\}$  and  $\delta p_o$  is the lower bound on  $N$ , taken as a fraction of the ice overburden pressure.

### 8.3 Efficient and inefficient basal hydrology on hard and soft beds

A fast and simplified hydrological model has recently been developed by Kazmierczak et al. (2024) and proposes a simplified model of the complex subglacial system that allows us to dynamically link subglacial hydrology to basal sliding for various bed types (hard and soft). The model considers different spatially- and temporally-varying subglacial water drainage systems. Their morphologies depend both on the subglacial water flux (distributed or channelized) and the rheology of the bed. The key simplifying assumptions are (see Figure 8):

1. There is limited temporal melt variability so that the hydrological system is in a quasi-static equilibrium with respect to the ice-sheet geometry. Therefore, changes in ice geometry will be the main driver for changes in subglacial water variability (both spatial and temporal).
2. A few kilometers upstream of the grounding line, the hydraulic gradient is approximated by the geometrical gradient.
3. The drainage density, that is, the number of conduits per grid cell, is uniform.
4. The effective pressure distribution is not calculated at the sub-grid (local) level.

While the water mass balance is defined at the global scale, conduits must evolve at the local scale, which requires water flow to be resolved at this scale, irrespective of whether it is associated with a distributed or a localized flow pattern, similarly to what is done in Gowan et al. (2023). Let us denote by  $S$  the cross-section area in a conduit, with characteristic width and thickness  $L$  and  $H$  (Figure 9), so that  $S = H L$ . The equations governing the geometry of the conduits and the flow of water within them in a quasi-static regime are given by the following:

$$\left\{ \begin{array}{l} Q_w = K S^\alpha \|\nabla \phi\|^{\beta-1}, \text{ in } \Omega, \\ \|\vec{v}_b\| h_b + \frac{Q_w \|\nabla \phi\|}{\rho_i \mathcal{L}_w} = 2 n^{-n} A L^2 |N|^{n-1} N, \text{ in } \Omega, \\ N = 0, \text{ on } \Gamma_{\text{gl}}, \end{array} \right. \quad (76a)$$

$$\left\{ \begin{array}{l} Q_w = K S^\alpha \|\nabla \phi\|^{\beta-1}, \text{ in } \Omega, \\ \|\vec{v}_b\| h_b + \frac{Q_w \|\nabla \phi\|}{\rho_i \mathcal{L}_w} = 2 n^{-n} A L^2 |N|^{n-1} N, \text{ in } \Omega, \\ N = 0, \text{ on } \Gamma_{\text{gl}}, \end{array} \right. \quad (76b)$$

$$\left\{ \begin{array}{l} Q_w = K S^\alpha \|\nabla \phi\|^{\beta-1}, \text{ in } \Omega, \\ \|\vec{v}_b\| h_b + \frac{Q_w \|\nabla \phi\|}{\rho_i \mathcal{L}_w} = 2 n^{-n} A L^2 |N|^{n-1} N, \text{ in } \Omega, \\ N = 0, \text{ on } \Gamma_{\text{gl}}, \end{array} \right. \quad (76c)$$

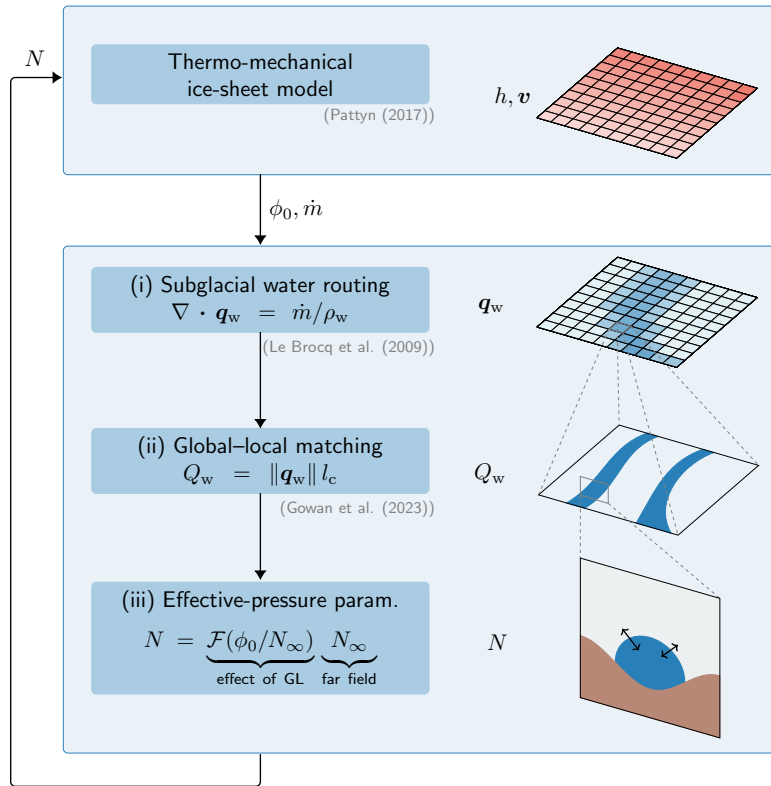


Figure 8: Flowchart of the dynamical linkage between the ice sheet and the subglacial hydrology. At each time step, the ice-sheet model provides the basal melt rate  $\dot{m}$  and the geometrical potential  $\phi_0$ . Based on these, the effective pressure is computed in three steps: (i) The globally distributed subglacial water flux  $\vec{q}_w$  is computed according to Le Brocq et al. (2009); (ii) a connection between both global and local (conduit) scale is obtained by specifying the distance  $l_c$  between the conduits (Gowan et al., 2023), yielding a volumetric water flux  $Q_w$  in each conduit; (iii) the effective pressure  $N$  is computed for each conduit via a parametrization where  $\mathcal{F}(\phi_0/N_\infty) = \text{erf}[(\sqrt{\pi}/2)\phi_0/N_\infty]$  serves as a correction factor for the impact of the grounding line (GL), and where  $N_\infty$  is the effective pressure far upstream of the grounding line. This effective pressure is then used by the large-scale ice-sheet model and is the same for all conduits that belong to the same grid cell (Kazmierczak et al., 2024).

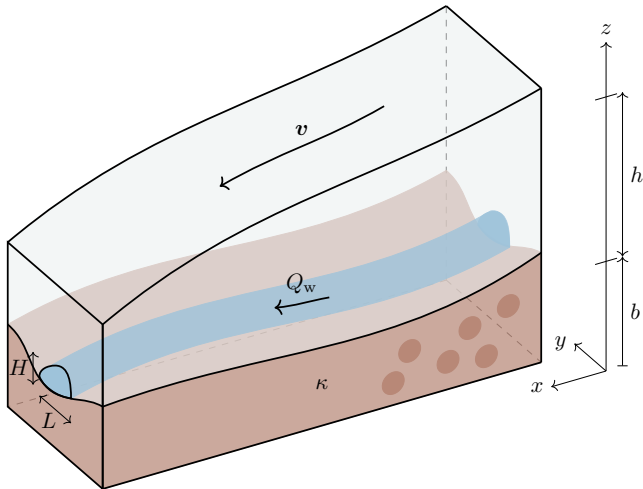


Figure 9: Schematic representation of a conduit (here, of a channel) in the subglacial hydrological system, characterized by a cross-sectional width  $L$  and thickness  $H$  and by a water flux  $Q_w$ . The ice sheet has a thickness  $h$ , is moving at a velocity  $\vec{v}$ , and overlays the bedrock whose upper surface is located at  $z = b$ . The bedrock type is parameterized by  $\kappa$ , with  $\kappa = 1$  corresponding to a soft bed,  $\kappa = 0$  corresponding to a hard bed, and  $0 < \kappa < 1$  corresponding to a mixed bed (Kazmierczak et al., 2024).

where  $h_b$  is the characteristic height of bed obstacles, and  $A$  and  $n$  are the viscosity parameters in Glen’s flow law (Glen, 1955; Paterson, 1994), respectively. The first equation is a Darcy–Weisbach constitutive equation for the water flow with  $K$  a conductivity coefficient, and  $\alpha$  and  $\beta$  exponents. Following Schoof (2010), we assume a turbulent flow, with  $\alpha = 5/4$ ,  $\beta = 3/2$ , and  $K = (2/\pi)^{1/4} \sqrt{(\pi + 2)/(\rho_w f)}$ , where  $f$  is a friction coefficient (e.g., Clarke, 1996). The choice of a turbulent flow is justified for large water fluxes, which is the case for converging subglacial channels near the grounding line. The second equation describes the equilibrium between opening and closure rates of the conduits, assuming that the hydrological system is at equilibrium. In general, opening and closing of subglacial water systems are due to various mechanisms depending on the drainage system and bed type involved. These mechanisms include, amongst others, melt of the subglacial conduit walls, sliding over bed protrusions, erosion of sediments, regelation, creep of ice, and creep of sediments (Bueler and van Pelt, 2015). Here, we consider opening rates associated with sliding over bed obstacles, melting of the conduit walls, and a closure rate due to ice creep. Finally, the third equation comes from the equality between the subglacial water pressure and the sea-water pressure at the grounding line (Drews et al., 2017), which holds because we are considering marine-terminated ice sheets.

To compute the effective pressure within each conduit, we combine the Darcy–Weisbach equation (76a) with the opening-closing equation (76b). This allows us to eliminate  $S$  and obtain an equation for  $N$  only. However, the resulting equation takes the form of a non-linear differential equation, which is not easy to solve. The complexity stems from the fact that  $\nabla\phi$  depends on  $N$  through  $\nabla\phi = \nabla\phi_0 - \nabla N$ . However, given our second simplifying assumption, we have  $\nabla\phi \approx \nabla\phi_0$  outside the vicinity of the grounding line. We then obtain algebraic equations for the effective pressure and the cross-sectional area far from the grounding line,

$N_\infty$  and  $S_\infty$ :

$$N_\infty = \left[ \left( \frac{H(S_\infty)}{S_\infty} \right)^2 \frac{\rho_i \mathcal{L}_w \|\vec{v}_b\| h_b + Q_w \|\nabla \phi_0\|}{2n^{-n} \rho_i \mathcal{L}_w A S_\infty} \right]^{\frac{1}{n}}, \quad (77a)$$

$$S_\infty = K^{-\frac{1}{\alpha}} \|\nabla \phi_0\|^{\frac{1-\beta}{\alpha}} Q_w^{\frac{1}{\alpha}}. \quad (77b)$$

Here, we have written  $H(S)/S$  instead of  $1/L$  to emphasize that  $N_\infty$  depends on the way that  $H$  depends on  $S$ , which is a function of the bed type.

The assumption that  $\nabla \phi \approx \nabla \phi_0$  breaks down close to the grounding line because  $N$  must reach a zero value there for water to be connected to the ocean, as given by (76c). Hence, the effective pressure decreases significantly in that area, leading to strong gradients in  $N$ . A boundary-layer analysis actually reveals that  $N \approx \phi_0$  close to the grounding line, and suggests that the effective pressure can be approximated over the whole domain by

$$N = \operatorname{erf} \left[ \frac{\sqrt{\pi}}{2} \frac{\phi_0}{N_\infty} \right] N_\infty, \quad (78)$$

One element that is lacking from the equations describing conduits is the definition of their geometry, e.g., through a relation between their thicknesses and their cross-sectional areas,  $H = H(S)$ . For **hard-bed** systems, we assume that  $L = H = \sqrt{S}$ , i.e., we consider conduits that are equally wide and thick. For **soft-bed** systems, the geometry of conduits is more challenging. For small subglacial water fluxes, water takes the form of a patchy film. When the film gets thicker due to an increased water flux, its height will exceed the thickness of the smallest clasts, so that the film will be flowing in between larger clasts that are separated by a larger distance. We introduce a factor  $F_{\text{till}}$ , defined as

$$L = F_{\text{till}} \sqrt{S}. \quad (79)$$

This deformation factor depends on the difference between ice and till viscosity, as well as the till thickness, and increases with the ability of the till to deform, provided it is sufficiently thick. For a factor  $F_{\text{till}} > 1$ , the effective pressure is lower compared to hard-bed systems. For this reason, we consider  $F_{\text{till}} = 1.1$ . For larger subglacial water fluxes, water flow channelizes into canals, for which we prescribe a thickness  $H = H_0$ . Here, we take  $H_0 = 0.1$  m as prescribed in Walder and Fowler (1994) for a sand/silt sediment type located under an ice sheet. For both inefficient and efficient cases, we then set

$$H(S) = H_0 + (\sqrt{S}/F_{\text{till}} - H_0) \exp(-Q_w/Q_c), \quad (80)$$

with  $Q_c$  a critical water flux value. Then  $H \approx \sqrt{S}/F_{\text{till}}$  if  $Q_w \ll Q_c$  and  $H \approx H_0$  if  $Q_w \gg Q_c$ . In our simulations, we take  $Q_c = 1 \text{ m}^3 \text{ s}^{-1}$ .

## 8.4 Control parameters for basal sliding and hydrology

**ctr.m** : Power sliding law exponent according to Weertman sliding law (default = 1).

**ctr.u0** : Value of  $u_0$  in the regularized Coulomb friction law. Large values (default) indicate Weertman-type sliding. (default=1e12)

**ctr.p** : Exponent for effective pressure in Weertman sliding law (default = 0).

**ctr.Asin** : Either a constant value or a matrix of size (**ctr.imax,ctr.jmax**) with coefficients of sliding parameters  $A_b$  prior to initialization. Will be overwritten if **As** is already defined in the **infile**. Note that the estimated value needs to correspond to sliding for **ctr.m=2**. An automatic scale by a factor of 1e5 is applied for other values.

**ctr.SlidAdjust** :

**0** : Basal sliding based on coefficients  $A_s$ , either constant value or optimized field (default);

**1** : As above, but basal sliding is also a function of basal temperature (within a range of **par.TrTemp** °C from the local pressure melting point) and bedrock variability **stdB** to allow for sliding in mountainous areas (only when **stdB** exists; this is also invoked in the inversion procedure).

**ctr.subwaterflow** :

**0** : no subglacial hydrology, i.e., water pressure calculated from depth of the bed below sea level (default);

**1** : runs the subglacial water flow model (subglacial hydrology) and calculates effective pressure based on subglacial water thickness;

**2** : Porous till water model (Bueler and van Pelt, 2015);

**3** : Subglacial hydrology model of Goeller et al. (2013).

**ctr.slidfac** : Multiplier to the values of **As** in the initialization to increase (value larger than 1) or decrease (value smaller than 1) sliding (default = 1.0). Note that for subsequent experiments, the multipliers add on top of each other.

**ctr.FreqHydro** : default=1

## 8.5 Global parameters for basal sliding and hydrology

**par.PoreFrac** = 0.96: Fraction of water pressure to balance ice pressure (Winkelmann et al., 2011)

**par.longcoupwater** = 5: distance (in number of ice thicknesses over which hydraulic gradient coupling takes place (only for subglacial water model)

**par.dirpp\_war** = [9 8 7 6 5 4 3 2 1]: vector for search directions in subglacial water model (based on Le Brocq et al. (2006))

**par.waterviscosity** = 1.8e-3/par.secperyear: viscosity of subglacial water

**par.NeffScale** = 5e6: scale factor for Effective Pressure to make comparison between different sliding laws possible (with and without effective pressure). In other words, when effective pressure is not used, it is set as a constant field of this value.

**par.Wdmin** = 1e-8: minimum value for the water layer **Wd** and **Wtil**

**par.Wdmax** = 0.015: maximum value for the water layer  $W_{til}$

**par.Wmax** = 2 m: maximum value for the till layer.

**par.flw0** = 1e5: maximum value for the subglacial water flux.

**par.Cdr** = 1e-3: background till drainage rate

**par.Cc** = 0.12: till compressibility (Tulaczyk et al., 2000)

**par.e0** = 0.69 reference void ratio at  $N_0$  (Tulaczyk et al., 2000)

**par.N0** = 1e3: reference effective pressure (Tulaczyk et al., 2000)

**par.sigmat** = 0.02:  $N_{til}$  lower bound, as fraction of overburden pressure

**par.convWdwPhi** = 1: convolution window for phi

**par.distChannels** = 1e4: distance between channels/canals

**par.effectHydroLimit** = 5e-4: limit for the effect of hydrology

**par.FactDefTill** = 1.1: till deformation factor

**par.alpha** = 5/4: Turbulent flow coefficient

**par.beta** = 3/2: Turbulent flow coefficient

**par.f** = 0.1: Turbulent flow coefficient

**par.hb** = 0.1: Parameter in subglacial hydrological model (Kazmierczak et al., 2024).

**par.hc** = 0.1: Parameter in subglacial hydrological model (Kazmierczak et al., 2024).

**par.Qc** = 1.0: Parameter in subglacial hydrological model (Kazmierczak et al., 2024).

## 9 Calving, hydrofracturing, sub-shelf pinning and damage

### 9.1 Preamble

This section will be further improved in future, as brittle processes will be introduced with an improved physical representation. These processes will not only include calving and hydrofracturing, but damage of ice sheets and ice shelves as well.

### 9.2 Description

In Kori–ULB, the dynamical evolution of the calving front position is defined using the level-set method (Osher and Fedkiw, 2001; Bondzio et al., 2016). The level-set method represents the continuum calving front position implicitly by a contour, or “level set,” of a so-called level-set function (LSF). This level-set function evolves according to the balance between the ice velocity perpendicular to the ice boundary and the lateral ablation rate, which is the sum of the frontal melting rate and a calving rate.

The calving rate CR may be defined by different calving laws, such as a crevasse depth law (depending on the combined penetration depths of surface and basal crevasses, relative to total ice thickness; Pollard et al., 2015; Wilner et al., 2023), a Von Mises law (depending on tensile stresses and frontal velocities; Wilner et al., 2023; Morlighem et al., 2016), or a simple minimum thickness law (Wilner et al., 2023). Those are described in more detail below.

#### 9.2.1 Crevasse-Depth Calving Law

Ice-front calving is obtained from the large scale stress field (Pollard et al., 2015), based on the horizontal divergence of the ice-shelf velocities and which is similar to parametrizations used elsewhere (Martin et al., 2011; Winkelmann et al., 2011; Levermann et al., 2012). Extensional stress is obtained via strain rate and the model SSA rheology. No distinction is made here between along-flow and transverse strains, whose combined effect is represented by ice divergence.

Dry-surface crevasse and basal crevasse depths are parameterized as

$$d_s = \frac{2}{\rho_i g} \left( \frac{\dot{\varepsilon}}{A} \right)^{1/n} \quad (81)$$

$$d_b = \left( \frac{\rho_i}{\rho_w - \rho_i} \right) \frac{2}{\rho_i g} \left( \frac{\dot{\varepsilon}}{A} \right)^{1/n} \quad (82)$$

where  $d_s$  and  $d_b$  are depths of dry-surface and basal crevasses respectively, and  $\dot{\varepsilon}$  is ice divergence. The setting of divergence  $\dot{\varepsilon}$  depends on whether the floating ice covers all or a fraction of the cell area.

A sub-grid parametrization of fractional ice area is used to set an adjusted ice thickness  $h$  and fractional cover  $f_i$ . At the ice-shelf edge adjacent to open ocean, the adjusted thickness  $h$  is the average of adjacent interior shelf thicknesses, each multiplied by a “downstream thinning” factor  $1-w[1-\exp(\Delta x/100)]$ , where the weight  $w = \min[1, h_u/(h_a \exp(-\Delta x/100))]$ , where  $\Delta x$  is the grid size in km,  $h_u$  is the unadjusted (grid-mean) ice thickness of the edge point, and  $h_a$  is the thickness of the adjacent interior point. The weight  $w$  is used to force

$h \approx h_a$  for small amounts of ice ( $h_u \ll h_a$ ), and to apply more downstream thinning when the edge cell has substantial ice cover. As in Pollard and DeConto (2012b), the fractional ice cover of the edge point is set to  $f_i = h_u/h$ , conserving ice mass.

For interior points (with  $f_i = 1$ ),  $\dot{\varepsilon}$  in Eqs. (81–82) is set to the grid-scale divergence of ice velocity  $\partial u / \partial x + \partial v / \partial y$ . For edge points (with  $f_i < 1$ ), it is set to the longitudinal spreading value for a freely floating unconfined ice face, using the adjusted ice thickness  $h$  as described above.

$$\dot{\varepsilon} = \left( \frac{\partial u}{\partial x} + \frac{\partial v}{\partial y} \right) \quad \text{for} \quad f_i = 1 \quad (83)$$

$$\dot{\varepsilon} = A \left( \frac{\rho_i g h}{4} \right)^n \quad \text{for} \quad f_i < 1 \quad (84)$$

An additional calving rate due to accumulated strain (valid for large ice shelves), is parametrized as

$$d_a = h \max[0, \ln(u/1600)] / \ln(1.2) \quad (85)$$

where  $h$  is ice thickness (adjusted as above if at the shelf edge) and  $u$  is local ice speed.  $d_a$  is zero for speeds up to 1600 m a<sup>-1</sup>, and approaches  $h$  as speeds increase to  $\sim 1900$  m a<sup>-1</sup> and above, as they do in the outer regions of the Ross and Ronne shelves.

A pragmatic constraint is imposed for thin floating ice,

$$d_t = h \max[0, \min[1, (H_{crit} - h)/50]] \quad (86)$$

where again  $h$  is ice thickness (adjusted as above if at the shelf edge), and  $d_t$  is an additional crevasse depth. This simply has the effect of removing floating ice thinner than  $H_{crit}$  (here given a default value of 200 m), and reduces unrealistic areas of thin ice extending seaward of the modern Ross and Filchner–Ronne calving fronts, where they are not limited by Eq. (85). It has the side-effect of not allowing thin ice shelves to grow from small tide-water glaciers, which may be unrealistic in some cases but does not noticeably affect the large-scale modern and “retreat” simulations.

Surface crevasses containing water are deepened due to the additional opening stress of the liquid by an amount  $d_{wa}$ , where  $d_{wa}$  is  $(\rho_w / \rho_i)$  times the depth of water drained into the crevasse from mobile surface melt and/or rainfall.  $d_{wa}$  (m) is simply set to

$$d_{wa} = 100R^2 \quad (87)$$

where  $R$  is the annual surface melt plus rainfall available after refreezing in the surface mass balance scheme.

The overall calving rate  $C_r$  (in m a<sup>-1</sup>) is expressed as:

$$C_r = M_{max} \max[0, \min[1, (r - r_c)/(1 - r_c)]] \quad (88)$$

where  $M_{max}$  is the maximum migration rate of the ice front (set to 3000 Pollard et al., 2015),  $r$  is the ratio of the combined crevasse depths to ice thickness  $[d_s + d_b + d_a + d_t + d_{wa}] / h$ , and  $r_c$  is a critical value for calving onset, set to 0.75 (Pollard et al., 2015).

### 9.2.2 Divergence-based Calving Law

Following Pollard and DeConto (2012b), the calving rate may be defined as

$$C_r = H_{min}(1 - w_c) + M_{max} \max\left(\frac{\partial u}{\partial x} + \frac{\partial v}{\partial y}, 0\right) \quad (89)$$

where  $w_c = \min(1, h_e/200)$  is a weight factor,  $h_{min}$  is the minimum ice thickness applied to avoid too thin ice shelves (here  $h_{min}=30$ ), and  $M_{max}$  is the maximum migration rate of the ice front (here 3000).

### 9.2.3 Von Mises Calving Law

Within the von Mises (VM) calving law, the calving rate  $c$  is proportional to the tensile stress regime at the ice front, i.e.,

$$C_r = |\mathbf{u}| \frac{\tilde{\sigma}}{\sigma_{max}}, \quad (90)$$

where  $\mathbf{u}$  is the ice front velocity vector,  $\tilde{\sigma}$  is the total tensile von Mises stress at the ice front, and  $\sigma_{max}$  is the tensile stress threshold (a tuning parameter for VM).

The von Mises stress  $\tilde{\sigma}$  is defined as

$$\tilde{\sigma} = \sqrt{3} A \tilde{\varepsilon}_e^{1/n}, \quad (91)$$

where  $A$  is the temperature-dependent flow-rate factor,  $n$  is Glen's flow law exponent (taken here to be  $n = 3$ ), and  $\tilde{\varepsilon}_e$  is the effective tensile strain rate.

The effective tensile strain rate is computed from the eigenvalues of the 2D horizontal strain rate tensor,  $\dot{\varepsilon}_1$  and  $\dot{\varepsilon}_2$ , following Morlighem et al. (2016):

$$\tilde{\varepsilon}_e = \frac{1}{2} \left[ \max(0, \dot{\varepsilon}_1)^2 + \max(0, \dot{\varepsilon}_2)^2 \right]. \quad (92)$$

Without considering any additional undercutting at the ice front, retreat occurs when  $\tilde{\sigma} > \sigma_{max}$ , and advance occurs when  $\tilde{\sigma} < \sigma_{max}$ .

### 9.2.4 Thickness-dependent Calving Law

In the thickness-dependent calving law, the calving rate  $C_r$  depends on the ice thickness  $H$  at the calving front. It is defined as:

$$C_r = \max\left(0, 1 + \frac{H_{crit} - H}{H_{crit}}\right) |\mathbf{u}|, \quad (93)$$

where  $H_{crit}$  is the critical thickness threshold, and  $|\mathbf{u}|$  is the ice front velocity magnitude.

When the ice thickness falls below  $H_{crit}$ , the calving rate increases, reaching a maximum when  $H = 0$ . In contrast,  $C_r$  becomes zero when  $H \geq H_{crit}$ .

## 9.3 Control parameters for calving

**ctr.calving :**

**0** : no calving, i.e., ice shelves will extend to the edge of the model domain (default)

- 1** : Imposition of a constant calving rate of value `ctr.CR`
- 2** : Imposition of a constant change rate `ctr.WV` in front position, i.e.,  $CR=U-ctr.WV$ .  
Note that `ctr.WV` (defalut) will fix the calving front position to be unmoving.
- 3** : Apply divergence-based calving law according to Pollard and DeConto (2012a);
- 4** : Apply crevasse-depth calving law according to Pollard et al. (2015);
- 5** : Apply Von Mises calving law;
- 6** : Apply thickness-dependent calving law;
- 7** : CalvingMIP periodic forcing, where `ctr.CR_AMP` is the max rate of front position change.

**ctr.HydroFrac :**

- 0** : no hydrofracturing (i.e.,  $d_{wa} = 0$ ; default)
- 1** : Apply hydrofracturing according to Pollard et al. (2015, equation (87)) (to be used together with `ctr.calving=4`);

**ctr.LimitFront :**

- 0** : the calving front can advance beyond initial position (default)
- 1** : the calving front cannot advance beyond initial position ;

**ctr.FrontalMelt** : Critical thickness threshold (default value of 200m). Used in `ctr.calving=4` and `ctr.calving=6`.

**ctr.taulim** : Tensile stress threshold in Von Mises calving (default value of 150 kPa)

**ctr.FrontalMelt :**

- 0** : No frontal melting (default)
- 1** : Adds frontal melting to calving rate ;

**ctr.Hcrit** : Critical ice thickness for the calving scheme (default=200 m)

**ctr.CR** : Direct and constant imposition of calving rate (default=0).

**ctr.WV** : Direct, constant imposition of change in front positon. `ctr.WV=0` will fix the calving front position to be unmoving (default=0).

**ctr.damage** : Activate damage in ice sheet and ice shelf when set to 1 (default=0)

**ctr.TRdam** : Compute advected damage field (default=0).

**ctr.THdam** : Compute thinning component in damage field (default=0).

**ctr.SFdam** : Include surface damage (default=0). **Should we have this term to be default to 1?**

**ctr.BSdam** : Include basal damage (default=0).

## 9.4 Global parameters for calving

**par.MinCalvThick** : Minimum ice thickness applied to avoid too thin ice shelves in m  
(default=30; used in `ctr.calving=3`)

**par.MaxCalvRate** : Maximum migration rate of the ice front in  $\text{m a}^{-1}$  (default: 3000; used in `ctr.calving=3` and `ctr.calving=4`).

**par.CritCrevasse** : Critical ratio for calving onset in Crevasse-Depth Calving law (default: 0.75; used in `ctr.calving=4`)

**par.LSFreset** : Amount of timestep after which the Level Set Function is reset (for stability; default: 30)

**par.ShelfPinning** :

**0** : No sub-shelf pinning;

**1** : Sub-shelf pinning of ice shelves based on local bedrock variability `stdB` and water column depth (only when `stdB` exists).

**par.Ucrit1** = 1600: Parameter in DeConto and Pollard (2016) crevasse algorithm for additional crevasse formation.

**par.Ucrit2** = 1900: Parameter in DeConto and Pollard (2016) crevasse algorithm for additional crevasse formation.

**par.damlim** = 0.9: Limit on damage (% of ice thickness).

## 10 Glacial Isostatic Adjustment (GIA)

As a first approximation, the equilibrium vertical displacement of the lithosphere in response to an ice loading is described as the equilibrium vertical displacement of a horizontal linear elastic plate subject to a transverse load. In order to represent the viscous asthenosphere underneath the lithosphere, it is also assumed that this plate lies on a viscous substratum. This representation of the lithosphere is considered for instance in the commonly used elastic lithosphere-relaxing asthenosphere (ELRA) model in glaciology.

### 10.1 Bedrock deformation for a plate with constant thickness

Consider a thin rectangular plate with constant thickness  $h$  (and infinite horizontal dimension). The mechanical properties of the plate are given by its Young's modulus  $E$  and its Poisson's ratio  $\nu$  (both properties are assumed to be constant). The plate is subjected to a transverse load  $q_b$ . Let  $w_b$  be the normal displacement of the plate (also called the deflection). For a thin rectangular plate, it is assumed that the shear strains  $\epsilon_{xz}$  and  $\epsilon_{xy}$  and the normal strain  $\epsilon_{xx}$  is negligible, where we denoted the strain tensor by  $\epsilon$ . In this context and using a Hooke's law in linear elasticity (the plate is assumed to behave like a linear elastic material), the components  $\sigma_{xx}$ ,  $\sigma_{yy}$  and  $\sigma_{xy}$  of the stress tensor are given by

$$\sigma_{xx} = \frac{E}{1 - \nu^2} (\epsilon_{xx} + \nu \epsilon_{yy}) \quad (94)$$

$$\sigma_{yy} = \frac{E}{1 - \nu^2} (\epsilon_{yy} + \nu \epsilon_{xx}) \quad (95)$$

$$\sigma_{xy} = \frac{1}{2} G \epsilon_{xy} \quad (96)$$

where  $G = \frac{E}{2(1+\nu)}$  is the shear modulus. In the context of thin rectangular plates, these stress components can be written as:

$$\sigma_{xx} = -\frac{Ez}{1 - \nu^2} \left( \frac{\partial^2 w_b}{\partial x^2} + \nu \frac{\partial^2 w_b}{\partial y^2} \right) \quad (97)$$

$$\sigma_{yy} = -\frac{Ez}{1 - \nu^2} \left( \frac{\partial^2 w_b}{\partial y^2} + \nu \frac{\partial^2 w_b}{\partial x^2} \right) \quad (98)$$

$$\sigma_{xy} = -\frac{Ez}{1 + \nu} \frac{\partial^2 w_b}{\partial x \partial y} \quad (99)$$

where the vertical coordinate  $z$  is measured from the middle surface of the plate. The resulting twisting (or torsion) moments  $M_{xx}$  and  $M_{yy}$  and bending moment  $M_{xy}$  (equal to  $M_{yx}$ ) are given by

$$M_{xx} = \int_{-h/2}^{h/2} \sigma_{xx} z dz = -D \left( \frac{\partial^2 w_b}{\partial x^2} + \nu \frac{\partial^2 w_b}{\partial y^2} \right) \quad (100)$$

$$M_{yy} = \int_{-h/2}^{h/2} \sigma_{yy} z dz = -D \left( \frac{\partial^2 w_b}{\partial y^2} + \nu \frac{\partial^2 w_b}{\partial x^2} \right) \quad (101)$$

$$M_{xy} = \int_{-h/2}^{h/2} \sigma_{xy} z dz = -D(1-\nu) \frac{\partial^2 w_b}{\partial x \partial y} \quad (102)$$

where

$$D = \frac{Eh^3}{12(1-\nu^2)} \quad (103)$$

is the flexural rigidity of the plate. Writing the equilibrium of forces and moments for the plate, it can be shown that the twisting and bending moments satisfy the following differential equation:

$$\frac{\partial^2 M_{xx}}{\partial x^2} + 2 \frac{\partial^2 M_{xy}}{\partial x \partial y} + \frac{\partial^2 M_{yy}}{\partial y^2} = -q_b \quad (104)$$

Substituting Eqs. (100)–(102) into Eq. (104) gives the following partial differential equation for the deflection  $w_b$ :

$$\begin{aligned} \frac{\partial^2}{\partial x^2} \left( -D \left( \frac{\partial^2 w_b}{\partial x^2} + \nu \frac{\partial^2 w_b}{\partial y^2} \right) \right) + 2 \frac{\partial^2}{\partial x \partial y} \left( -D(1-\nu) \frac{\partial^2 w_b}{\partial x \partial y} \right) + \\ \frac{\partial^2}{\partial y^2} \left( -D \left( \frac{\partial^2 w_b}{\partial y^2} + \nu \frac{\partial^2 w_b}{\partial x^2} \right) \right) = -q_b \end{aligned} \quad (105)$$

or as  $D$  is assumed to be constant and  $\nu$  is constant,

$$-D \left( \frac{\partial^4 w_b}{\partial x^4} + 2\nu \frac{\partial^4 w_b}{\partial x^2 \partial y^2} + \frac{\partial^4 w_b}{\partial y^4} \right) - 2D(1-\nu) \frac{\partial^4 w_b}{\partial x^2 \partial y^2} = -q_b \quad (106)$$

that leads to

$$D \left( \frac{\partial^4 w_b}{\partial x^4} + 2 \frac{\partial^4 w_b}{\partial x^2 \partial y^2} + \frac{\partial^4 w_b}{\partial y^4} \right) \equiv D \nabla_x^4 w_b = q_b \quad (107)$$

## 10.2 Plate with constant thickness on a viscous substratum

We consider now that the plate lies on a viscous substratum with density  $\rho_b$ , which is the upper mantle density. In this case, we must account for the buoyancy force (which depends on the vertical displacement  $w_b$ ) that the lithosphere experiences in the underlying viscous substratum. The buoyancy force acts to reduce the exerted force  $q_b$  by an amount  $\rho_b g w_b$ . Then, Eq. (107) writes in the presence of a viscous substratum as (Huybrechts and de Wolde, 1999; Pollard and DeConto, 2012a)

$$D \nabla_x^4 w_b + \rho_b g w_b = q_b \quad (108)$$

The load  $q_b$  is then defined by

$$q_b = \rho_i g h + \rho_s g h_w - \rho_i g h^{\text{eq}} - \rho_s g h_w^{\text{eq}}, \quad (109)$$

where  $h_w$  is the ocean column thickness, and  $h^{\text{eq}}$  and  $h_w^{\text{eq}}$  are the values of ice thickness and ocean column thickness in equilibrium, respectively, taken from modern observed fields.

Equation (108) is solved by a Green's function (Huybrechts and de Wolde, 1999). The response to a point load  $P_b$  ( $q_b \times$  area) versus distance from the point load  $l$  is then given by

$$w_p(l) = \frac{P_b L_w^2}{2\pi D} \text{kei}\left(\frac{l}{L_w}\right), \quad (110)$$

where  $\text{kei}$  is a Kelvin function of zeroth order (defined as the imaginary part of a modified Bessel function of the second kind), and  $L_w = (D/\rho_b g)^{1/4}$  is the flexural length scale. For any load, the different values of the point loads  $w_p$  are summed over all grid cells to yield  $w_b(x, y)$ .

### 10.3 Plate with spatially-varying thickness

Let us consider in this section a thin rectangular plate having a spatially-varying thickness  $h(x)$ . As previous, the plate is assumed to behave as a linear elastic material with constant Young's modulus  $E$  and Poisson's ratio  $\nu$ . The plate is subjected to a transverse load  $q_b$  that induces a deflection  $w_b$  of the plate. We assume that the above thickness varies gradually and there is no abrupt variation in thickness so that the expressions for the bending and twisting moments derived earlier for plates of constant thickness (100)–(102) also apply with sufficient accuracy to the case of a thin rectangular having a spatially-varying thickness. Please note that in this case, the flexural rigidity  $D$  is therefore spatially varying, i.e.,

$$D = D(\mathbf{x}) = \frac{Eh(\mathbf{x})^3}{12(1-\nu^2)} \quad (111)$$

Substituting Eqs. (100)–(102) with the spatially-varying flexural rigidity  $D(x)$  into Eq. (104) gives the following partial differential equation for the deflection  $w_b$ :

$$\begin{aligned} & D\nabla_x^4 w_b + 2\frac{\partial D}{\partial x}\frac{\partial}{\partial x}(\nabla_x^2 w_b) + 2\frac{\partial D}{\partial y}\frac{\partial}{\partial y}(\nabla_x^2 w_b) + \nabla_x^2 D(\nabla_x^2 w_b) \\ & - (1-\nu)\left(\frac{\partial^2 D}{\partial x^2}\frac{\partial^2 w_b}{\partial y^2} - 2\frac{\partial^2 D}{\partial x \partial y}\frac{\partial^2 w_b}{\partial x \partial y} + \frac{\partial^2 D}{\partial y^2}\frac{\partial^2 w_b}{\partial x^2}\right) + \rho_b g w_b = q_b \end{aligned} \quad (112)$$

In this case, Eq. (112) is solved using numerical methods instead of Green's functions.

### 10.4 Time-dependent bedrock response

The actual rate of change in bedrock elevation is given by a simple relaxation scheme:

$$\frac{\partial b}{\partial t} = -\frac{1}{\tau_w}(b - b^{\text{eq}} + w_b), \quad (113)$$

where  $b$  is the actual bedrock elevation,  $b^{\text{eq}}$  is the elevation in equilibrium (taken from modern observed fields), and  $\tau_w = 3000$  year (Pollard and DeConto, 2012a). Also here, we introduced spatially-varying values for  $\tau_w$ , based on viscosity variations of the upper asthenosphere (Coulon et al., 2021).

## 10.5 Geoid changes

A major drawback of the ELRA approximation is that it does not account for local perturbations in the height of the sea surface, thus missing an important feedback process. We therefore implemented an approximation of gravitationally-consistent non-uniform sea-level variations due to regional mass changes  $m_G$ , here expressed as

$$m_G = \rho_i h + \rho_w h_w + \rho_a b - \rho_i h_0 - \rho_w h_{w,0} - \rho_a b_0. \quad (114)$$

The distribution of mass changes ( $m_G$ ) is influenced by changes in the ice and/or ocean column (depending on whether a specific location is covered by grounded ice or by ocean water) as well as by changes in bedrock elevation. Mass changes associated with bed elevation change are calculated assuming asthenosphere density, noting that the perturbation in gravitational attraction due to ice and ocean mass changes will be somewhat counterbalanced by the gravitational effect of the subsequent solid-Earth deformation, which arises due to the displacement of mantle material below the lithosphere.

For a unit point mass, the perturbation in the geoid is approximated by

$$N(\theta) = \frac{R_e}{M_e} \left( \frac{1}{2 \sin(\theta/2)} \right), \quad (115)$$

where  $N(\theta)$  is a geoid Green's function,  $R_e$  the Earth radius,  $M_e$  the Earth mass, and  $\theta$  the spherical distance from the load point. Note that equation (115) considers a spherical Earth. This expression is convoluted with the distribution of mass changes  $m_G$  in order to obtain the change in geoid height  $P$  compared to the initial sea-surface height  $SL_0$  (taken here as present-day sea level). In order to capture the entire geoid perturbation, this convolution is realized over an extended ocean domain. Local sea surface changes are then calculated as the sum of the geoid perturbation  $P$ , the barystatic sea-level contribution arising from Antarctic ice mass changes (Goelzer et al., 2020, *SLC*, calculated as in) and a mass conservation term  $C$ , which is a spatial constant that must be added to the solution in order to conserve oceanic mass (Coulon et al., 2021). Note that since we calculate geoid changes between discrete configurations of the ice–earth–ocean systems, we approximate the perturbation of the geoid using Green's functions of geoid for a rigid Earth Farrell and Clark (1976). In studies that solve the full sea-level equation, self-consistent solutions for geoid and solid Earth perturbations are determined iteratively using Green's functions for a deforming Earth. This approach would significantly increase the computation time of our model and would only lead to a small increase in accuracy. The geoid model defined here only considers gravitational changes directly or indirectly due to changes in Antarctic ice-sheet cover (Figure 10). Sea-level contributions stemming from ice masses other than the AIS are not considered. The feedback due to Earth rotational effects is also neglected. The result influences the position of the grounding line and may retard grounding line retreat due to mass loss of ice sheets (Coulon et al., 2021).

## 10.6 Control parameters for GIA and geoid changes

**ctr.BedAdj :**

**0** : no isostatic bedrock adjustment (default);

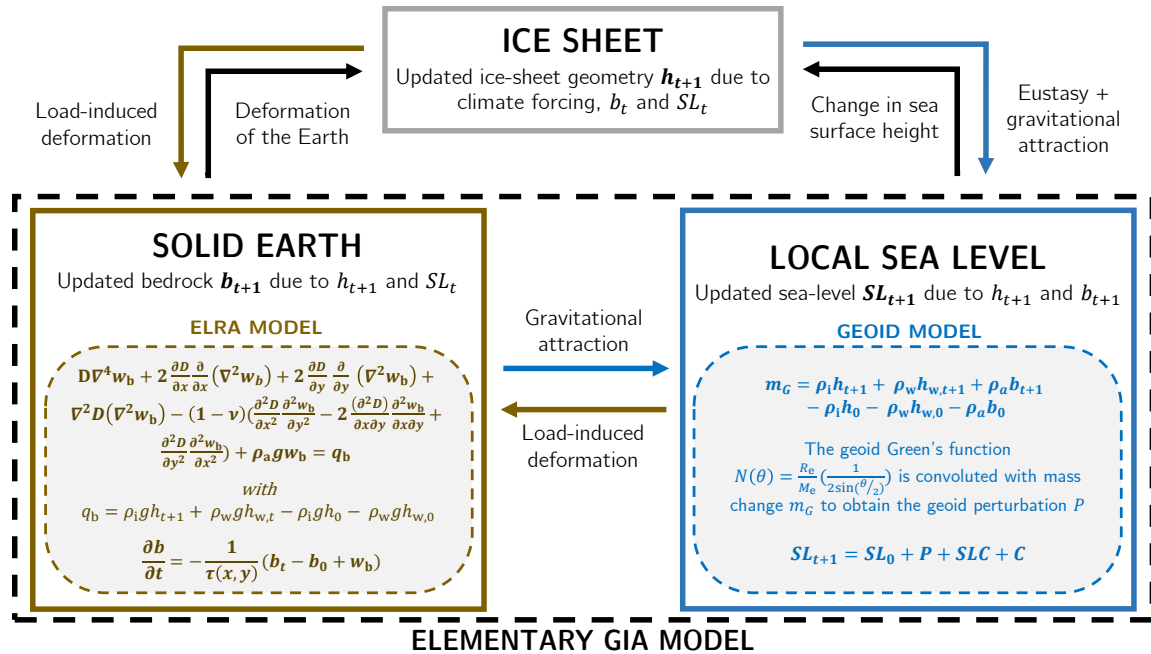


Figure 10: Interactions between the ice sheet, the local sea level, and the solid Earth in the regional coupled system as calculated in Kori–ULB and described in Coulon et al. (2021). In the solid-Earth system,  $D(x, y)$  is the flexural rigidity of the lithosphere,  $\nu$  the lithospheric Poisson's ratio,  $w_b$  the equilibrium deflection of the lithosphere,  $q_b$  the applied load,  $g$  the gravitational acceleration, and  $\tau(x, y)$  the relaxation time of the asthenosphere. In addition,  $\rho_i$ ,  $\rho_w$ , and  $\rho_a$  are the ice, ocean water, and asthenosphere densities, respectively. The ocean column thickness at time steps  $t$  and  $t + 1$  are  $h_{w,t} = SL_t - b_t$  and  $h_{w,t+1} = SL_t - b_{t+1}$ , respectively, while  $h_t$  and  $h_{t+1}$  are the ice thicknesses at time  $t$  and  $t + 1$  and  $h_0$  and  $h_{w,0}$  are the initial ice and ocean column thicknesses. Similarly,  $b_0$  is the initial bedrock elevation and  $b_t$  and  $b_{t+1}$  the ones at time  $t$  and  $t + 1$ . In the local sea-level system,  $R_e$  and  $M_e$  are the Earth radius and mass, respectively, and  $\theta$  is the spherical distance from the load.  $SLC$  is the barystatic sea-level contribution due to ice sheet mass changes, and  $C$  is a mass conservation term.

**1** : isostatic adjustment of bedrock. If spatially-varying flexural rigidity ( $D_b$ ) and relaxation time ( $\text{bedrelax}$ ) fields are provided as inputs in `infile`, the modified ELRA model is used (Figure 10). Otherwise, the Green’s function formalism with is used with uniform solid Earth properties;

**2** : local isostatic bed adjustment.

**ctr.GeoidCalc :**

**0** : Local sea level changes not taken into account (default);

**1** : Calculate height of the geoid (local sea level) compared to initial state, based on mass changes of the ice sheet (Figure 10).

## 10.7 Global parameters for GIA and geoid changes

**par.rhom** = 3370 kg m<sup>-3</sup>: Mantle density.

**par.FlexRigid** = 1e25: Flexural rigidity of the lithosphere (Pa m<sup>3</sup>); its value is defined by

$$D_b = \frac{E h_e^3}{12(1 - \nu^2)}$$

where  $E$  is Young’s modulus (100 GPa),  $\nu$  is Poisson’s ratio (0.25), and  $h_e$  is the effective elastic lithosphere thickness (Chen et al., 2017)

**par.bedrelax** = 3000: Relaxation time of the asthenosphere (year) as nominal value (used when  $\text{Btau}$  is not defined).

**par.nuB** = 0.25: Poisson coefficient in the full derivation of lithospheric deformation.

**par.Re** = 6.3781e6: Radius of the Earth

**par.Me** = 5.972e24: Mass of the Earth

**par.Aoc** = 3.618e14: Global ocean surface

**par.geoidist** = 5000e3: size of the convolution filter over which fingerprinting is calculated (m)

**par.rhof** = 1000: fresh water density

**par.SLref** = 0: reference sea level

## 11 Grounding-line flux condition for power-law sliding

### 11.1 Description

Previous studies have indicated that it is necessary to resolve the transition zone/boundary layer at sufficiently fine resolution in order to capture grounding-line migration accurately (Durand et al., 2009; Pattyn et al., 2012, 2013; Pattyn and Durand, 2013; Durand and Pattyn, 2015). In large-scale models, this can lead to unacceptably small time-steps and costly integrations. Pollard and DeConto (2009, 2012a) incorporated the boundary layer solution of Schoof (2007) directly in a numerical ice-sheet model at coarse grid resolution, so the flux,  $q_g$ , across model grounding lines is given by

$$q_g = \left[ \frac{A(\rho_i g)^{n+1} (1 - \rho_i / \rho_s)^n A_b'^{1/m}}{4^n} \right]^{\frac{m}{m+1}} \Theta^{\frac{nm}{m+1}} h_g^{\frac{m(n+3)+1}{m+1}}. \quad (116)$$

This yields the vertically averaged velocity  $u_g = q_g/h_g$  where  $h_g$  is the ice thickness at the grounding line.  $\Theta$  in Eq. (116) accounts for back stress at the grounding line due to buttressing by pinning points or lateral shear, and is defined as

$$\Theta = \frac{b_f \tau_{xx} + (1 - b_f) \tau_f}{\tau_f}, \quad (117)$$

where  $\tau_{xx}$  is the longitudinal stress just downstream of the grounding line, calculated from the viscosity and strains in a preliminary SSA solution without constraints given by Eq. (116), and  $\tau_f$  the free-water tensile stress defined by

$$\tau_f = \frac{1}{2} \rho_i g h \left( 1 - \frac{\rho_i}{\rho_s} \right). \quad (118)$$

The parameter  $b_f$  is an additional buttressing factor to control the buttressing strength of ice shelves and may be varied between 0 (no buttressing) and 1 (full buttressing). All experiments in this paper use  $b_f = 1$ , except the sensitivity experiments on ice-shelf de-buttressing where  $b_f$  is set to zero. Grounding-line ice thickness  $h_g$  is linearly interpolated in space by estimating the sub-grid position of the grounding line between the two surrounding floating and grounded  $h$ -grid points. Therefore, the height above floatation is linearly interpolated on the Arakawa C-grid between those two points to where it is zero. Subsequently, the bedrock elevation is linearly interpolated to that location, and the floatation thickness of ice for that bedrock elevation and current sea level is obtained (Pattyn et al., 2006; Gladstone et al., 2010; Pollard and DeConto, 2012a). The velocity  $u_g$  is then calculated at the grounding-line points and imposed as an internal boundary condition for the flow equations, hence overriding the large-scale velocity solution at the grounding line.  $u_g = q_g/h_g$  is imposed exactly at the  $u$ -grid grounding line point when the flux  $q_g$  is greater than the large-scale sheet-shelf equation's flux at the grounding line.

Equation (116) applies equally to the  $y$  direction, with  $v_g$  and  $\tau_{yy}$  instead of  $u_g$  and  $\tau_{xx}$ . Note that spatial gradients of quantities parallel to the grounding line, which are not included in Schoof's flow-line derivation of Eq. (116), are neglected here (Katz and Worster, 2010; Gudmundsson et al., 2012; Pattyn et al., 2013). This parametrization was also found to yield results comparable to SSA models solving transient grounding line migration at high spatial

resolution of the order of hundreds of meters (Pattyn and Durand, 2013; Durand and Pattyn, 2015), despite the fact that Eq. (116) applies to steady-state conditions.

The use of the above-described flux condition has been analysed and criticised by Reese et al. (2018b), claiming non-physical behaviour of the buttressing factor in the flux condition. However, Reese et al. (2018b) only considered ice-sheet diagnostics, as negative values of buttressing vanish when the ice sheet is allowed to change over time. As a precaution, we limit anyway  $0 \leq \Theta \leq 1$ .

The ice sheet model Kori also allows for modelling separate drainage basins at high resolution. In this case the SGL condition is not applied at all.

## 11.2 Control parameters for grounding-line flux

**ctr.schoof :**

**0** : no grounding line flux correction (default);

**1** : grounding line migration according to Schoof (2007), only for coarse model resolutions;

**ctr.radnorm** : default=50

## 12 Model initialization

### 12.1 Methodology

Model initialization can be done in different ways. One particular approach is to match the initial state of the ice sheet as close as possible to the observed one. Here we use this approach with the method from Pollard and DeConto (2012b) by optimizing basal sliding coefficients in an iterative fashion to allow for the ice thickness to match as closely the observed ice thickness. It is a two-step approach, where first the model is run forward in time using SIA without ice shelves (or grounding line flux condition), starting from modern observed bed and ice surface elevations and driven by the observed climatology (surface mass balance and temperature). Full thermomechanical coupling and temperature evolution, isostatic bedrock adjustment, and sub-grid ice-shelf pinning can equally be considered. Basal sliding coefficients  $A_b(x, y)$  are initialized with a constant value (e.g.,  $A_b = 3 \times 10^{-9} \text{ m a}^{-1} \text{ Pa}^{-2}$  for the Antarctic ice sheet). This value is a nominal value for  $m = 2$  and scaled for different values of  $m$  through a scaling factor that is multiplied with  $A_b$

$$A_{\text{scale}} = 10^{5(2-m)} \quad (119)$$

At intervals of  $\Delta t_{\text{inv}}$  years, at each grounded ice grid point, the local basal sliding coefficients  $A_b(x, y)$  in Eq. (60) are adjusted by a multiplicative factor (Pollard and DeConto, 2012b):

$$A_b^* = A_b \times 10^{\Delta z}, \quad (120)$$

for  $\Delta z \leq \Delta z^0$ .  $\Delta z$  is defined as

$$\Delta z = \max \left[ -1.5, \min \left( 1.5, \frac{h_s - h_s^{\text{obs}}}{h_s^{\text{inv}}} \right) \right], \quad (121)$$

and  $\Delta z^0$  is its value from the previous iteration step,  $h_s^{\text{obs}}$  is the observed ice surface elevation and  $h_s^{\text{inv}}$  is a scaling constant. This means that the optimization of a local point is halted whenever its change  $\Delta z$  is larger than the one of the previous iteration step (Bernalles et al., 2017). During the inversion procedure, basal temperature is still allowed to influence sliding. Adjusted  $A_b^*(x, y)$  values are limited by defined limit values that take into account dependency on sliding law power coefficients  $m$  in Eq. (57). Values for  $A_b^*$  are only updated when  $r > 0$  in Eq. (60), so that they are kept unchanged for ice temperatures below a certain limit.

In addition to Pollard and DeConto (2012b) we also introduce a regularization term that essentially smooths high-frequency noise in the basal sliding coefficients by using a Gaussian smoothing filter. The filter is only applied across the grounded domain with the exception of grid cells where the bedrock elevation is higher than 1000 m above present-day sea level and the roughness of the bedrock is above the 99% percentile of the total roughness of the domain. Contrary to Pollard and DeConto (2012b), the revised algorithm only requires about 50 000 years of forward integration to obtain an optimized friction field.

The second step consists of running the model with ice shelves (and grounding line flux condition if pertinent) using the HySSA velocity calculation. In addition to constraining the basal slip coefficients, melt/accretion rates under the floating ice shelves are updated using the method of Bernalles et al. (2017).

## 12.2 Control parameters for optimization

**ctr.inverse :**

**0** : normal forward model run (default);

**1** : optimization of basal sliding coefficients  $A_s$  for the grounded ice sheet with fixed grounding line position.

**2** : optimization of basal sliding coefficients  $A_s$  for the grounded ice sheet and sub-shelf melt/accretion for floating ice shelves.

**ctr.Hinv** : Scale factor on iterative optimization of ice thickness (Pollard and DeConto, 2012b). Default = 500.

**ctr.Tinv** : Time interval between updates in the optimization scheme (Pollard and DeConto, 2012b). Default = 200. For basin calculations, the value should be set lower (10 for instance) in order to reduce the run time.

**ctr.HinvMelt** : Scale factor on iterative optimization of ice thickness for ice shelves (Pollard and DeConto, 2012b). Default = 100.

**ctr.TinvMelt** : Time interval between updates in the optimization scheme (Pollard and DeConto, 2012b). Default = 50.

**ctr.stopoptim** : Fraction of total time at the end of the initialization run where updates of basal friction coefficients are not applied anymore (default=0.1)

## 12.3 Global parameters for optimization

**par.stdDevRegul** = 3.5: standard deviation of the Gaussian filter for the regularization in grid cells. For **ctr.basin**=1, the value is taken as **par.stdDevRegul** + 1.

**par.invmin** = 1.e-10 (for  $m = 2$ ): Minimum value of  $A_s$  in optimization scheme. **par.AsScale** is employed for scaling with other values of **ctr.m**

**par.invmax** = 1.e-3 (for  $m = 2$ ): Maximum value of  $A_s$  in optimization scheme. **par.AsScale** is employed for scaling with other values of **m**

**par.invmaxncor** = 1.e-5; used in the initialization of the optimization.

**par.AsFroz** = 1e-11 (for  $m = 2$ ): Minimum value of  $A_s$  corresponding to frozen bed conditions (should be different from zero to avoid division by zero); **par.AsScale** is employed for scaling with other values of **m**

**par.AsScale** =  $(1e5)^{2-m}$ : scaling factor for other values of **ctr.m** different from 2

## 12.4 Example: Initialization of the Antarctic ice sheet

The following example shows how to initialize an ice sheet, and the Antarctic ice sheet in particular. This allows to illustrate the two-step initialization procedure. The first step being an optimization of basal sliding coefficients underneath the grounded ice sheet using the SIA model and a fixed grounding line; the second being an optimization of both basal sliding coefficients and sub-shelf melt/accretion rates using the hybrid SSA/SIA model. To compare the different approaches, we start with establishing a steady-state ice sheet without optimization and without ice shelves (SIA and fixed grounding line).

The example below shows a basic thermomechanically-coupled run of the Antarctic ice sheet on a 25 grid size resolution. The file `BedMachine25km.mat` contains the observed ice thickness ( $H_0$ ) and bedrock elevation ( $B_0$ ) of the ice sheet on 25 km resolution, resampled from BedMachine v2 (Morlighem et al., 2019), surface mass balance ( $M_b$ ) and temperature ( $T_s$ ), resampled at the same resolution and obtained from regional climate models, and geothermal heat flux ( $G$ ). For a thermomechanical coupled run, these are the basic data needed. For validation purposes, the observed velocity components ( $v_x, v_y$ ) were added to the input file. The script shows three consecutive runs, i.e., (i) a simple steady state run starting from the input data, (ii) the first optimization for the grounded ice sheet only, and (iii) the second optimization with the hybrid model.

```
% Steady-state run of the Antarctic ice sheet
% 25 km spatial resolution

ctr.imax=225;
ctr.jmax=225;
ctr.kmax=21;
ctr.delta=25.e3;
ctr.nsteps=8001;
ctr.dt=10;
ctr.Tcalc=2;
ctr.Tinit=1; % SET 1 FOR INITIALIZATION !
ctr.Asin=3e-9;
ctr.Ao=5.0e-17;
ctr.m=3;
KoriModel('Bedmachine25km', 'INIT25a', ctr);

% First optimization
ctr.inverse=1;
KoriModel('Bedmachine25km', 'INIT25b', ctr);

% Second optimization
ctr.inverse==2;
ctr.Tinit=0 % important as the temperature field is calculated
ctr.SSA=2; % hybrid model
ctr.shelf=1; % add ice shelves
ctr.schoof=1; % flux condition due to coarse grid
ctr.calving=4; % keep calving front at observed position
ctr.dt=0.2; % smaller time step
ctr.nsteps=10001; % more iterations
KoriModel('INIT25b', 'INIT25c', ctr);
```

Figures 11 and 12 display the difference between modelled and observed ice thickness

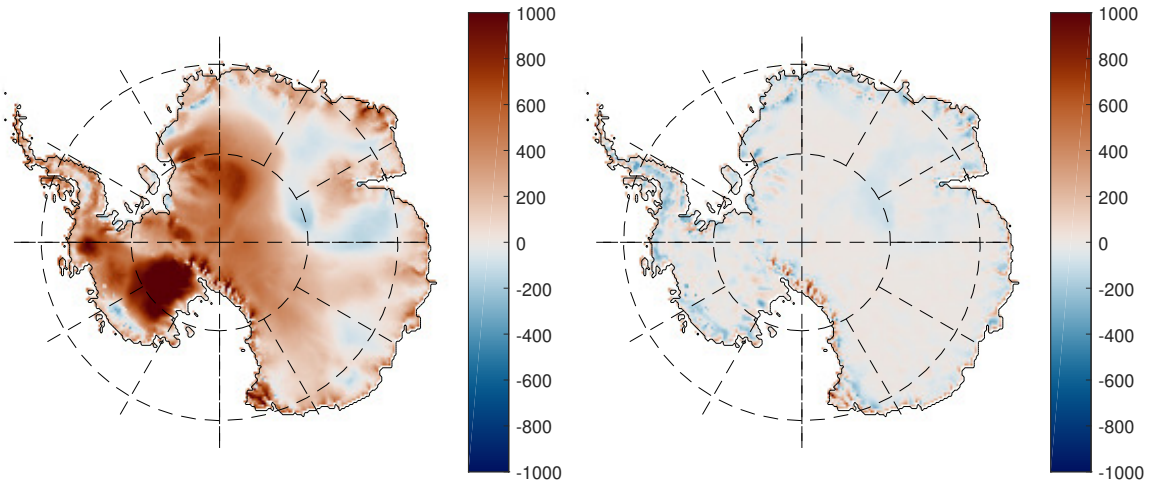


Figure 11: Difference in ice thickness between a steady-state thermomechanical coupled ice sheet, for constant value of basal sliding coefficients, with the observed ice thickness (left), and when basal sliding coefficients are optimized using the nudging method `ctr.inverse` = 1 (right).

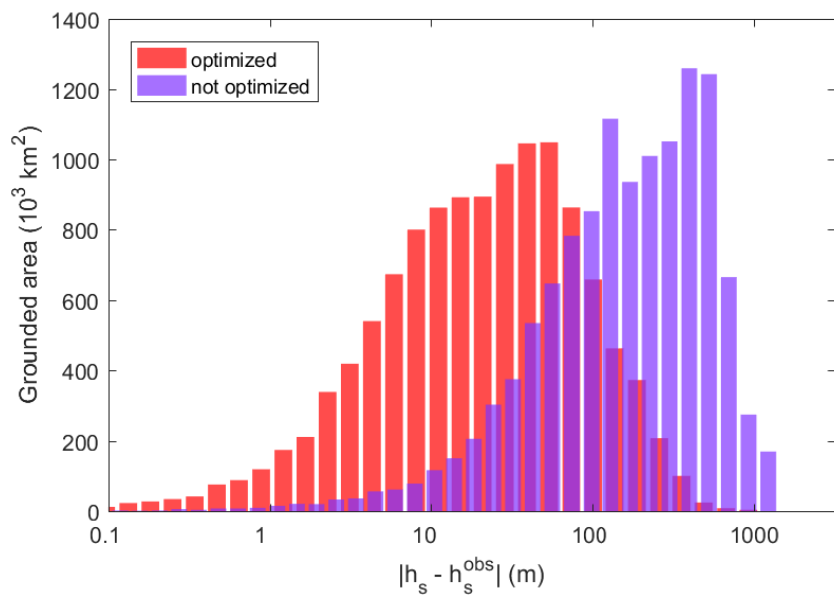


Figure 12: Histogram of surface elevation difference for the experiments shown in Figure 11.

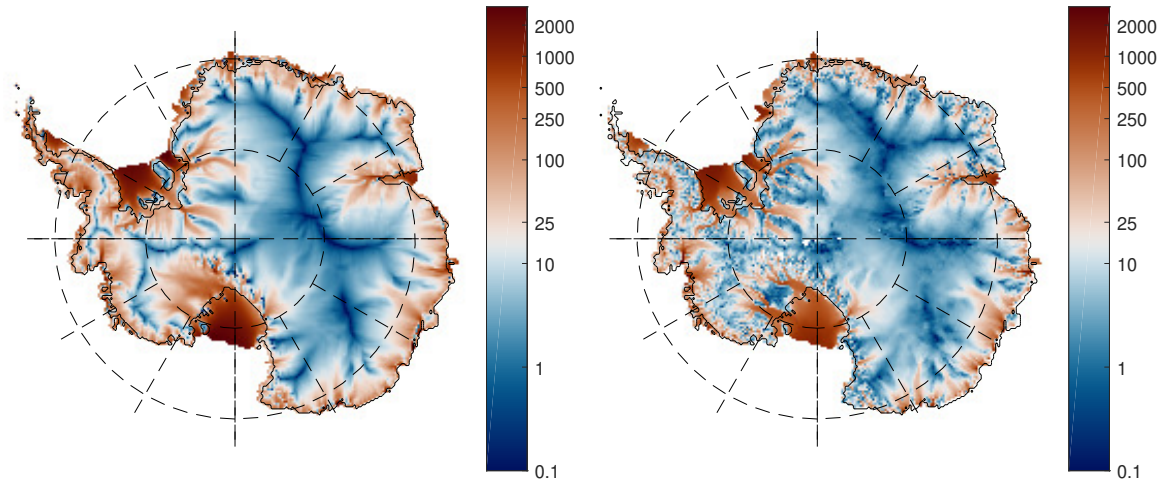


Figure 13: Modelled (left) and observed (right) ice flow velocity after the second inversion `ctr.inverse = 2`.

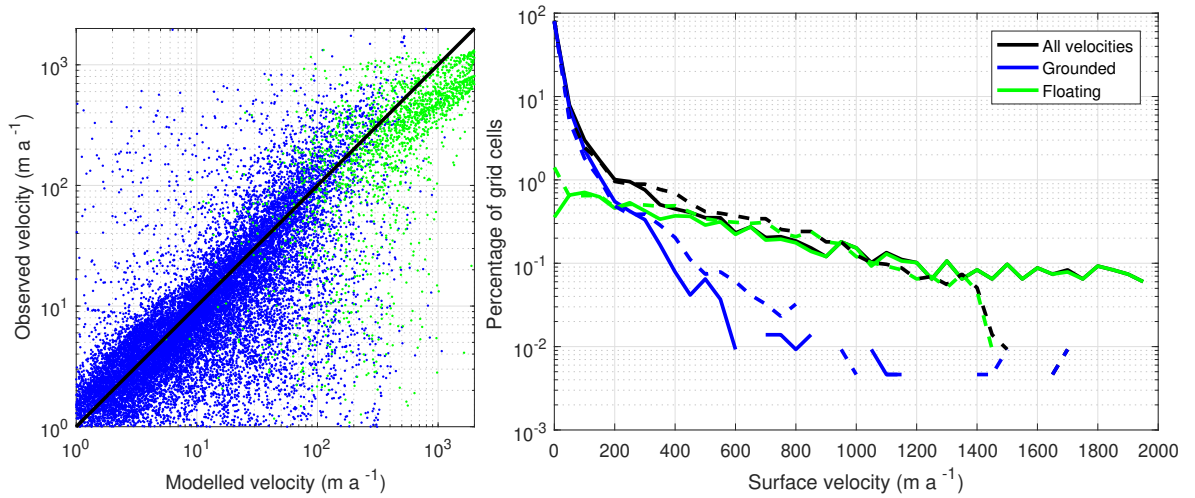


Figure 14: Scattergram of observed versus modelled velocities (left) and binned representation of the observed and modelled velocities.

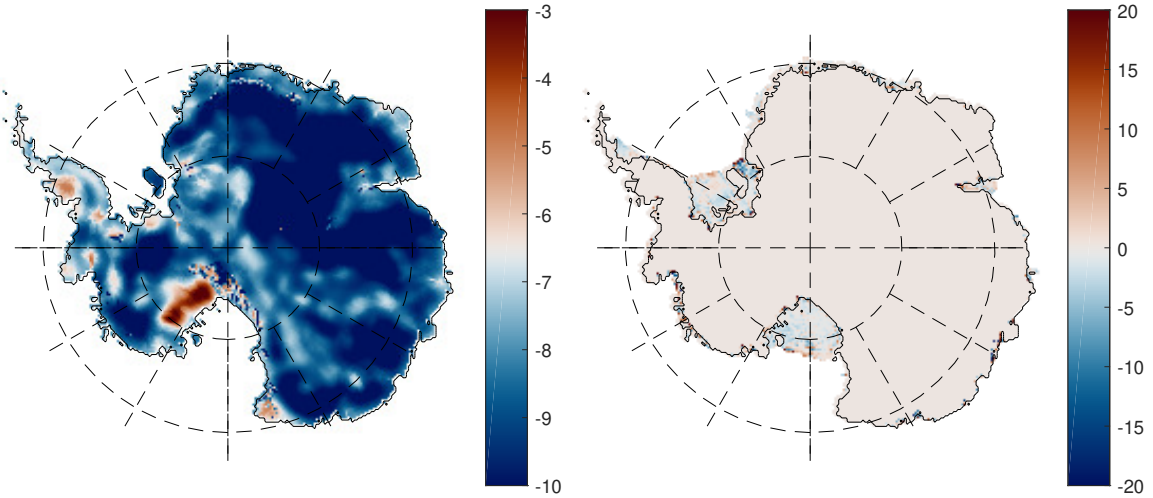


Figure 15: Logarithmic optimized basal sliding coefficients (left) and optimized basal mass balance (m/a) of the ice shelves (right) after the second inversion `ctr.inverse = 2`.

for the simple steady-state solution and the optimized steady-state.

The second optimization phase not only fine-tunes the basal sliding coefficients underneath the grounded ice sheet, but also optimizes the basal melt and accretion rates under the ice shelves in order to keep their ice thickness as close as possible to the observed shelf thickness. Since observed ice velocities are not part of the optimization (the nudging is performed using observed ice thickness), we can use ice velocities as a validation of our model results, as shown in Figures 13 and 14. The resulting basal coefficients and optimized sub-shelf mass balance are displayed in Figure 15.

## 13 Atmospheric forcing

In Kori–ULB, the interactions between the ice sheet and the climate components of the Earth system may be approximated either by one-way coupling of Kori–ULB to a climate model, or by using parameterisations or reduced-order models.

If no other information is provided to the model, Kori–ULB will, by default, consider the atmospheric boundary conditions provided as input in `infile` to be constant in time and space. The climatic mass balance `Mb` enters in Eq. (7), while the near-surface air temperature `Ts` is converted into top-of-the-ice temperature influencing the ice temperature via the thermomechanical coupling (section 7). Modifications of the atmosphere boundary conditions may be imposed either in a simplified way, i.e., using scalar temperature offsets, or by reading files with time- and space-dependent climate data produced by a climate model. The settings controlling the climate forcing of the model are provided by the optional `struct` field `fc` as well as by control parameters in `ctr`.

The atmospheric forcing is applied either by reading air temperature and surface mass balance (defined as precipitation minus evapotranspiration minus runoff) outputs from a climate model or by modifying the present-day fields (typically derived from regional climate model projections) in a parameterized way by applying a spatially-uniform shift in surface temperature and correcting the surface mass balance for such temperature change using a Clausius-Clapeyron-like relation (Garbe et al., 2020; Golledge et al., 2015; Pollard and DeConto, 2012a).

### 13.1 Parameterisations of the near-surface air temperature and the precipitation rate using a scalar temperature offset

When parameterized, any spatially-uniform change in the background (forcing) surface temperature  $\Delta T$  (provided as a `fc.DeltaT` time vector) leads to an overall change in the near-surface air temperature  $T_s = T_s^{\text{obs}} + \Delta T$ .

In addition, if desired (using `ctr.TsFunc`), the near-surface air temperature can be further corrected for ice-sheet elevation changes according to the environmental lapse rate  $\gamma$ . The air temperature field  $T_s$  is hence modified (at every timestep) as follows (Huybrechts et al., 1998; Pollard and DeConto, 2012a)

$$T_s = T_s^{\text{obs}} + \Delta T + \gamma(h_s - h_s^{\text{obs}}), \quad (122)$$

where  $\gamma = -0.0082^\circ\text{C m}^{-1}$  is the lapse rate. The subscript ‘obs’ refers to the present-day observed value.

Similarly, the precipitation field  $P$  can also be modified as a function of the temperature change (using `ctr.MbFunc`), either following Pollard and DeConto (2012a); Garbe et al. (2020)

$$P = P^{\text{obs}} \exp(0.05 \times (\gamma(h_s - h_s^{\text{obs}}) + \Delta T)), \quad (123)$$

or following Golledge et al. (2015), based on an analysis of CMIP5 models (Frieler et al., 2015).

$$P = P^{\text{obs}} \times (1 + 0.053(\gamma(h_s - h_s^{\text{obs}}) + \Delta T)). \quad (124)$$

This leads to a smaller accumulation increase over the interior of ice sheets (and Antarctica in particular) with an increase in (background) temperature.

Surface runoff,  $R_o$ , is calculated using a positive degree-day model that uses the near-surface air temperature and the precipitation rate as inputs (see section 13.3 below). Unless externally provided from climate model outputs, evapotranspiration  $E_v$  is assumed to remain constant.

The surface mass balance  $\dot{a}$  at every model timestep is the sum of the different components, i.e.,  $\dot{a} = P - E_v - R_o$ .

## 13.2 Reading atmospheric boundary conditions from files

Alternatively (i.e., if not parameterized as above), evolving atmospheric boundary conditions can easily be replaced by spatial fields that stem from (global or regional) climate models.

The fields that can be externally provided are the near-surface air temperature ( $T_s$ ), the precipitation rate ( $Pr$ ), the evapotranspiration rate ( $Evp$ ), the runoff rate ( $runoff$ ), and the total climatic surface mass balance ( $Mb$ ). To do so, the `struct` field `fc` is required in order to specify the location of the externally forced fields (`fc.atm_XX_fname`, where XX may be  $T_s$ ,  $Mb$ ,  $Pr$ ,  $Evp$ , and  $runoff$ ) and the frequency of the forcing (see section 13.5).

If the total climatic surface mass balance is provided, the  $Mb$  field is directly used. Alternatively, the surface mass balance components may be provided separately. Therefore, if any of  $runoff$ ,  $Pr$ , and/or  $Evp$  is provided,  $Mb$  is calculated as  $Pr - Evp - runoff$ . If one or several `fc.atm_XX_fname` are defined, the corresponding fields will be read in every `fc.atm_cnt` timestep, and this between times `fc.atm_Tinit` and `fc.atm_Tend` (see section 13.5).

If relevant, fields of atmospheric boundary conditions provided by external climate models may be corrected to account for the difference in ice-sheet elevation between the ice-sheet model and the observational dataset (provided as Ho Pollard and DeConto, 2012a; Garbe et al., 2020), following equations (122) and (123). Similarly, externally-provided surface runoff fields can be corrected for changes in surface elevation with respect to a reference ice sheet geometry using the following correction (inferred from RCM outputs):

$$R_o = R_o^{\text{obs}} + 1.805 \left[ \exp(0.5745 \times T_s) - \exp(0.5745 \times T_s^{\text{obs}}) \right]. \quad (125)$$

## 13.3 Positive Degree Day (PDD)-based melt-and runoff scheme

Surface runoff,  $R_o$ , if not externally provided from a climate model, may be parameterized using a positive degree-day model that calculates the yearly-mean surface melt production and subsequent runoff at the ice surface by capturing the basic physical processes of refreezing versus runoff in the snow column (Huybrechts and de Wolde, 1999), using the near-surface air temperature and the precipitation rate as inputs.

The positive degree-day model is a parameterisation of surface melt where melt is assumed to be proportional to the number of positive degree-days (PDD), defined as the integral of positive Celsius temperature  $T$  over a time interval  $A$ , typically one year.

$$\text{PDD} = \int_0^A \max(T(t), 0) dt. \quad (126)$$

In order to account for diurnal cycles and synoptic ( $\sim$  days) variability of the temperature around the melting point (which significantly affects surface melt on a multi-year scale), it is common to approximate (sub)daily climate means from seasonal means by assuming a normal probability distribution of the near-surface air temperature  $T$  of known standard deviation  $\sigma_{\text{PDD}}$  around the (typically weekly or monthly) seasonal mean temperature  $T_M$ . It follows that, for a year, the number of PDDs can be computed using the following double-integral formulation (Reeh, 1989)

$$\text{PDD} = \frac{1}{\sigma_{\text{PDD}}\sqrt{2\pi}} \int_0^A dt \int_{T_t}^{\infty} T \exp\left(-\frac{(T - T_M(t))^2}{2\sigma_{\text{PDD}}^2}\right) dT, \quad (127)$$

where  $T_t$  is typically  $0^\circ\text{C}$ , though some studies have considered a positive temperature threshold different than  $0^\circ\text{C}$  (e.g., Golledge et al., 2019). The standard deviation  $\sigma_{\text{PDD}}$  is often taken as 4–5°C (Reeh, 1989; Huybrechts and de Wolde, 1999). Here, fixed values of  $\sigma_{\text{PDD}}$  are used.

Most implementations of the PDD method take daily or weekly temperature values from interpolated monthly-mean climatological data. In contrast, if monthly temperature and precipitation variations are not known (for example if these fields are parameterised as in section 13.1), it is common to approximate the intra-annual variations of the air temperature by adding a sinusoidal seasonal cycle to the yearly mean air temperature (e.g., Pollard and DeConto, 2012a). In Kori–ULB, two distinct situations are allowed in order to define the intra-annual variations of the air temperature and precipitation rates.

1. The evolution of the monthly-mean (or sub-monthly) air temperatures and precipitation rates are externally provided (following section 13.2): they are directly used as inputs to define the seasonal cycles of temperature and precipitation  $T_M$  and  $P_M$  (`ctr.monthly=1` must be defined).
2. The intra-annual variations of the air temperatures and precipitation rates are not known:  $T_M$  and  $P_M$  are approximated based on the yearly-mean air temperature  $T_s$  and precipitation rate  $P$ . To do so, a sinusoidal seasonal cycle is added to  $T_s$ , using a peak-to-peak air amplitude  $T_a$  based on the ice elevation (and optionally the latitude). The precipitation rate is considered constant in time throughout the annual cycle, i.e.  $P_M = P$ .

A semi-analytical solution to the above temperature integral (here adapted to account for the more general case with a positive temperature threshold  $T_t$ ) has been proposed by Calov and Greve (2005):

$$\text{PDD} = \int_0^A dt \left[ \frac{\sigma_{\text{PDD}}}{\sqrt{2\pi}} \exp\left(-\frac{(T_t - T_M(t))^2}{2\sigma_{\text{PDD}}^2}\right) + \frac{(T_M(t) - T_t)}{2} \operatorname{erfc}\left(\frac{T_t - T_M(t)}{\sqrt{2}\sigma_{\text{PDD}}}\right) + T_t \right], \quad (128)$$

where  $\operatorname{erfc}(x)$  is the complementary error function.

Degree-day factors represent the amount of melt that occurs per positive degree-day, expressed as millimetres water-equivalent or ice-equivalent per degree per day. These melt factors differ on a specific glacier for snow and ice (as ice is less reflective than snow, it

melts more per positive degree-day). A simple degree-day model assumes that, for a specific glacier,

$$M = K_{\text{snow}} \text{PDD} + K_{\text{ice}} (\text{PDD} - M_{\text{snow}} / K_{\text{snow}}), \quad (129)$$

where  $K_{\text{ice}}$  and  $K_{\text{snow}}$  are the degree-day factors for ice and snow respectively. The surface melt of a given time period is considered in two phases: any surface layer of snow must be melted ( $M_{\text{snow}}$ ), before the subjacent ice is melted with the remaining PDD that is not used up by snow melt (see Figure 16).

In order to approximate the amount of snow available for surface melting, the solid (snow) and liquid (rain) fractions (SF and RF, respectively) of the total precipitation  $P$  (provided as input) needs to be determined. This is done by determining a ‘rain fraction’ factor  $R$ , with  $\text{RF} = P \times R$  and  $\text{SF} = P \times (1 - R)$ . More specifically, the rain fraction  $R$  is computed as a function of the daily temperature  $T_D$ , with a statistic that is normally distributed and centered on the curve of the mean seasonal cycle  $T_M$  with a standard deviation  $\sigma_{RS}$  of  $3.5^\circ\text{C}$ , accounting for random temperature fluctuations and the daily cycle:

$$R_f = 1 - \max \left[ 0, \min \left( \frac{T_{\text{rain}} - T_D}{T_{\text{rain}} - T_{\text{snow}}}, 1 \right) \right], \quad (130)$$

where  $T_D$  is the semi-analytical solution of the temperature integral (Calov and Greve, 2005) above the  $T_{\text{snow}}$  threshold, used in order to take into account the daily variability of the temperature. All precipitation during periods with daily air temperatures above  $T_{\text{rain}} = 2^\circ\text{C}$  is interpreted as rain; all precipitation during periods with air temperatures below  $T_{\text{snow}} = 0^\circ\text{C}$  is interpreted as snow.

The retention of melt water before runoff takes place is mainly a consequence of refreezing of percolating melt water through new or old snow layers, and of capillary forces in the upper snow layers that retain the melt water until the end of the melting season. The latter water refreezes during the winter and produces an impermeable layer in the water-saturated zone, called superimposed ice (Janssens and Huybrechts, 2000; Huybrechts and de Wolde, 1999; Reijmer et al., 2012). Here, these processes are (roughly) approximated using a simple snow pack model. Due to the lack of more sophisticated firn model, the surface of the previous year is considered impermeable. The remaining rain and snow melt liquid water (beyond the snowpack saturation) as well as the entire ice melt water is thus converted into surface run-off, meaning that in the absence of a water-routing hydrologic scheme, all surface water that could potentially form melt ponds is considered to be run-off, i.e. is lost by the ice sheet.

The amount of refreezing is limited by the available energy and the available amount of liquid fraction (from snow melt and rain) of the annual precipitation (Reijmer et al., 2012). Following Janssens and Huybrechts (2000) and Reijmer et al. (2012), we define  $P_{\text{ref}}$  as the potential retention mass, which is the maximum amount of water that can be refrozen,  $W_{\text{ref}}$  as the available water mass, and  $E_{\text{ref}}$  as the effective retention mass, which is the actual mass refrozen in the snow.  $P_{\text{ref}}$ ,  $W_{\text{ref}}$  and  $E_{\text{ref}}$  are related by

$$E_{\text{ref}} = \min(P_{\text{ref}}, W_{\text{ref}}) \quad (131)$$

While some formulations simply assume runoff to occur when the amount of refreezing exceeds a maximum fraction ( $P_{\text{max}}$ ) of the annual snowfall (Reeh, 1991), here we use a more physically-based approach (based on a simple thermodynamic parameterisation of the refreezing process) proposed by Huybrechts and de Wolde (1999), where the condition for refreezing is given by:

$$P_{\text{ref}} = \frac{c_i}{L_f} d_{\text{SUP}} (T_m - T_{\text{year}}), \quad (132)$$

where  $c_i$  and  $L_f$  are the specific heat capacity and latent heat of fusion of ice, respectively,  $T_{\text{year}}$  is the annual mean temperature,  $T_m$  is the melting point,  $d_{\text{SUP}}$  is the thickness of the thermally active layer. The capillary suction effect of the snowpack is therefore not accounted for in the expression of  $P_{\text{ref}}$ . Huybrechts and de Wolde (1999) determined a value of  $d_{\text{SUP}} = 2$  m based on observations at the equilibrium line in central west Greenland, while Wright et al. (2007) obtained the best agreement with observations from a glacier on Svalbard for  $d_{\text{SUP}} = 5$  m. According to equation (132), the maximum amount of superimposed ice is equivalent to the latent heat released by the refreezing melt water to raise the temperature of the uppermost  $d_{\text{SUP}}$  m of the ice sheet surface from the mean annual temperature to the melting point. Therefore, for part of the melt water to run off, the amount must be large enough to remove the cold content of the snow and raise its temperature to 0°C.

Finally, since refreezing can only occur in snow or firn and given that we lack a sophisticated multilayered snow-firn model here, we limit the effective refreezing  $E_{\text{ref}}$  to the total annual precipitation  $P$  (following Janssens and Huybrechts, 2000; Reijmer et al., 2012).

Overall, the PDD-based melt-and-runoff algorithm implemented in Kori–ULB (outlined in Figure 16) calculates the yearly surface mass balance at the ice surface by capturing the basic physical processes of surface melting of ice and snow and refreezing versus runoff in the snow pack (Huybrechts and de Wolde, 1999). The algorithm involves seasonal cycles of zero-dimensional bulk quantities of snow and embedded melt water, run through several years to equilibrium with a weekly time step, driven by seasonal variations of the air temperatures and precipitation rate interpolated in time to those time steps. A PDD scheme calculates the melt of snow or exposed ice at each weekly timestep (with a uniform normal distribution representing diurnal cycles and synoptic variability) while tracking the evolving thickness of the snow layer across the balance year. Accumulation is assumed equal to precipitation when the daily temperature (also assumed to have a normal distribution around the monthly mean) is below  $T_{\text{snow}}$ , and decreasing linearly with temperature between  $T_{\text{snow}}$  and  $T_{\text{rain}}$  while also accounting for temperature variability around the seasonal mean. After seasonal equilibrium is reached, net annual quantities are used to calculate the refreezing of the produced melt water (which depends on the cold content of the upper ice sheet layers; Huybrechts and de Wolde, 1999), and runoff of excess melt water once the snow is saturated.

Finally, the surface mass balance is then the sum of the different components, i.e.,  $\dot{a} = P - E_v - R_o$ .

### 13.4 Control parameters for atmosphere forcing

**ctr.MbConst** = Value of a constant surface mass balance applied over the whole model domain ( $\text{m a}^{-1}$  ice equivalent). Default = 0;

**ctr.TsConst** = Value of a constant surface temperature applied over the whole model domain (°C). Default = 0;

**ctr.MbType** : Type of surface mass balance distribution/perturbation.

**0:** No corrections of the provided (initial) surface mass balance components.

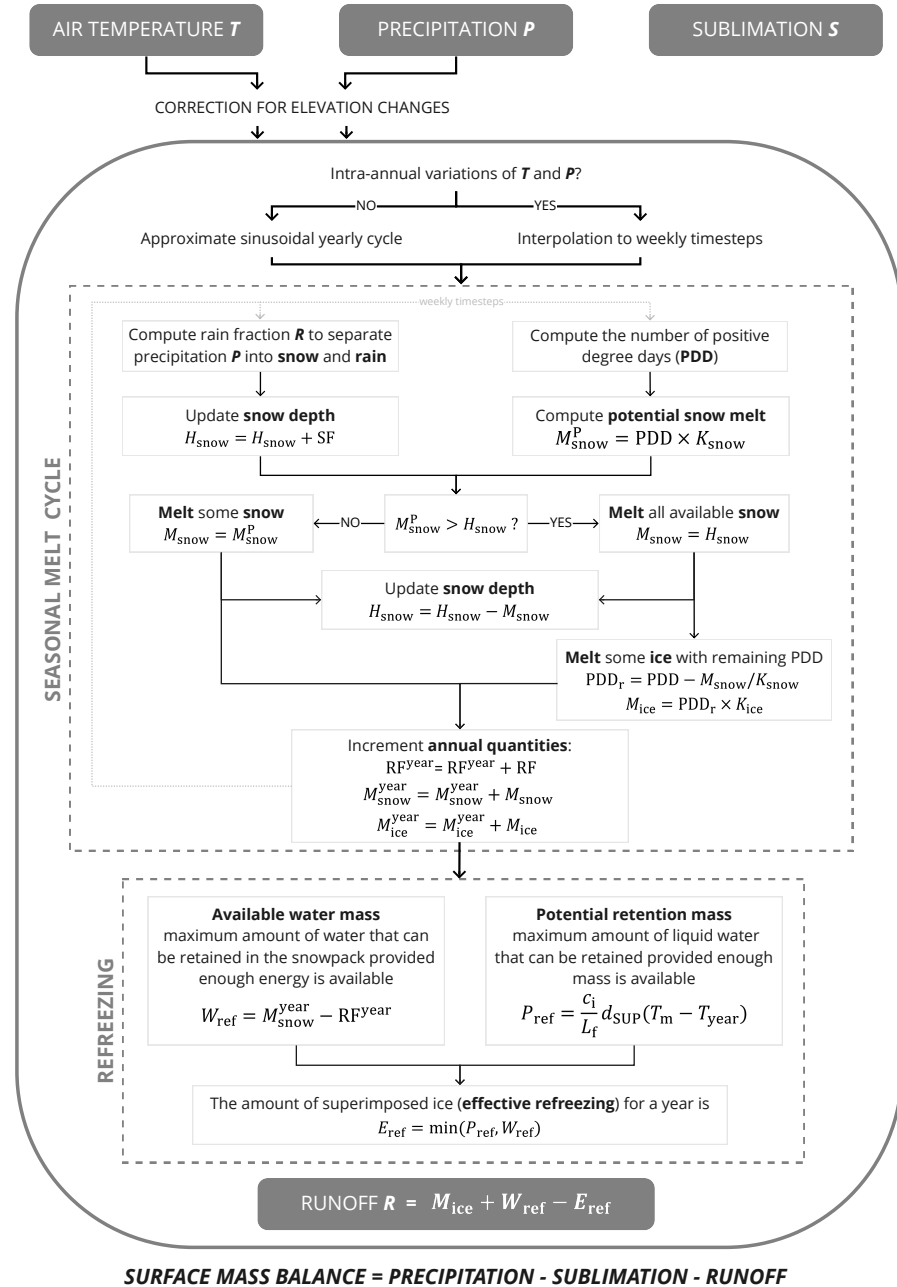


**Figure 16: Positive degree-day-based melt-and-runoff model implemented in Kori-ULB.** In the seasonal melt cycle (typically applied with weekly timesteps),  $H_{\text{snow}}$  is the evolving snow depth,  $M_{\text{snow}}^P$  and  $M_{\text{snow}}$  are the weekly potential and effective snow melt, respectively,  $M_{\text{ice}}$  is the weekly ice melt, and  $RF$  and  $SF$  are the weekly rainfall and snowfall, respectively.  $M_{\text{snow}}^{\text{year}}$ ,  $M_{\text{ice}}^{\text{year}}$  and  $RF_{\text{year}}$  are the annual quantities of snow melt, ice melt, and rainfall, respectively. Note that due to the lack of firn model, the snow depth is set to zero at the beginning of every year.

- 1:** Correction for elevation changes according to Pollard and DeConto (2012a); Garbe et al. (2020):  $P = P(0) \exp(0.05 \times (T_s - T_s(0)))$ .
- 2:** Correction for elevation changes according to Golledge et al. (2015):  $P = P(0)[1 + 0.053(T_s - T_s(0))]$
- 3:** EISMINT fixed margin experiment with  $M_b = M_b(0) + 0.02\Delta T$
- 4:** EISMINT moving margin experiment
- 5:** EISMINT moving margin experiment with  $R_{el} = R_{el} + 10\Delta T$
- 6:** Alpine glacier with linear mass balance as a function of the equilibrium line altitude:  $Pr = ctr.mbgrad * (sn - ctr.ELA)$ . It is possible to identify a second mass balance gradient (`ctr.mbgrad1`) for the region above the ELA.

**ctr.mbgrad** = Surface mass balance gradient over glaciers.

**ctr.mbgrad1** = Surface mass balance gradient over glaciers for the region above the ELA separately (accumulation area).

**ctr.ELA** = Equilibrium line altitude (ELA; m a.s.l.)

**ctr.TsType** = type of surface temperature distribution/perturbation.

- 0:** No corrections for elevation changes. Initial  $T_s$  remain unchanged:  $T_s = T_s(0)$
- 1:** Correction for elevation changes using atmospheric lapse rate `par.Tlapse`.
- 2:** EISMINT moving margin experiment.
- 3:** Any other user specified function for surface temperature.

**ctr.PDDcalc** = Application of a PDD-based melt-and runoff scheme.

- 1** : Runoff calculated from a PDD-based melt-and-runoff scheme ;
- 0** : Runoff not calculated from a PDD-based melt-and-runoff scheme (default).

**ctr.monthly** = Definition of intra-annual temperature and precipitation variations to be used in the PDD-based scheme.

- 1** : Intra-annual (monthly or submonthly) variations of the air temperature and precipitation rates provided by input atmospheric data are be provided to be used in the PDD scheme.;
- 0** : Intra-annual (monthly or submonthly) variations of the air temperature and precipitation rates (default). They will be approximated using a sinusoidal cycle for the air temperature, and considering the precipitation constant throughout the annual cycle. If `ctr.monthly = 1`, `fc.atm_Ts_fname`, `fc.atm_Pr_fname`, and `fc.atm_yrstep` must be defined (see below).

**ctr.runoffcorr** = Correction of externally-provided surface runoff fields can be corrected for changes in surface elevation

- 1** : No correction for elevation changes. Provided `runoff` field remains unchanged.
- 0** : Runoff corrected for ice-sheet elevation changes using  $R_o = R_o^{\text{obs}} + 1.805[\exp(0.5745 \times T_s) - \exp(0.5745 \times T_s^{\text{obs}})]$ .

### 13.5 Forcing parameters for atmosphere forcing

**fc.DeltaT** : Scalar time-dependent air temperature offset. Time vector of dimension (ctr.nsteps, 1). If not defined, fc.DeltaT is considered to be zero.

**fc.atm\_Mb\_fname** : Path directory and name of the 2-D sequential Mb input files (optional). The files must be named sequentially (starting from 000 and ending by fc.atm\_snapshots-1 – for example if 10 files are provided, the first file is named fc.atm\_Mb\_fname000 and the last file is named fc.atm\_Mb\_fname009). The 2D field provided in each sequential fc.atm\_Mb\_fname file must be named Mb. Note that if fc.atm\_Mb\_fname is defined, any fc.atm\_Pr\_fname, fc.atm\_Evp\_fname or fc.atm\_runoff\_fname will not be read in.

**fc.atm\_Ts\_fname** : Path directory and name of the 2-D sequential Ts input files (optional). The files must be named sequentially (starting from 000 and ending by fc.atm\_snapshots-1. The 2D field provided in each sequential fc.atm\_Ts\_fname file must be named Ts.

**fc.atm\_Pr\_fname** : Path directory and name of the 2-D sequential Pr input files (optional). The files must be named sequentially (starting from 000 and ending by fc.atm\_snapshots-1. The 2D field provided in each sequential fc.atm\_Pr\_fname file must be named Pr.

**fc.atm\_Evp\_fname** : Path directory and name of the 2-D sequential Evp input files (optional). The files must be named sequentially (starting from 000 and ending by fc.atm\_snapshots-1. The 2D field provided in each sequential fc.atm\_Evp\_fname file must be named Evp.

**fc.atm\_runoff\_fname** : Path directory and name of the 2-D sequential runoff input files (optional). The files must be named sequentially (starting from 000 and ending by fc.atm\_snapshots-1. The 2D field provided in each sequential fc.atm\_runoff\_fname file must be named runoff. Note that fc.atm\_runoff\_fname will not be read if ctr.Pddcalc=1.

**fc.atm\_snapshots** : Total amount of provided atmospheric boundary conditions snapshots. Must be defined if any of the fc.atm\_XX\_fname above is defined.

**fc.atm\_Tinit** : Year of the first sequential input file. Must be defined if any of the fc.atm\_XX\_fname above is defined.

**fc.atm\_Tend** : Year of the last sequential input file. Must be defined if any of the fc.atm\_XX\_fname above is defined. If fc.atm\_snapshots=1, then fc.atm\_Tinit = fc.atm\_Tend.

**fc.atm\_cnt** : Timesteps interval of the sequential input files, i.e., the atmospheric inputs will be called every fc.atm\_cnt model timesteps. Must be defined if any of the fc.atm\_XX\_fname above is defined.

**fc.atm\_nrep** : Number of last atmospheric snapshots to repeat if time > fc.atm\_Tend. For example, if fc.atm\_nrep=1, the last fc.atm\_XX\_fname file will be re-read every

**fc.atm\_cnt** timestep if model time exceeds **fc.atm\_Tend**. Must be defined if any of the **fc.atm\_XX\_fname** above is defined and if there is the possibility that model time exceeds **fc.atm\_Tend**.

**fc.atm\_yrstep** : Number of files per year. Necessary if to extract annual cycles from input atmospheric data if **fc.monthly=1**.

Below is an example script on how to provide monthly externally-forced atmospheric boundary conditions. In this case, monthly near-surface air temperature, evapotranspiration and precipitation data are provided while runoff is to be calculated by a PDD-based melt-and-runoff scheme (section 13.3).

```
% READING MONTHLY EXTERNAL ATMOSPHERIC BOUNDARY CONDITIONS
% AS ATMOSPHERIC FORCING

% example of path directory where forcing files are located
folder_name=['/home/username/Documents/AtmosphericForcingFiles/'];
% files name providing ocean Ts inputs
fc.ocn_Ts_fname=[folder_name 'TS'];
% files name providing ocean Pr inputs
fc.ocn_Pr_fname=[folder_name 'PR'];
% files name providing ocean Evp inputs
fc.ocn_Evp_fname=[folder_name 'EVP'];
% Total amount of snapshots
fc.ocn_snapshots=1032;
% Ocean snapshots called every ocean_cnt timesteps -- here: every month
fc.ocn_cnt=1/ctr.dt;
% Time of first snapshot
fc.ocn_Tinit=2015;
% Time of last snapshot
fc.ocn_Tend=2100+11/12;
% Number of last snapshots to repeat if T>Tend -- here: last snapshot
fc.ocn_nrep=12;

% runoff to be calculated by a PDD model using the monthly data as input
ctr.PDDcalc=1;
ctr.monthly=1;
fc.atm_yrstep=12; % snapshots per year
```

## 13.6 Global parameters for atmosphere forcing

**par.PDDth** = 0: PDD threshold temperature ( $0^{\circ}$  C).

**par.Train** = 2.

**par.Tsnow** = 0.

**par.snowfac** = 3/par.rho: PDD factor for melting snow (w.e. mm/PDD)

**par.icefac** = 8/par.rho: PDD factor for melting ice (w.e. mm/PDD)

**par.d\_ice** = 5: Maximum depth of refreezing of percolating meltwater (m).

**par.Tlapse = -0.008:** Atmospheric lapse rate.

**par.Tsigma = 4:** Standard deviation of mean temperature correction with height.

**par.Psigma = 3.5:** Standard deviation of mean temperature for rain factor calculation.

**par.PDDsteps = 48:** number of integration steps (minimum 12 = 1 month)

## 14 Ocean forcing

In Kori–ULB, the interactions between the ice sheet and the climate components of the Earth system may be approximated either by one-way coupling of Kori–ULB to a climate model, or by using parameterisations or reduced-order models.

If no other information is provided to the model, Kori–ULB will, by default, consider the atmospheric and oceanic boundary conditions provided as input in `infile` to be constant in time and space. The ocean temperature  $T_o$  and salinity  $S_o$  are used to produce a sub-shelf mass flux (i.e., sub-shelf melt rates) also used in the mass-continuity equation (Eq. (7)). Similar to the atmosphere, the oceanic forcing is applied either by reading ocean temperature and salinity outputs from a climate model or by modifying the present-day observed fields in a parameterized way by relating changes in ocean temperature to changes in the background atmospheric temperature (section 14.2). Similarly, a sea-level forcing may be imposed using a spatially-uniform sea-level offset (section 14.4).

### 14.1 Sub-shelf melting

In Kori–ULB, melting underneath the floating ice shelves may be determined by different sub-shelf melt parameterisation schemes, such as the PICO model (Reese et al., 2018a), the Plume model (Lazeroms et al., 2019), and simple parameterisations (Jourdain et al., 2019; Favier et al., 2019). The applied sub-shelf melt scheme is defined by `ctr.meltfunc`.

#### 14.1.1 Simple parameterizations

Melting underneath the floating ice shelves is often based on parametrizations that relate sub-shelf melting to ocean temperature and ice-shelf depth (Beckmann and Goosse, 2003; Holland et al., 2008), either in a linear or a quadratic way (Martin et al., 2011; Pollard and DeConto, 2012a; de Boer et al., 2015; DeConto and Pollard, 2016). This leads to higher melt rates close to the grounding line, as the ice-shelf bottom is the lowest, i.e.,

$$M = \gamma_T \frac{\rho_s c_{po}}{L \rho_i} |T_{oc} - T_{fo}| (T_{oc} - T_{fo}), \quad (133)$$

and where  $M$  is the sub-ice-shelf basal melt rate,  $c_{po}$  is the specific heat capacity of the ocean,  $\gamma_T$  is the thermal exchange velocity,  $L$  is the latent heat of fusion,  $T_{oc}$  is the temperature of the ocean underneath the ice shelf, and  $T_{fo}$  is the freezing temperature defined by Beckmann and Goosse (2003) as:

$$T_{fo} = \lambda_1 S_o + \lambda_2 + \lambda_3 h_b, \quad (134)$$

where  $S_o$  is a value for the salinity of the ocean waters. We employ measurements of ocean temperature and salinity defined for each drainage basin of the Antarctic ice sheet based on Schmidtko et al. (2014) (see below for more details).

Alternatively, a linear version of Eq. (133) can be employed, which will also require a different value for  $\gamma_T$ . The latter is in general used as a general tuning parameter for the melt function (Favier et al., 2019).

### 14.1.2 Non-local melt-rate parametrization (ISMIP6)

Climate model projections have previously been used to compute ice-shelf basal melt rates in ice-sheet models, but the strategies employed –e.g. ocean input, parametrization, calibration technique, and corrections– have varied widely and are often ad-hoc. Jourdain et al. (2019) propose a methodology for the calculation of circum-Antarctic basal melt rates for floating ice, based on climate models, that is suitable for ISMIP6, the Ice Sheet Model Intercomparison Project for CMIP6 (6th Coupled Model Intercomparison Project). The past and future evolution of ocean temperature and salinity is derived from a climate model by estimating anomalies with respect to the modern day, which are added to an present-day climatology constructed from existing observational datasets. Temperature and salinity are extrapolated to any position potentially occupied by a simulated ice shelf. A simple formulation is proposed for a basal-melt parametrization in ISMIP6, constrained by the observed temperature climatology, with a quadratic dependency on either the non-local or local thermal forcing. Two calibration methods are proposed: (i) based on the mean Antarctic melt rate (MeanAnt) and (ii) based on melt rates near Pine Island’s deep grounding line (PIGL).

Melt rates in the common ISMIP6 experiments are derived using a slightly modified version of the non-local quadratic parametrization proposed by Favier et al. (2019). The parametrization is explicitly defined over regional sectors, rather than for a single ice shelf, and it includes a temperature correction:

$$m(x, y) = \gamma_0 \times \left( \frac{\rho_{sw} c_{pw}}{\rho_i L_f} \right)^2 \times (TF(x, y, z_{\text{draft}}) + \delta T_{\text{sector}}) \times |\langle TF \rangle_{\text{draft} \in \text{sector}} + \delta T_{\text{sector}}| \quad (135)$$

where  $TF(x, y, z_{\text{draft}})$  is the thermal forcing at the ice-ocean interface, and  $\langle TF \rangle_{\text{draft} \in \text{sector}}$  the thermal forcing averaged over all the ice-shelves of an entire sector. The uniform coefficient  $\gamma_0$ , with units of velocity, is somewhat similar to the exchange velocity commonly used to calculate ice-ocean heat fluxes. The temperature correction  $T_{\text{sector}}$  for each sector is needed to reproduce observation-based melt rates (at the scale of a sector) from observation-based thermal forcing.

### 14.1.3 The PICO ocean-coupler model

Alternatively to the sub-shelf melt parametrization, an ocean-coupling model has been implemented based on PICO (Potsdam Ice-shelf Cavity mOdel; Reese et al. (2018a)). PICO is developed from the ocean box model of Olbers and Hellmer (2010), which is designed to capture the basic overturning circulation in ice shelf cavities which is driven by the “ice pump” mechanism: melting at the ice shelf base near the grounding line reduces salinity and the ambient ocean water becomes buoyant, rising along the ice shelf base towards the calving front. Since the ocean temperatures on the Antarctic continental shelf are generally close to the local freezing point, density variations are primarily controlled by salinity changes. Melting at the ice-shelf base hence reduces the density of ambient water masses, resulting in a haline-driven circulation. Buoyant water rising along the shelf base draws in ocean water at depth, which flows across the continental shelf towards the deep grounding lines of the ice shelves. The warmer these water masses are, the stronger is the melting-induced ice pump. The Olbers and Hellmer (2010) box model describes the relevant physical processes and captures this vertical overturning circulation by defining consecutive boxes following the flow

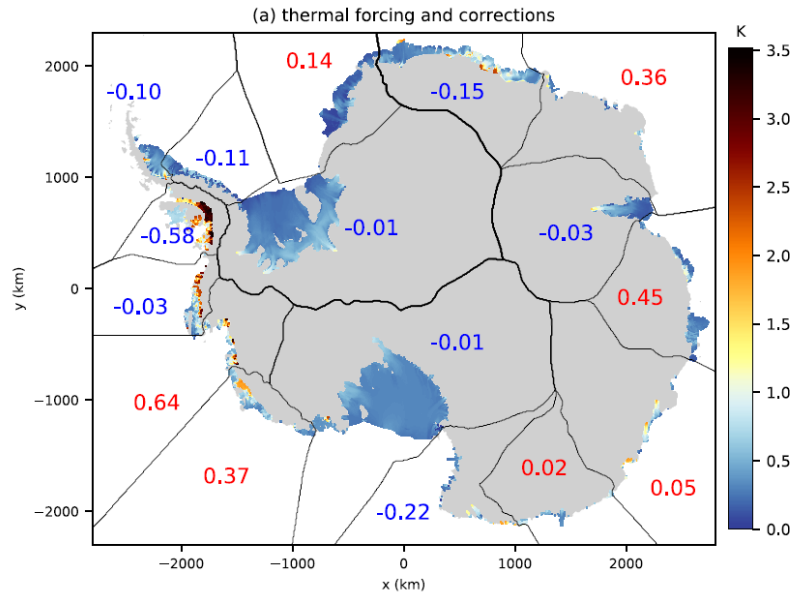


Figure 17: Thermal forcing (shaded) and its corrections (blue/red numbers indicating negative/positive  $\delta T$ ) applied to each sector for non-local-MeanAnt with a slope dependency (Figure from Jourdain et al., 2019).

within the ice shelf cavity.

The strength of the overturning flux  $q$  is determined from the density difference between the incoming water masses on the continental shelf and the buoyant water masses near the deep grounding lines of the ice shelf. As PICO is implemented in an ice sheet model with characteristic time scales much slower than typical response times of the ocean, we assume steady-state ocean conditions and hence reduce the complexity of the governing equations of the Olbers and Hellmer (2010) model. We assume stable vertical stratification, which motivates neglecting the diffusive heat and salt transport between boxes. Without diffusive transport between the boxes, some of the original ocean boxes from Olbers and Hellmer (2010) become passive and can be incorporated into the governing equations of the set of boxes used in PICO. We explicitly model a single open ocean box which provides the boundary conditions for the boxes adjacent to the ice shelf base following the overturning circulation, as shown in Fig. 18. In order to better resolve the complex melt patterns, PICO adapts the number of boxes based on the evolving geometry of the ice shelf. These simplifying assumptions allow us to analytically solve the system of governing equations (Reese et al., 2018a).

In general, PICO solves for the transport of heat and salt between boxes in contact with the base of the ice shelf, starting at the grounding line and ending at the ice front (boxes  $B_k$  for  $k = \{1, \dots, n\}$ , where  $n$  is typically less than or equal to 5). After simplification and assuming steady-state conditions, the balance of heat and salt in all boxes along the base of the ice shelf can be written as

$$\begin{aligned} q(T_{k-1} - T_k) - A_k m_k \frac{\rho_i}{\rho_s} \frac{L}{c_{po}} &= 0 \\ q(S_{k-1} - S_k) - A_k m_k S_k &= 0 \end{aligned} \quad (136)$$

Using a simplified formulation of the three-equation melt model by Holland and Jenkins (1999), the transport equations can be solved for salinity  $S_k$  and temperature  $T_k$  in box  $B_k$

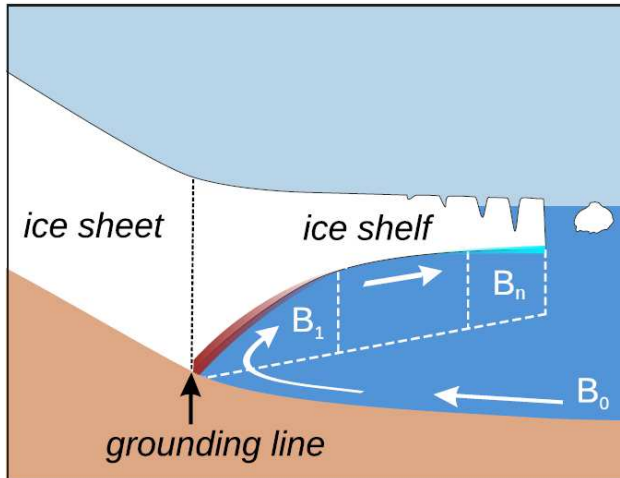


Figure 18: Schematic view of the PICO model. The model mimics the overturning circulation in ice shelf cavities: Ocean water from box  $B_0$  enters the ice shelf cavity at the depth of the sea floor and is advected to the grounding line box  $B_1$ . Freshwater influx from melting at the ice shelf base makes the water buoyant, causing it to rise. The cavity is divided into  $n$  boxes along the ice shelf base. Generally, the highest melt rates can be found near the grounding line, with lower melt rates or refreezing towards the calving front (Reese et al., 2018a).

and are dependent on the local pressure, the box area  $A_k$ , and the temperature  $T_{k-1}$  and salinity  $S_{k-1}$  of the upstream box  $B - k - 1$ . The strength of the overturning circulation,  $q$ , is calculated once per time step in box  $B_1$  from the density difference between the far-field and grounding line water masses:

$$q = C (\rho_0 - \rho_1) \quad (137)$$

The sub-shelf melt rate in each of the boxes is then determined as

$$m_k(x, y) = -\gamma_T \frac{\rho_s c_{po}}{L \rho_i} (\lambda_1 S_k(x, y) + \lambda_2 + \lambda_3 h_b(x, y) - T_k(x, y)) \quad (138)$$

where the subscript  $k$  refers to the values determined for each box within each ice shelf. Input data for the PICO model are present-day observed ocean temperature and salinity at depth on the continental shelf in front of contemporary ice shelves (Schmidtko et al., 2014). For the ice sheet to 'feel' these data, the ice sheet is divided up in different drainage basins based on the limits provided by NASA (Zwally, H. Jay, Mario B. Giovinetto, Matthew A. Beckley, and Jack L. Saba, 2012, [Antarctic and Greenland Drainage Systems](#), GSFC Cryospheric Sciences Laboratory). Mean values of ocean temperature and salinity in front of the ice shelves are then assigned to each basin, so that with retreat of the grounding line, individual ice shelves remain connected to the far-field ocean. These datasets are not calculated within f.ETISH, but should be provided. The PICO model automatically identifies individual ice shelves, divides them up in boxes and calculates ocean properties for each box. Sub-shelf melt rates within each box are determined using the local pressure of the overlying ice (Reese et al., 2018a).

#### 14.1.4 PICOP and plume model

The plume model is a basal melt rate parametrization based on the theory of buoyant melt-water plumes that travel upward along the base of the ice shelf from the grounding line to the location where the plume loses buoyancy. The two-dimensional formulation from Lazeroms et al. (2018) is adapted from the one-dimensional plume model developed by Jenkins (1991) for a plume travelling in direction  $X$  in an ocean with ambient temperature  $T_a$  and salinity  $S_a$ , either provided by PICO (which leads to the PICOP model) or from far-field ocean measurements (which is equivalent to the plume model). The method due to Pelle et al. (2019) has been employed. We begin by defining the grounding line depth,  $z_{gl}$ , over the entire ice shelf, as it is necessary to determine where individual plumes originate in order to employ this parametrization. As a first approximation, we solve an advection equation:

$$\begin{cases} v \cdot \nabla z_{gl} + \epsilon \Delta z_{gl} = 0 & \text{in } \Omega \\ z_{gl} = z_{gl0} & \text{on } \Gamma \end{cases} \quad (139)$$

where  $z_{gl0}$  is the grounding line height defined at the grounding line  $\Gamma$ ,  $\Omega$  is the ice shelf, and as a first approximation,  $v$  is the modelled, depth-averaged ice velocity. Note that  $\epsilon$  is a small diffusion coefficient introduced to minimize noise and to provide numerical stability.

Once  $z_{gl}$  is defined, we continue by computing both the characteristic freezing point  $T_{f,gl}$  and the effective heat exchange coefficient  $\Gamma_{TS}$  as follows:

$$T_{f,gl} = \lambda_1 S_a + \lambda_2 + \lambda_3 z_{gl} \quad (140)$$

$$\Gamma_{TS} = \Gamma_T \left( \gamma_1 + \gamma_2 \frac{T_a - T_{f,gl}}{\lambda_3} \times \frac{E_0 \sin \alpha}{C_d^{1/2} \Gamma_{TS_0} + E_0 \sin \alpha} \right) \quad (141)$$

A geometric scaling factor  $g(\alpha)$  and length scale  $l$  are defined in order to give the plume model the proper geometry dependence and scaling according to the distance travelled along the plume path. The scaling factor and length scale are computed as follows:

$$g(\alpha) = \left( \frac{\sin \alpha}{C_d + E_0 \sin \alpha} \right)^{1/2} \left( \frac{C_d^{1/2} \Gamma_{TS}}{C_d^{1/2} \Gamma_{TS} + E_0 \sin \alpha} \right)^{1/2} \left( \frac{E_0 \sin \alpha}{C_d^{1/2} \Gamma_{TS} + E_0 \sin \alpha} \right) \quad (142)$$

$$\mu = \frac{T_a - T_{f,gl}}{\lambda_3} \times \frac{x_0 C_d^{1/2} \Gamma_{TS} + E_0 \sin \alpha}{x_0 (C_d^{1/2} \Gamma_{TS} + E_0 \sin \alpha)} \quad (143)$$

The dimensionless scale factor  $x_0$  used in the second term of  $l$  defines the transition point between melting and refreezing and is constant for all model results. For a complete explanation of the individual terms that make up these two factors, see Sect. 2.2 of Lazeroms et al. (2018). The length scale is then used in the computation of the dimensionless coordinate,  $\hat{X}$ :

$$\hat{X} = \frac{z_b - z_{gl}}{l} \quad (144)$$

In order to ensure valid values of  $\hat{X}$ , we set a lower bound for the ambient ocean temperature:  $T_a \geq \lambda_1 S_a + \lambda_2$ . The melt rate  $\dot{m}$  is then calculated as

$$\dot{m} = \hat{M}(\hat{X}) \times M \quad (145)$$

where  $\hat{M}(\hat{X})$  is a dimensionless melt curve defined in Lazeroms et al. (2018) and  $M$  is defined as

$$M = M_0 \times g(\alpha) \times (T_a - T_f(S_a, z_{gl}))^2 \quad (146)$$

## 14.2 Scalar ocean temperature offset

When imposing a spatially-uniform shift in near-surface air temperature using a `fc.DeltaT` time-vector, the ocean temperature may be modified accordingly by a temperature offsets related to `fc.DeltaT` through a factor `ctr.meltfactor`, i.e.,

$$T_o = T_o^{\text{obs}} + F_M \times \Delta T \quad (147)$$

where  $F_M$  is an ocean melt factor that represents the ratio between oceanic and atmospheric temperature changes (Maris et al., 2014; Golledge et al., 2015) and  $\Delta T$  is a spatially-uniform shift in background atmospheric temperatures. Equation (147) with  $F_M = 0.25$  has been shown to reproduce trends in ocean temperatures following an analysis of the Climate Model Intercomparison Project phase 5 (CMIP5) data set for changes in atmospheric and ocean temperatures (Golledge et al., 2015).

## 14.3 Reading oceanic boundary conditions from files

Similar to the atmosphere (section 13.2), evolving oceanic boundary conditions can easily be replaced by spatial fields that stem from (global or regional) climate models.

The fields that can be externally provided are the ocean temperature (`To`) and salinity (`So`), or directly the thermal forcing (`TF`). To do so, the `struct` field `fc` is required in order to specify the location of the externally forced fields (`fc.ocn_XX_fname`, where `XX` may be `To`, `So`, or `TF`) and the frequency of the forcing (see section 14.6).

If the thermal is provided, the `TF` field is directly used. Alternatively, the evolving oceanic properties may be provided separately. If one or several `fc.ocn_XX_fname` are defined, the corresponding fields will be read in every `fc.ocn_cnt` timestep, and this between times `fc.ocn_Tinit` and `fc.ocn_Tend` (see section 14.6).

The input ocean files may be either 2-D (`ctr.imax`, `ctr.jmax`) fields, representing ocean properties on the continental shelf, or 3-D (`ctr.imax`, `ctr.jmax`, `length(fc.z)`) fields, representing the ocean properties at different ocean depths. In the latter case, `fc.z` defining the corresponding ocean depths *must* be provided. If 3-D fields are provided, oceanic properties will be interpolated at the relevant depth, depending on the applied sub-shelf melt scheme (following Burgard et al., 2022).

As PICO uses only one value of temperature and salinity per basin, if 2-D fields are provided to be used by PICO and if `fc.PICO_basins` is defined, oceanic fields of temperature and salinity are averaged over the continental shelf for each of the `fc.PICO_basins` (following Kreuzer et al., 2021).

## 14.4 Imposing a sea-level offset

To modify the global-mean sea level with respect to a reference level (for example in the case of paleo-climate runs), the time-vector `fc.DeltaSL` may be defined. Note that the `fc.DeltaSL` time-vector influences isostatic adjustment via changes in the ocean load (see section 10).

## 14.5 Control parameters for ice-ocean interaction

`ctr.meltfunc` :

- 0** : Constant value of sub-shelf melting equal to the value of `ctr.meltfac` for all ice shelves (default);
- 1** : Melting underneath ice shelves according to the parametrization of Beckmann and Goosse (2003) with linear dependency on the thermal forcing, following (de Boer et al., 2015);
- 2** : Melting underneath ice shelves according to the parametrization of Beckmann and Goosse (2003) with quadratic dependency on the thermal forcing following Pollard and DeConto (2012a);
- 3** : melt based on the PICO ocean-model coupler (Reese et al., 2018a);
- 4** : melt based on the PICOP model (combined PICO and plume model) (Pelle et al., 2019);
- 5** : melt based on the plume model (Pelle et al., 2019);
- 6** : melt as a linear function of ice-shelf thickness (Cornford et al., 2016);
- 7** : uniform melting according to `ctr.meltfac` for `fc.butfac=1`; in this case `fc.butfac` determines the period for which melting is applied; after invoking the melt scheme, `fc.butfac` is put back to 1 in order to keep buttressing applied;
- 8** : removal of all ice shelves; supplementary melting can be applied via `ctr.meltfac`
- 9** : ISMIP6 non-local melt-rate parametrization. If defined, the `fc` fields `fc.deltaT_basin`, `fc.basinNumber`, and `fc.z` must be provided (see below).
- 10** : MISMIP+ melt function;
- 11** : Applying optimized sub-shelf melt/accretion rates to the ice shelves.
- 21** : [To do](#)
- 22** : [To do](#)
- 23** : [To do](#)
- 24** : [To do](#)
- 91** : [To do](#)
- 92** : [To do](#)

**ctr.meltfac** : Amount of basal melting underneath ice shelves (in  $m\ a^{-1}$  if `ctr.meltfunc=0` for example) or multiplier to sub-shelf melt for `ctr.meltfunc=1-5`; default = 0.

**ctr.meltfactor** : `fc.DeltaT` fraction of atmospheric forcing to account for ocean temperature change (used when `ctr.meltfunc>0`); can be used as a tuning/ensemble parameter. Default = 0.3.

**ctr.gammaT** : Effective turbulent temperature exchange velocity ( $m\ s^{-1}$ ); can be used as a tuning/ensemble parameter. Default values for different melting schemes are: 3e-5 for PICO/PICOP; 50e-5 for quadratic; 2e-5 for linear.

**ctr.gammaTpume** : Effective turbulent temperature exchange velocity ( $m\ s^{-1}$ ) for the plume model; can be used as a tuning/ensemble parameter. Default value = 5.9e-4.

**ctr.C = 1e6**: Overturning strength of ocean circulation underneath ice shelf ( $m^3\ s^{-1}$ )

**ctr.M0** : Tuning parameter for the plume/PICOP model. Default values are 5 for Plume; 15 for PICOP.

## 14.6 Forcing parameters for ice-ocean interactions

**fc.DeltaSL** : Scalar time-dependent sea-level offset. Time vector of dimension (`ctr.nsteps`, 1). If not defined, `fc.DeltaSL` is considered to be zero.

**fc.ocn\_To\_fname** : Path directory and name of the 2-D sequential To input files (optional). The files must be named sequentially (starting from 000 and ending by `fc.ocn_snapshots-1` – for example if 10 files are provided, the first file is named `fc.ocn_To_fname000` and the last file is named `fc.ocn_To_fname009`). The 2D field provided in each sequential `fc.ocn_To_fname` file must be named To.

**fc.ocn\_So\_fname** : Path directory and name of the 2-D sequential So input files (optional). The files must be named sequentially (starting from 000 and ending by `fc.ocn_snapshots-1`. The 2D field provided in each sequential `fc.ocn_So_fname` file must be named So.

**fc.ocn\_TF\_fname** : Path directory and name of the 2-D sequential TF input files (optional). The files must be named sequentially (starting from 000 and ending by `fc.ocn_snapshots-1`. The 2D field provided in each sequential `fc.ocn_TF_fname` file must be named TF. Note that if `fc.ocn_TF_fname` is defined, any `fc.ocn_TF_fname` or `fc.ocn_TF_fname` will not be read in.

**fc.ocn\_snapshots** : Total amount of provided oceanic boundary conditions snapshots. Must be defined if any of the `fc.ocn_XX_fname` above is defined.

**fc.ocn\_Tinit** : Year of the first sequential input file. Must be defined if any of the `fc.ocn_XX_fname` above is defined.

**fc.ocn\_Tend** : Year of the last sequential input file. Must be defined if any of the `fc.ocn_XX_fname` above is defined. If `fc.ocn_snapshots=1`, then `fc.ocn_Tinit = fc.ocn_Tend`.

**fc.ocn\_cnt** : Timesteps interval of the sequential input files, i.e., the oceanic inputs will be called every `fc.ocn_cnt` model timesteps. Must be defined if any of the `fc.ocn_XX_fname` above is defined.

**fc.ocn\_nrep** : Number of last oceanic snapshots to repeat if time > `fc.ocn_Tend`. For example, if `fc.ocn_nrep=1`, the last `fc.ocn_XX_fname` file will be re-read every `fc.ocn_cnt` timestep if model time exceeds `fc.ocn_Tend`. Must be defined if any of the `fc.ocn_XX_fname` above is defined and if there is the possibility that model time exceeds `fc.ocn_Tend`.

**fc.basinNumber** : 2-D field (of `(ctr.imax,ctr.jmax)`) identifying the sectors used in ISMIP non-local melt-rate parametrization (Jourdain et al., 2019, needed if `ctr.meltfunc=9`)

**fc.deltaT\_basin** : 2-D field (of `(ctr.imax,ctr.jmax)`) with temperature correction applied to the sectors used in ISMIP non-local melt-rate parametrization (Jourdain et al., 2019, needed if `ctr.meltfunc=9`)

**fc.z** : 1-D vector identifying the depth of provided 3-D oceanic boundary conditions. Must be defined if 3-D ocean boundary conditions are to be read in. Should also be provided with `ctr.meltfunc=9`.

**fc.PICO\_basins** : 2-D field (of `(ctr.imax,ctr.jmax)`) identifying the basins used by PICO basins over which to average oceanic fields of temperature and salinity over the continental shelf (following Kreuzer et al., 2021). As PICO uses one value of temperature and salinity per basin, this field should be provided if 2-D spatially-varying ocean and temperature data are provided and used together with the PICO model (`ctr.meltfunc=3`).

in ISMIP non-local melt-rate parametrization (Jourdain et al., 2019, needed if `ctr.meltfunc=9`)

Below is an example script on how to provide yearly externally-forced oceanic boundary conditions.

```
% READING YEARLY EXTERNAL OCEANIC BOUNDARY CONDITIONS AS OCEANIC FORCING

% example of path directory where forcing files are located
folder_name=['/home/username/Documents/OceanForcingFiles/'];
% files name providing ocean To inputs
fc.ocn_To_fname=[folder_name 'THETA0'];
% files name providing ocean So inputs
fc.ocn_So_fname=[folder_name 'SO'];
% Total amount of snapshots
fc.ocn_snapshots=86;
% Ocean snapshots called every ocean_cnt timesteps -- here: every year
fc.ocn_cnt=1/ctr.dt;
% Time of first snapshot
fc.ocn_Tinit=2015;
% Time of last snapshot
fc.ocn_Tend=2100;
```

```
% Number of last snapshots to repeat if T>Tend -- here: last snapshot  
fc.ocn_nrep=1;
```

## 14.7 Global parameters for ice-ocean interaction

**par.Latent** = 3.35e5: Latent heat of freezing

**par.cp0** = 3974: Heat capacity of ocean water

**par.Soi** = 34.5: ocean salinity (default)

**par.Toi** = -1.7°C: Ocean temperature (default) (Maris et al., 2014)

**par.SeaIceThickness** = 0.1: Thickness of the sea-ice layer uniformly on the ocean domain (m); used to control stress transfer from the modelled domain edges to the ice shelves.

**par.ArcOcean** :

**0** : Not used;

**1** : Calculates the radial opening of ice shelves to open ocean. Used for optimizing basal melt in ice shelves (DeConto and Pollard, 2016).

**par.nbox** = 5: Maximum number of ocean boxes in PICO model

**par.alphao** = 7.5e-5: Thermal expansion coefficient in EOS <sup>2</sup> (°C<sup>-1</sup>)

**par.betao** = 7.7e-4: Salt contraction coefficient in EOS (PSU<sup>-1</sup>)

**par.rhoref** = 1033: Reference density in EOS (kg m<sup>-3</sup>)

**par.lambda1** = -0.0573: Salinity coefficient of freezing equation (°C PSU<sup>-1</sup>)

**par.lambda2** = 0.0832: Constant coefficient of freezing equation (°C)

**par.lambda3** = 7.61e-4: Pressure coefficient (as a function of HB of freezing equation (°C m<sup>-1</sup>)

**par.gamma1** = 0.545: Heat exchange parameter

**par.gamma2** = 3.5e-5: Heat exchange parameter

**par.CdGamT** = 1.1e-3: Turbulent heat exchange coefficient

**par.CdGamTS0** = 6e-4: Heat exchange parameter

**par.C\_eps\_lazero** = 0.6: Slope correction parameter (Lazeroms et al., 2019).

**par.alpha\_coeff\_lazero** = 3.87e-5 ° C<sup>-1</sup>: Thermal expansion coefficient (Lazeroms et al., 2019).

---

<sup>2</sup>EOS: equations of state

**par.beta\_coeff\_lazero** = 7.86e-4 PSU<sup>-1</sup>: Haline contraction coefficient (Lazeroms et al., 2019).

**par.Eo** = 3.6e-2: Entrainment coefficient

**par.Cd** = 2.5e-3: Drag coefficient

**par.x0** = 0.56: Dimensionless scaling factor

**par.pcof** = coefficients for the 11th-degree polynomial describing the melt-refreezing function in Lazeroms et al. (2018).

**par.LatentMelt** =  $\rho_w c_{p0} / (\rho L)$

**par.f\_coriolis** = **To be defined**

**par.BetaS** = **To be defined**

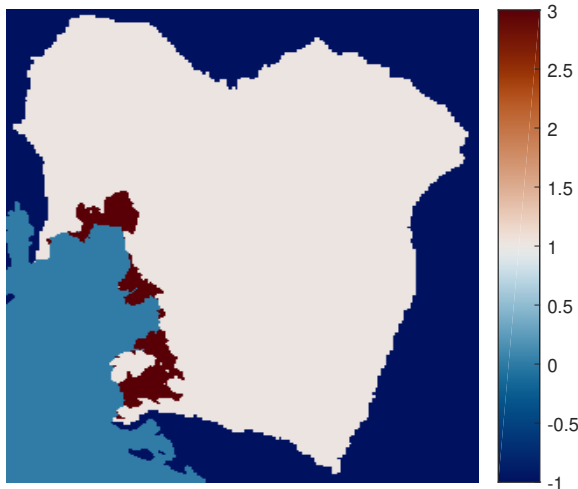


Figure 19: The initial MASK or MASKo used for basin modelling. The value of the grounded ice outside the drainage basin is set to -1.

## 15 Basins and synthetic experiments

### 15.1 Basin modelling

Basin modelling encompasses the simulation of just a part of the ice sheet (drainage basin). This approach requires specific boundary conditions to be applied. It requires to cut out a domain from the ice sheet and define a MASK similar to standard model runs (0 = open ocean; 1 = grounded ice sheet; 3 = ice shelf), and to set MASK=-1 for the grounded regions outside the basins. An example is shown in Figure 19. For the value of MASK = -1, both the ice flow factor A and the basal sliding parameter As are set to very low values, making the ice hard to deform and almost being stagnant. This non-deformable ice zone then forms a boundary condition for the interior basin. Note that changes in the domain of the drainage basin cannot be coped with.

### 15.2 Synthetic geometries

Several international model intercomparisons designed for plan-view and three-dimensional ice flow models build upon a synthetic geometric setup. The early EISMINT experiments (Huybrechts et al., 1996; Payne et al., 2000) were simple in their design and defined by simple and straightforward boundary conditions that every ice sheet model could easily cope with (zero ice thickness on the edge of the square domain). However, subsequent inter-comparisons added a complexity to the boundary conditions, such as the use of periodic boundary conditions or symmetry axes (Pattyn et al., 2008, 2013; Cornford et al., 2020). For `ctr.mismp = 1`, this implies a symmetric ice divide with a no slip condition for  $x = 0$ , a calving front at  $x = x_e$  (where  $x_e$  is the last point of the domain in the  $x$  direction), a symmetric condition at  $y = 0$  and a periodic boundary condition / symmetry axis at  $y = y_e$ , as illustrated in Figure 20.

Another synthetic setup is useful to carry out experiments with a marine ice sheet setup characterized by two symmetry axes in the  $x$  and  $y$  direction (the MISMIP+ experiment has

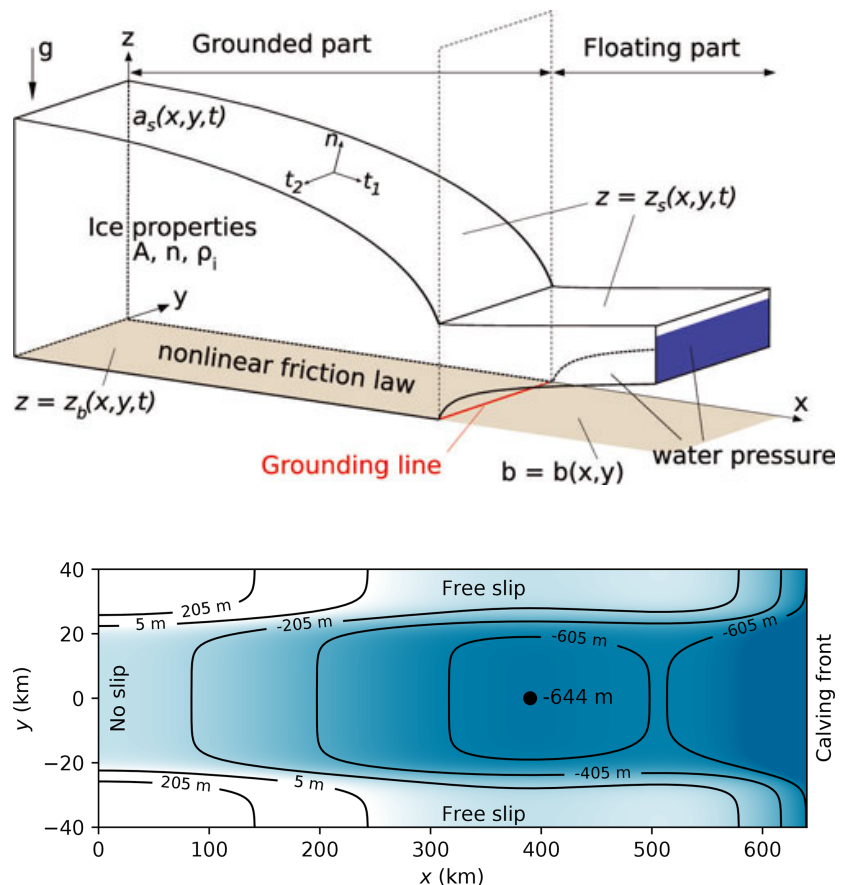


Figure 20: Geometry of the MISMIP3d experiment (Pattyn et al., 2013) and the MISMIP+ experiment (Cornford et al., 2020).

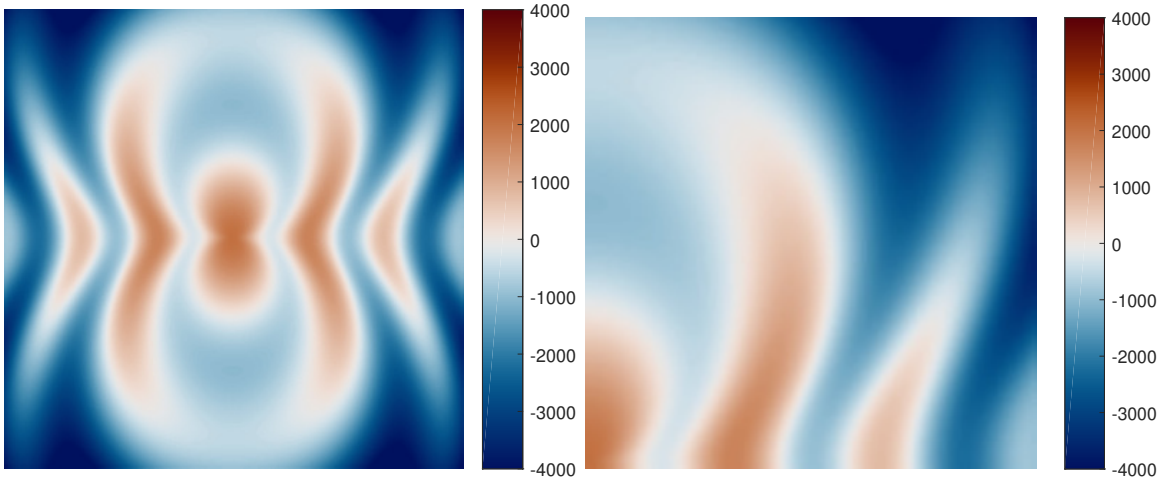


Figure 21: Bedrock geometry of the Thule domain with two symmetry axes (works also for a circular marine ice sheet; left). The option `ctr.mismip = 2` simulates only a quadrant of the domain by considering two symmetry axes at  $x = 0$  and  $y = 0$  (right).

only one symmetry axis). For a circular ice sheet surrounded by ocean, this implies that only one quadrant is simulated and the ocean boundary condition is situated on  $x = x_e$  and  $y = y_e$ , with a symmetry axis on  $x = 0$  and  $y = 0$  (Figure 21).

### 15.3 Control parameters for basins and synthetic experiments

**ctr.basin = 1**: Run the model for a specific basin, based on basin boundaries. Outside the basin boundaries, ice is kept very viscous and basal sliding extremely small. In that case, `MASK = -1` for the grounded areas outside the drainage basin (the entire model domain remains rectangular). Default = 0.

**ctr.mismip = 0** : Standard model run (default)

**1** : Synthetic experiments on a rectangular domain with specific boundary conditions. Use flowband, MISMIP3d or MISMIP+ geometry, i.e., the left boundary of the domain is the ice divide, the right boundary is the ocean. Lateral boundaries are taken as symmetry axis, which means that only half a domain is simulated.

**2** : Use of, e.g., the Thule geometry, where the right and upper lateral boundaries are ocean and symmetric boundaries apply to the left and bottom lateral boundary. These conditions allow to simulate only a quarter of a double-symmetric problem, such as a circular ice sheet.

### 15.4 Global parameters for basins and synthetic experiments

**par.As0 = 1e-20**: Sliding coefficient outside basin

**par.A0 = 1e-20**: Ice fluidity outside basin

## 16 Publications involving Kori–ULB and f.ETISh

23. Li, Y., Coulon, V., Blasco, J., Qiao, G., Yang, Q., and Pattyn, F.: Damage strength increases ice mass loss from Thwaites Glacier, Antarctica, EGUsphere [preprint], <https://doi.org/10.5194/egusphere-2024-2916>, 2024.
22. Kazmierczak, E., Gregov, T., Coulon, V., and Pattyn, F.: A fast and simplified subglacial hydrological model for the Antarctic Ice Sheet and outlet glaciers, *The Cryosphere*, 18, 5887–5911, <https://doi.org/10.5194/tc-18-5887-2024>, 2024.
21. Coulon, V., De Rydt, J., Gregov, T., Qin, Q., and Pattyn, F. (2024). Future freshwater fluxes from the Antarctic ice sheet. *Geophysical Research Letters*, 51, e2024GL111250. <https://doi.org/10.1029/2024GL11125>.
20. Klose, A. K., Coulon, V., Pattyn, F., and Winkelmann, R.: The long-term sea-level commitment from Antarctica, *The Cryosphere*, 18, 4463–4492, <https://doi.org/10.5194/tc-18-4463-2024>, 2024.
19. Seroussi, H. Pelle, T., Lipscomb,W. H., Abe-Ouchi, A., Albrecht, T., Alvarez-Solas, J, et al. (inlcuding F. Pattyn and V. Coulon) (2024). Evolution of the Antarctic Ice Sheet over the next three centuries from an ISMIP6 model ensemble. *Earth's Future* 12, e2024EF004561. <https://doi.org/10.1029/2024EF004561>.
18. Coulon, V., Klose, A. K., Kittel, C., Edwards, T., Turner, F., Winkelmann, R., and Pattyn, F.: Disentangling the drivers of future Antarctic ice loss with a historically calibrated ice-sheet model, *The Cryosphere*, 18, 653, 2024.
17. Seroussi, H., Verjans, V., Nowicki, S., Payne, A. J., Goelzer, H., Lipscomb, W. H., Abe-Ouchi, A., Agosta, C., Albrecht, T., Asay-Davis, X., Barthel, A., Calov, R., Cul-lather, R., Dumas, C., Galton-Fenzi, B. K., Gladstone, R., Golledge, N. R., Gregory, J. M., Greve, R., Hattermann, T., Hoffman, M. J., Humbert, A., Huybrechts, P., Jourdain, N. C., Kleiner, T., Larour, E., Leguy, G. R., Lowry, D. P., Little, C. M., Morlighem, M., Pattyn, F., Pelle, T., Price, S. F., Quiquet, A., Reese, R., Schlegel, N.-J., Shepherd, A., Simon, E., Smith, R. S., Straneo, F., Sun, S., Trusel, L. D., Van Breedam, J., Van Katwyk, P., van de Wal, R. S. W., Winkelmann, R., Zhao, C., Zhang, T., and Zwinger, T.: Insights into the vulnerability of Antarctic glaciers from the ISMIP6 ice sheet model ensemble and associated uncertainty, *The Cryosphere*, 17, 5197–5217, <https://doi.org/10.5194/tc-17-5197-2023>, 2023.
16. Kazmierczak, E., Sun, S., Coulon, V., and Pattyn, F.: Subglacial hydrology modulates basal sliding response of the Antarctic ice sheet to climate forcing, *The Cryosphere*, 16, 4537–4552, <https://doi.org/10.5194/tc-16-4537-2022>, 2022.
15. Pelletier, C., Fichefet, T., Goosse, H., Haubner, K., Helsen, S., Huot, P.-V., Kittel, C., Klein, F., Le clec'h, S., van Lipzig, N. P. M., Marchi, S., Massonnet, F., Mathiot, P., Moravveji, E., Moreno-Chamarro, E., Ortega, P., Pattyn, F., Souverijns, N., Van Achter, G., Vanden Broucke, S., Vanhulle, A., Verfaillie, D., and Zipf, L.: PARASO, a circum-Antarctic fully coupled ice-sheet–ocean–sea-ice–atmosphere–land model involving f.ETISh1.7, NEMO3.6, LIM3.6, COSMO5.0 and CLM4.5, *Geosci. Model Dev.*, 15, 553–594, <https://doi.org/10.5194/gmd-15-553-2022>, 2022.

14. Payne, A. J., Nowicki, S., Abe-Ouchi, A., Agosta, C., Alexander, P., Albrecht, T., et al. (including F. Pattyn) (2021). Future sea level change under CMIP5 and CMIP6 scenarios from the Greenland and Antarctic ice sheets. *Geophysical Research Letters*, 48, e2020GL091741. <https://doi.org/10.1029/2020GL091741>.
13. Edwards, T.L., Nowicki, S., Marzeion, B. et al. (including F. Pattyn) Projected land ice contributions to twenty-first-century sea level rise. *Nature* 593, 74–82 (2021). <https://doi.org/10.1038/s41586-021-03302-y>.
12. Coulon, V., Bulthuis, K., Whitehouse, P. L., Sun, S., Haubner, K., Zipf, L., & Pattyn, F. (2021). Contrasting response of West and East Antarctic ice sheets to glacial isostatic adjustment. *Journal of Geophysical Research: Earth Surface*, 126, e2020JF006003. <https://doi.org/10.1029/2020JF006003>
11. Sun, S., Pattyn, F., Simon, E., Albrecht, T., Cornford, S., Calov, R., . . . Zhang, T. (2020). Antarctic ice sheet response to sudden and sustained ice-shelf collapse (ABUMIP). *Journal of Glaciology*, 1-14. doi:10.1017/jog.2020.67
10. Bulthuis, K., F. Pattyn, M. Arnst (2019) A multifidelity quantile-based approach for confidence sets of random excursion sets with application to ice-sheet dynamics. *SIAM/ASA J. Uncertainty Quantification*, 8(3), 860–890. <https://doi.org/10.1137/19M1280466>
9. Seroussi, H., Nowicki, S., Payne, A. J., Goelzer, H., Lipscomb, W. H., Abe-Ouchi, A., Agosta, C., Albrecht, T., Asay-Davis, X., Barthel, A., Calov, R., Cullather, R., Dumas, C., Galton-Fenzi, B. K., Gladstone, R., Golledge, N. R., Gregory, J. M., Greve, R., Hattermann, T., Hoffman, M. J., Humbert, A., Huybrechts, P., Jourdain, N. C., Kleiner, T., Larour, E., Leguy, G. R., Lowry, D. P., Little, C. M., Morlighem, M., Pattyn, F., Pelle, T., Price, S. F., Quiquet, A., Reese, R., Schlegel, N.-J., Shepherd, A., Simon, E., Smith, R. S., Straneo, F., Sun, S., Trusel, L. D., Van Breedam, J., van de Wal, R. S. W., Winkelmann, R., Zhao, C., Zhang, T., and Zwinger, T.(2020): ISMIP6 Antarctica: a multi-model ensemble of the Antarctic ice sheet evolution over the 21st century, *The Cryosphere*, 14, 3033–3070, <https://doi.org/10.5194/tc-14-3033-2020>.
8. Goelzer, H., Coulon, V., Pattyn, F., de Boer, B., and van de Wal, R.: Brief communication: On calculating the sea-level contribution in marine ice-sheet models , *The Cryosphere*, 14, 833–840, <https://doi.org/10.5194/tc-14-833-2020>, 2020
7. Hanna, E., F. Pattyn, F. Navarro, V. Favier, H. Goelzer, M.R. van den Broeke, M. Vizcaino, P.L. Whitehouse, C. Ritz, K. Bulthuis, B. Smith (2019) Mass balance of the ice sheets and glaciers - progress since AR5 and challenges. *Earth Science Reviews*. 201, doi: 10.1016/j.earscirev.2019.102976.
6. Levermann, A., Winkelmann, R., Albrecht, T., Goelzer, H., Golledge, N. R., Greve, R., Huybrechts, P., Jordan, J., Leguy, G., Martin, D., Morlighem, M., Pattyn, F., Pollard, D., Quiquet, A., Rodehacke, C., Seroussi, H., Sutter, J., Zhang, T., Van Breedam, J., Calov, R., DeConto, R., Dumas, C., Garbe, J., Gudmundsson, G. H., Hoffman, M. J., Humbert, A., Kleiner, T., Lipscomb, W. H., Meinshausen, M., Ng, E., Nowicki, S. M. J., Perego, M., Price, S. F., Saito, F., Schlegel, N.-J., Sun, S., and van de Wal, R. S.

- W.: Projecting Antarctica's contribution to future sea level rise from basal ice shelf melt using linear response functions of 16 ice sheet models (LARMIP-2), *Earth Syst. Dynam.*, 11, 35–76, <https://doi.org/10.5194/esd-11-35-2020>, 2020.
5. Seroussi, H., Nowicki, S., Simon, E., Abe-Ouchi, A., Albrecht, T., Brondex, J., Cornford, S., Dumas, C., Gillet-Chaulet, F., Goelzer, H., Golledge, N. R., Gregory, J. M., Greve, R., Hoffman, M. J., Humbert, A., Huybrechts, P., Kleiner, T., Larour, E., Leguy, G., Lipscomb, W. H., Lowry, D., Mengel, M., Morlighem, M., Pattyn, F., Payne, A. J., Pollard, D., Price, S. F., Quiquet, A., Reerink, T. J., Reese, R., Rodehacke, C. B., Schlegel, N.-J., Shepherd, A., Sun, S., Sutter, J., Van Breedam, J., van de Wal, R. S. W., Winkelmann, R., and Zhang, T.: initMIP-Antarctica: an ice sheet model initialization experiment of ISMIP6, *The Cryosphere*, 13, 1441–1471, <https://doi.org/10.5194/tc-13-1441-2019>, 2019.
  4. Bulthuis, K., Arnst, M., Sun, S., and Pattyn, F.: Uncertainty quantification of the multi-centennial response of the Antarctic ice sheet to climate change, *The Cryosphere*, 13, 1349–1380, <https://doi.org/10.5194/tc-13-1349-2019>, 2019.
  3. Goelzer, H., Nowicki, S., Edwards, T., Beckley, M., Abe-Ouchi, A., Aschwanden, A., Calov, R., Gagliardini, O., Gillet-Chaulet, F., Golledge, N. R., Gregory, J., Greve, R., Humbert, A., Huybrechts, P., Kennedy, J. H., Larour, E., Lipscomb, W. H., Le clec'h, S., Lee, V., Morlighem, M., Pattyn, F., Payne, A. J., Rodehacke, C., Rückamp, M., Saito, F., Schlegel, N., Seroussi, H., Shepherd, A., Sun, S., van de Wal, R., and Ziemen, F. A.: Design and results of the ice sheet model initialisation experiments initMIP-Greenland: an ISMIP6 intercomparison, *The Cryosphere*, 12, 1433–1460
  2. Firas Mourad, Emmanuel Witrant, Frank Pattyn. The Initialization Of Basal Sliding Coefficients For Antarctica, A Lyapunov Based Approach. American Control Conference, Jun 2018, Milwaukee, United States. <hal-01778305>
  1. Pattyn, F.: Sea-level response to melting of Antarctic ice shelves on multi-centennial time scales with the fast Elementary Thermomechanical Ice Sheet model (f.ETISH v1.0), *The Cryosphere* 11, 1851–1878, 2017 doi:10.5194/tc-11-1851-2017.

## References

- Arthern, R. J., Hindmarsh, R. C. A., and Williams, C. R.: Flow speed within the Antarctic ice sheet and its controls inferred from satellite observations, *Journal of Geophysical Research: Earth Surface*, 120, 1171–1188, [https://doi.org/https://doi.org/10.1002/2014JF003239](https://doi.org/10.1002/2014JF003239), 2015.
- Aschwanden, A., Bueler, E., Khroulev, C., and Blatter, H.: An enthalpy formulation for glaciers and ice sheets, *Journal of Glaciology*, 58, 441–457, <https://doi.org/10.3189/2012JoG11J088>, 2012.
- Beckmann, A. and Goosse, H.: A parameterization of ice shelf-ocean interaction for climate models, *Ocean Modelling*, 5, 157 – 170, [https://doi.org/10.1016/S1463-5003\(02\)00019-7](https://doi.org/10.1016/S1463-5003(02)00019-7), 2003.
- Bernales, J., Rogozhina, I., Greve, R., and Thomas, M.: Comparison of hybrid schemes for the combination of shallow approximations in numerical simulations of the Antarctic Ice Sheet, *The Cryosphere*, 11, 247–265, <https://doi.org/10.5194/tc-11-247-2017>, 2017.
- Blatter, H. and Greve, R.: Comparison and verification of enthalpy schemes for polythermal glaciers and ice sheets with a one-dimensional model, *Polar Science*, 9, 196–207, <https://doi.org/10.1016/j.polar.2015.04.001>, 2015.
- Bondzio, J. H., Seroussi, H., Morlighem, M., Kleiner, T., Rückamp, M., Humbert, A., and Larour, E. Y.: Modelling calving front dynamics using a level-set method: application to Jakobshavn Isbræ, West Greenland, *The Cryosphere*, 10, 497–510, <https://doi.org/10.5194/tc-10-497-2016>, 2016.
- Bougamont, M., Christoffersen, P., Hubbard, A. L., Fitzpatrick, A. A., Doyle, S. H., and Carter, S. P.: Sensitive response of the Greenland Ice Sheet to surface melt drainage over a soft bed, *Nature Communications*, 5, 5052, <https://doi.org/10.1038/ncomms6052>, 2014.
- Bueler, E. and Brown, J.: Shallow shelf approximation as a “sliding law” in a thermomechanically coupled ice sheet model, *Journal of Geophysical Research: Earth Surface*, 114, <https://doi.org/10.1029/2008JF001179>, f03008, 2009.
- Bueler, E. and van Pelt, W.: Mass-conserving subglacial hydrology in the Parallel Ice Sheet Model version 0.6, *Geoscientific Model Development*, 8, 1613–1635, <https://doi.org/10.5194/gmd-8-1613-2015>, 2015.
- Bulthuis, K., Arnst, M., Sun, S., and Pattyn, F.: Uncertainty quantification of the multi-centennial response of the Antarctic ice sheet to climate change, *The Cryosphere*, 13, 1349–1380, <https://doi.org/10.5194/tc-13-1349-2019>, 2019.
- Burgard, C., Jourdain, N. C., Reese, R., Jenkins, A., and Mathiot, P.: An assessment of basal melt parameterisations for Antarctic ice shelves, *The Cryosphere*, 16, 4931–4975, <https://doi.org/10.5194/tc-16-4931-2022>, 2022.
- Calov, R. and Greve, R.: A semi-analytical solution for the positive degree-day model with stochastic temperature variations, *Journal of Glaciology*, 51, 2005.

- Chen, B., Haeger, C., Kaban, M. K., and Petrunin, A. G.: Variations of the effective elastic thickness reveal tectonic fragmentation of the Antarctic lithosphere, *Tectonophysics*, <https://doi.org/http://dx.doi.org/10.1016/j.tecto.2017.06.012>, 2017.
- Clarke, G. K. C.: Lumped-Element Analysis of Subglacial Hydraulic Circuits, *J. Geophys. Res.*, 101, 17 547–17 599, 1996.
- Cornford, S. L., Martin, D. F., Graves, D. T., Ranken, D. F., LeBrocq, A. M., Gladstone, R. M., Payne, A. J., Ng, E. G., and Lipscomb, W. H.: Adaptive Mesh, Finite Volume Modeling of Marine Ice Sheets, *J. Comput. Phys.*, 232, 529–549, 2013.
- Cornford, S. L., Martin, D. F., Lee, V., Payne, A. J., and Ng, E. G.: Adaptive mesh refinement versus subgrid friction interpolation in simulations of Antarctic ice dynamics, *Annals of Glaciology*, 57, 1–9, <https://doi.org/10.1017/aog.2016.13>, 2016.
- Cornford, S. L., Seroussi, H., Asay-Davis, X. S., Gudmundsson, G. H., Arthern, R., Borstad, C., Christmann, J., Dias dos Santos, T., Feldmann, J., Goldberg, D., Hoffman, M. J., Humbert, A., Kleiner, T., Leguy, G., Lipscomb, W. H., Merino, N., Durand, G., Morlighem, M., Pollard, D., Rückamp, M., Williams, C. R., and Yu, H.: Results of the third Marine Ice Sheet Model Intercomparison Project (MISMIP+), *The Cryosphere*, 14, 2283–2301, <https://doi.org/10.5194/tc-14-2283-2020>, 2020.
- Coulon, V., Bulthuis, K., Whitehouse, P. L., Sun, S., Haubner, K., Zipf, L., and Pattyn, F.: Contrasting Response of West and East Antarctic Ice Sheets to Glacial Isostatic Adjustment, *Journal of Geophysical Research: Earth Surface*, 126, e2020JF006 003, <https://doi.org/https://doi.org/10.1029/2020JF006003>, e2020JF006003 2020JF006003, 2021.
- Coulon, V., Klose, A. K., Kittel, C., Edwards, T., Turner, F., Winkelmann, R., and Pattyn, F.: Disentangling the drivers of future Antarctic ice loss with a historically-calibrated ice-sheet model, *EGUphere*, 2023, 1–42, <https://doi.org/10.5194/egusphere-2023-1532>, 2023.
- de Boer, B., Dolan, A. M., Bernales, J., Gasson, E., Goelzer, H., Golledge, N. R., Sutter, J., Huybrechts, P., Lohmann, G., Rogozhina, I., Abe-Ouchi, A., Saito, F., and van de Wal, R. S. W.: Simulating the Antarctic ice sheet in the late-Pliocene warm period: PLISMIP-ANT, an ice-sheet model intercomparison project, *The Cryosphere*, 9, 881–903, <https://doi.org/10.5194/tc-9-881-2015>, 2015.
- DeConto, R. M. and Pollard, D.: Contribution of Antarctica to past and future sea-level rise, *Nature*, 531, 591–597, <https://doi.org/10.1038/nature17145>, 2016.
- Drews, R., Pattyn, F., Hewitt, I. J., Ng, F. S. L., Berger, S., Matsuoka, K., Helm, V., Bergeot, N., Favier, L., and Neckel, N.: Actively evolving subglacial conduits and eskers initiate ice shelf channels at an Antarctic grounding line, *Nature Communications*, 8, <https://doi.org/10.1038/ncomms15228>, 2017.
- Durand, G. and Pattyn, F.: Reducing uncertainties in projections of Antarctic ice mass loss, *The Cryosphere*, 9, 2043–2055, <https://doi.org/10.5194/tc-9-2043-2015>, 2015.

- Durand, G., Gagliardini, O., Zwinger, T., Le Meur, E., and Hindmarsh, R. C.: Full Stokes modeling of marine ice sheets: influence of the grid size, *Annals of Glaciology*, 50, 109–114, <https://doi.org/doi:10.3189/172756409789624283>, 2009.
- Edwards, T. L., Nowicki, S., Marzeion, B., Hock, R., Goelzer, H., Seroussi, H., Jourdain, N. C., Slater, D. A., Turner, F. E., Smith, C. J., McKenna, C. M., Simon, E., Abe-Ouchi, A., Gregory, J. M., Larour, E., Lipscomb, W. H., Payne, A. J., Shepherd, A., Agosta, C., Alexander, P., Albrecht, T., Anderson, B., Asay-Davis, X., Aschwanden, A., Barthel, A., Bliss, A., Calov, R., Chambers, C., Champollion, N., Choi, Y., Cullather, R., Cuzzone, J., Dumas, C., Felikson, D., Fettweis, X., Fujita, K., Galton-Fenzi, B. K., Gladstone, R., Golledge, N. R., Greve, R., Hattermann, T., Hoffman, M. J., Humbert, A., Huss, M., Huybrechts, P., Immerzeel, W., Kleiner, T., Kraaijenbrink, P., Le clec'h, S., Lee, V., Leguy, G. R., Little, C. M., Lowry, D. P., Malles, J.-H., Martin, D. F., Maussion, F., Morlighem, M., O'Neill, J. F., Nias, I., Pattyn, F., Pelle, T., Price, S. F., Quiquet, A., Radić, V., Reese, R., Rounce, D. R., Rückamp, M., Sakai, A., Shafer, C., Schlegel, N.-J., Shannon, S., Smith, R. S., Straneo, F., Sun, S., Tarasov, L., Trusel, L. D., Van Breedam, J., van de Wal, R., van den Broeke, M., Winkelmann, R., Zekollari, H., Zhao, C., Zhang, T., and Zwinger, T.: Projected land ice contributions to twenty-first-century sea level rise, *Nature*, 593, 74–82, <https://doi.org/10.1038/s41586-021-03302-y>, 2021.
- Farrell, W. E. and Clark, J. A.: On Postglacial Sea Level, *Geophysical Journal of the Royal Astronomical Society*, 46, 647–667, <https://doi.org/https://doi.org/10.1111/j.1365-246X.1976.tb01252.x>, 1976.
- Favier, L., Jourdain, N. C., Jenkins, A., Merino, N., Durand, G., Gagliardini, O., Gillet-Chaulet, F., and Mathiot, P.: Assessment of sub-shelf melting parameterisations using the ocean–ice-sheet coupled model NEMO(v3.6)–Elmer/Ice(v8.3), *Geoscientific Model Development*, 12, 2255–2283, <https://doi.org/10.5194/gmd-12-2255-2019>, 2019.
- Flowers, G. E.: Modelling water flow under glaciers and ice sheets, *Proceedings of the Royal Society of London A: Mathematical, Physical and Engineering Sciences*, 471, <https://doi.org/10.1098/rspa.2014.0907>, 2015.
- Frieler, K., Clark, P. U., He, F., Buzert, C., Reese, R., Ligtenberg, S. R. M., van den Broeke, M. R., Winkelmann, R., and Levermann, A.: Consistent evidence of increasing Antarctic accumulation with warming, *Nature Climate Change*, 5, 348 EP –, URL <https://doi.org/10.1038/nclimate2574>, 2015.
- Gagliardini, O., Cohen, D., Raback, P., and Zwinger, T.: Finite-element modeling of sub-glacial cavities and related friction law, *J. Geophys. Res.*, 112, n/a–n/a, <https://doi.org/10.1029/2006JF000576>, 2007.
- Gandy, N., Gregoire, L. J., Ely, J. C., Cornford, S. L., Clark, C. D., and Hodgson, D. M.: Exploring the ingredients required to successfully model the placement, generation, and evolution of ice streams in the British-Irish Ice Sheet, *Quaternary Science Reviews*, 223, 105 915, <https://doi.org/https://doi.org/10.1016/j.quascirev.2019.105915>, 2019.
- Garbe, J., Albrecht, T., Levermann, A., Donges, J. F., and Winkelmann, R.: The hysteresis of the Antarctic Ice Sheet, *Nature*, 585, 538–544, <https://doi.org/10.1038/s41586-020-2727-5>, 2020.

- Gladstone, R. M., Payne, A. J., and Cornford, S. L.: Parameterising the Grounding Line in Ice Sheet Models, *The Cryosphere*, 4, 605–619, <https://doi.org/10.5194/tc-4-605-2010>, 2010.
- Glen, J. W.: The Creep of Polycrystalline Ice, *Proc. Royal. Soc. London A*, 228, 519–538, 1955.
- Goeller, S., Thoma, M., Grosfeld, K., and Miller, H.: A balanced water layer concept for subglacial hydrology in large-scale ice sheet models, *The Cryosphere*, 7, 1095–1106, <https://doi.org/10.5194/tc-7-1095-2013>, 2013.
- Goelzer, H., Coulon, V., Pattyn, F., de Boer, B., and van de Wal, R.: Brief communication: On calculating the sea-level contribution in marine ice-sheet models, *The Cryosphere*, 14, 833–840, <https://doi.org/10.5194/tc-14-833-2020>, 2020.
- Goldberg, D. N.: A variationally derived, depth-integrated approximation to a higher-order glaciological flow model, *Journal of Glaciology*, 57, 157–170, <https://doi.org/10.3189/002214311795306763>, 2011.
- Golledge, N., Keller, E., Gomez, N., Naughten, K., Bernales, J., Trusel, L., and Edwards, T.: Global environmental consequences of twenty-first-century ice-sheet melt, *Nature*, 566, 65–72, 2019.
- Golledge, N. R., Kowalewski, D. E., Naish, T. R., Levy, R. H., Fogwill, C. J., and Gasson, E. G. W.: The multi-millennial Antarctic commitment to future sea-level rise, *Nature*, 526, 421–425, 2015.
- Gowan, E. J., Hinck, S., Niu, L., Clason, C., and Lohmann, G.: The impact of spatially varying ice sheet basal conditions on sliding at glacial time scales, *Journal of Glaciology*, pp. 1–15, <https://doi.org/10.1017/jog.2022.125>, 2023.
- Greve, R. and Blatter, H.: *Dynamics of Ice Sheets and Glaciers*, Berlin, Springer, 2009.
- Greve, R. and Blatter, H.: Comparison of thermodynamics solvers in the polythermal ice sheet model SICOPOLIS, *Polar Science*, 10, 11–23, <https://doi.org/10.1016/j.polar.2015.12.004>, 2016.
- Gudmundsson, G. H., Krug, J., Durand, G., Favier, L., and Gagliardini, O.: The Stability of Grounding Lines on Retrograde Slopes, *The Cryosphere Discuss.*, 6, 2597–2619, <https://doi.org/10.5194/tcd-6-2597-2012>, 2012.
- Helanow, C., Iverson, N. R., Woodard, J. B., and Zoet, L. K.: A slip law for hard-bedded glaciers derived from observed bed topography, *Science Advances*, 7, <https://doi.org/10.1126/sciadv.abe7798>, 2021.
- Hewitt, I. J. and Schoof, C.: Models for polythermal ice sheets and glaciers, *The Cryosphere*, 11, 541–551, <https://doi.org/10.5194/tc-11-541-2017>, 2017.
- Hindmarsh, R. C. A.: On the Numerical Computation of Temperature in an Ice Sheet, *J. Glaciol.*, 45, 568–574, 1999.

- Hindmarsh, R. C. A.: Notes on Basic Glaciological Computational Methods and Algorithms, in: Continuum Mechanics and Applications in Geophysics and the Environment, edited by Straughan, B., Greve, R., Ehrentraut, H., and Wang, Y., pp. 222–249, Springer Verlag, Berlin, 2001.
- Holland, D. M. and Jenkins, A.: Modeling Thermodynamic Ice-Ocean Interactions at the Base of an Ice Shelf, *J. Phys. Oceanogr.*, 29, 1787–1800, 1999.
- Holland, P. R., Jenkins, A., and Holland, D. M.: The response of ice shelf basal melting to variations in ocean temperature., *Journal of Climate*, 21, 2008.
- Hutter, K.: Theoretical Glaciology, Dordrecht, Kluwer Academic Publishers, 1983.
- Huybrechts, P.: The Antarctic Ice Sheet and Environmental Change: a Three-Dimensional Modelling Study, *Berichte für Polarforschung*, 99, 1–241, 1992.
- Huybrechts, P. and de Wolde, J.: The dynamic response of the Greenland and Antarctic ice sheets to multiple-century climatic warming, *Journal of Climate*, 12, 2169–2188, 1999.
- Huybrechts, P., Payne, A., and The EISMINT Intercomparison Group: The EISMINT Benchmarks for Testing Ice-Sheet Models, *Ann. Glaciol.*, 23, 1–12, 1996.
- Huybrechts, P., Abe-Ouchi, A., Marsiat, I., Pattyn, F., Payne, A., Ritz, C., and Romme-laere, V.: Report of the Third EISMINT Workshop on Model Intercomparison, European Science Foundation (Strasbourg), 1998.
- Janssens, I. and Huybrechts, P.: The treatment of meltwater retention in mass-balance parameterisations of the Greenland ice sheet, *Annals of Glaciology*, 31, 133–140, 2000.
- Jenkins, A.: A one-dimensional model of ice shelf-ocean interaction, *Journal of Geophysical Research: Oceans*, 96, 20 671–20 677, <https://doi.org/10.1029/91JC01842>, 1991.
- Joughin, I., Smith, B. E., and Schoof, C. G.: Regularized Coulomb Friction Laws for Ice Sheet Sliding: Application to Pine Island Glacier, Antarctica, *Geophysical Research Letters*, 46, 4764–4771, <https://doi.org/https://doi.org/10.1029/2019GL082526>, 2019.
- Jourdain, N. C., Asay-Davis, X., Hattermann, T., Straneo, F., Seroussi, H., Little, C. M., and Nowicki, S.: A protocol for calculating basal melt rates in the ISMIP6 Antarctic ice sheet projections, *The Cryosphere Discussions*, 2019, 1–33, <https://doi.org/10.5194/tc-2019-277>, 2019.
- Katz, R. F. and Worster, M. G.: Stability of ice-sheet grounding lines, *Proceedings of the Royal Society of London A: Mathematical, Physical and Engineering Sciences*, pp. n/a–n/a, <https://doi.org/10.1098/rspa.2009.0434>, 2010.
- Kazmierczak, E., Sun, S., Coulon, V., and Pattyn, F.: Subglacial hydrology modulates basal sliding response of the Antarctic ice sheet to climate forcing, *The Cryosphere*, 16, 4537–4552, <https://doi.org/10.5194/tc-16-4537-2022>, 2022.
- Kazmierczak, E., Gregov, T., Coulon, V., and Pattyn, F.: A fast and simplified subglacial hydrological model for the Antarctic Ice Sheet and outlet glaciers, *The Cryosphere*, 18, 5887–5911, <https://doi.org/10.5194/tc-18-5887-2024>, 2024.

- Kleiner, T., Rückamp, M., Bondzio, J. H., and Humbert, A.: Enthalpy benchmark experiments for numerical ice sheet models, *The Cryosphere*, 9, 217–228, <https://doi.org/10.5194/tc-9-217-2015>, 2015.
- Kreuzer, M., Reese, R., Huiskamp, W. N., Petri, S., Albrecht, T., Feulner, G., and Winkelmann, R.: Coupling framework (1.0) for the PISM (1.1.4) ice sheet model and the MOM5 (5.1.0) ocean model via the PICCO ice shelf cavity model in an Antarctic domain, *Geoscientific Model Development*, 14, 3697–3714, <https://doi.org/10.5194/gmd-14-3697-2021>, 2021.
- Larour, E., Seroussi, H., Morlighem, M., and Rignot, E.: Continental scale, high order, high spatial resolution, ice sheet modeling using the Ice Sheet System Model (ISSM), *Journal of Geophysical Research: Earth Surface*, 117, n/a–n/a, <https://doi.org/10.1029/2011JF002140>, 2012.
- Lazeroms, W. M. J., Jenkins, A., Gudmundsson, G. H., and van de Wal, R. S. W.: Modelling present-day basal melt rates for Antarctic ice shelves using a parametrization of buoyant meltwater plumes, *The Cryosphere*, 12, 49–70, <https://doi.org/10.5194/tc-12-49-2018>, 2018.
- Lazeroms, W. M. J., Jenkins, A., Rienstra, S. W., and van de Wal, R. S. W.: An Analytical Derivation of Ice-Shelf Basal Melt Based on the Dynamics of Meltwater Plumes, *Journal of Physical Oceanography*, 49, 917 – 939, <https://doi.org/https://doi.org/10.1175/JPO-D-18-0131.1>, 2019.
- Le Brocq, A., Payne, A., Siegert, M., and Alley, R.: A subglacial water-flow model for West Antarctica, *Journal of Glaciology*, 55, 879–888, <https://doi.org/10.3189/002214309790152564>, 2009.
- Le Brocq, A. M., Payne, A. J., and Siegert, M. J.: West Antarctic Balance Calculations: Impact of Flux-Routing Algorithm, Smoothing Algorithm and Topography, *Computers and Geosciences*, 32, 1780–1795, 2006.
- Levermann, A., Albrecht, T., Winkelmann, R., Martin, M. A., Haseloff, M., and Joughin, I.: Kinematic first-order calving law implies potential for abrupt ice-shelf retreat, *The Cryosphere*, 6, 273–286, <https://doi.org/10.5194/tc-6-273-2012>, 2012.
- Lipscomb, W. H., Price, S. F., Hoffman, M. J., Leguy, G. R., Bennett, A. R., Bradley, S. L., Evans, K. J., Fyke, J. G., Kennedy, J. H., Perego, M., Ranken, D. M., Sacks, W. J., Salinger, A. G., Vargo, L. J., and Worley, P. H.: Description and evaluation of the Community Ice Sheet Model (CISM) v2.1, *Geoscientific Model Development*, 12, 387–424, <https://doi.org/10.5194/gmd-12-387-2019>, 2019.
- Lliboutry, L.: A critical review of analytical approximate solutions for steady state velocities and temperatures in cold ice-sheets, *Zeitschrift für Gletscherkunde und Glazialgeologie*, 35, 135–148, 1979.
- Lüthi, M., Funk, M., Iken, A., Gogineni, S., and Truffer, M.: Mechanisms of fast flow in Jakobshavn Isbræ, West Greenland: Part III. Measurements of ice deformation, temperature and cross-borehole conductivity in boreholes to the bedrock, *Journal of Glaciology*, 48, 369–385, <https://doi.org/10.3189/172756502781831322>, 2002.

- Ma, Y., Gagliardini, O., Ritz, C., Gillet-Chaulet, F., Durand, G., and Montagnat, M.: Enhancement factors for grounded ice and ice shelves inferred from an anisotropic ice-flow model, *Journal of Glaciology*, 56, 805–812, <https://doi.org/10.3189/002214310794457209>, 2010.
- MacAyeal, D. R.: Large-scale Ice Flow over a Viscous Basal Sediment: Theory and Application to Ice Stream B, Antarctica, *J. Geophys. Res.*, 94, 4071–4087, 1989.
- Maris, M. N. A., de Boer, B., Ligtenberg, S. R. M., Crucifix, M., van de Berg, W. J., and Oerlemans, J.: Modelling the evolution of the Antarctic ice sheet since the last interglacial, *The Cryosphere*, 8, 1347–1360, <https://doi.org/10.5194/tc-8-1347-2014>, 2014.
- Martin, M. A., Winkelmann, R., Haseloff, M., Albrecht, T., Bueler, E., Khroulev, C., and Levermann, A.: The Potsdam Parallel Ice Sheet Model (PISM-PIK) Part 2: Dynamic equilibrium simulation of the Antarctic ice sheet, *The Cryosphere*, 5, 727–740, <https://doi.org/10.5194/tc-5-727-2011>, 2011.
- Morland, L.: Unconfined Ice-Shelf Flow, in: Dynamics of the West Antarctica Ice Sheet, edited by van der Veen, C. J. and Oerlemans, J., pp. 99–116, Kluwer Acad., Dordrecht, Netherlands, 1987.
- Morlighem, M., Bondzio, J., Seroussi, H., Rignot, E., Larour, E., Humbert, A., and Rebuffi, S.: Modeling of Store Gletscher’s calving dynamics, West Greenland, in response to ocean thermal forcing, *Geophysical Research Letters*, 43, 2659–2666, <https://doi.org/10.1002/2016GL067695>, 2016.
- Morlighem, M., Rignot, E., Binder, T., Blankenship, D., Drews, R., Eagles, G., Eisen, O., Ferraccioli, F., Forsberg, R., Fretwell, P., Goel, V., Greenbaum, J. S., Gudmundsson, H., Guo, J., Helm, V., Hofstede, C., Howat, I., Humbert, A., Jokat, W., Karlsson, N. B., Lee, W. S., Matsuoka, K., Millan, R., Mouginot, J., Paden, J., Pattyn, F., Roberts, J., Rosier, S., Ruppel, A., Seroussi, H., Smith, E. C., Steinhage, D., Sun, B., Broeke, M. R. v. d., Ommen, T. D. v., Wessem, M. v., and Young, D. A.: Deep glacial troughs and stabilizing ridges unveiled beneath the margins of the Antarctic ice sheet, *Nature Geoscience*, <https://doi.org/10.1038/s41561-019-0510-8>, 2019.
- Olbers, D. and Hellmer, H.: A box model of circulation and melting in ice shelf caverns, *Ocean Dynamics*, 60, 141–153, <https://doi.org/10.1007/s10236-009-0252-z>, 2010.
- Osher, S. and Fedkiw, R. P.: Level Set Methods: An Overview and Some Recent Results, *Journal of Computational Physics*, 169, 463–502, <https://doi.org/10.1006/jcph.2000.6636>, 2001.
- Paterson, W. S. B.: *The Physics of Glaciers*, Oxford, Pergamon Press, 3rd edn., 1994.
- Pattyn, F.: GRANTISM: An ExcelTM Model for Greenland and Antarctic Ice-sheet Response to Climate Changes, *Comput. Geosci.*, 32, 316–325, <https://doi.org/10.1016/j.cageo.2005.06.020>, 2006.
- Pattyn, F.: Antarctic Subglacial Conditions inferred from a Hybrid Ice Sheet/Ice Stream Model, *Earth Planet. Sci. Lett.*, 295, 451–461, 2010.

- Pattyn, F.: Sea-level response to melting of Antarctic ice shelves on multi-centennial timescales with the fast Elementary Thermomechanical Ice Sheet model (f.ETISh v1.0), *The Cryosphere*, 11, 1851–1878, <https://doi.org/10.5194/tc-11-1851-2017>, 2017.
- Pattyn, F. and Durand, G.: Why marine ice sheet model predictions may diverge in estimating future sea level rise, *Geophysical Research Letters*, 40, 4316–4320, <https://doi.org/10.1002/grl.50824>, 2013.
- Pattyn, F., De Brabander, S., and Huyghe, A.: Basal and Thermal Control Mechanisms of the Ragnhild Glaciers, East Antarctica, *Ann. Glaciol.*, 40, 225–231, 2005.
- Pattyn, F., Huyghe, A., De Brabander, S., and De Smedt, B.: Role of transition zones in marine ice sheet dynamics, *Journal of Geophysical Research: Earth Surface*, 111, n/a–n/a, <https://doi.org/10.1029/2005JF000394>, f02004, 2006.
- Pattyn, F., Perichon, L., Aschwanden, A., Breuer, B., De Smedt, B., Gagliardini, O., Gudmundsson, G. H., Hindmarsh, R. C. A., Hubbard, A., Johnson, J. V., Kleiner, T., Konovalov, Y., Martin, C., Payne, A. J., Pollard, D., Price, S., Rückamp, M., Saito, F., Soucek, O., Sugiyama, S., and Zwinger, T.: Benchmark Experiments for Higher-Order and Full-Stokes Ice Sheet Models (ISMIP–HOM), *The Cryosphere*, 2, 95–108, 2008.
- Pattyn, F., Schoof, C., Perichon, L., Hindmarsh, R. C. A., Bueler, E., de Fleurian, B., Durand, G., Gagliardini, O., Gladstone, R., Goldberg, D., Gudmundsson, G. H., Huybrechts, P., Lee, V., Nick, F. M., Payne, A. J., Pollard, D., Rybak, O., Saito, F., and Vieli, A.: Results of the Marine Ice Sheet Model Intercomparison Project, MISMIP, *The Cryosphere*, 6, 573–588, <https://doi.org/10.5194/tc-6-573-2012>, 2012.
- Pattyn, F., Perichon, L., Durand, G., Favier, L., Gagliardini, O., Hindmarsh, R. C., Zwinger, T., Albrecht, T., Cornford, S., Docquier, D., Fürst, J. J., Goldberg, D., Gudmundsson, G. H., Humbert, A., Hütten, M., Huybrechts, P., Jouvet, G., Kleiner, T., Larour, E., Martin, D., Morlighem, M., Payne, A. J., Pollard, D., Rückamp, M., Rybak, O., Seroussi, H., Thoma, M., and Wilkens, N.: Grounding-line migration in plan-view marine ice-sheet models: results of the ice2sea MISMIP3d intercomparison, *Journal of Glaciology*, 59, 410–422, <https://doi.org/10.3189/2013JoG12J129>, 2013.
- Payne, A. J. and Dongelmans, P. W.: Self-organisation in the Thermomechanical Flow of Ice Sheets, *J. Geophys. Res.*, 102, 12 219–12 234, 1997.
- Payne, A. J., Huybrechts, P., Abe-Ouchi, A., Calov, R., Fastook, J. L., Greve, R., Marshall, S. J., Marsiat, I., Ritz, C., Tarasov, L., and Thomassen, M.: Results from the EISMINT Model Intercomparison: the Effects of Thermomechanical Coupling, *J. Glaciol.*, 46, 227–238, 2000.
- Pelle, T., Morlighem, M., and Bondzio, J. H.: Brief communication: PICOP, a new ocean melt parameterization under ice shelves combining PICO and a plume model, *The Cryosphere*, 13, 1043–1049, <https://doi.org/10.5194/tc-13-1043-2019>, 2019.
- Pelletier, C., Fichefet, T., Goosse, H., Haubner, K., Helsen, S., Huot, P.-V., Kittel, C., Klein, F., Le clec'h, S., van Lipzig, N. P. M., Marchi, S., Massonnet, F., Mathiot, P., Moravveji,

- E., Moreno-Chamarro, E., Ortega, P., Pattyn, F., Souverijns, N., Van Achter, G., Vanden Broucke, S., Vanhulle, A., Verfaillie, D., and Zipf, L.: PARASO, a circum-Antarctic fully-coupled ice-sheet - ocean - sea-ice - atmosphere - land model involving f.ETISH1.7, NEMO3.6, LIM3.6, COSMO5.0 and CLM4.5, Geoscientific Model Development Discussions, 2021, 1–59, <https://doi.org/10.5194/gmd-2021-315>, 2021.
- Pollard, D. and DeConto, R. M.: Modelling West Antarctic Ice Sheet Growth and Collapse Through the Past Five Million Years, *Nature*, 458, 329–332, <https://doi.org/10.1038/nature07809>, 2009.
- Pollard, D. and DeConto, R. M.: Description of a Hybrid Ice Sheet-Shelf Model, and Application to Antarctica, *Geosci. Model Dev.*, 5, 1273–1295, <https://doi.org/10.5194/gmd-5-1273-2012>, 2012a.
- Pollard, D. and DeConto, R. M.: A simple inverse method for the distribution of basal sliding coefficients under ice sheets, applied to Antarctica, *The Cryosphere*, 6, 953–971, <https://doi.org/10.5194/tc-6-953-2012>, 2012b.
- Pollard, D., DeConto, R. M., and Alley, R. B.: Potential Antarctic Ice Sheet retreat driven by hydrofracturing and ice cliff failure, *Earth and Planetary Science Letters*, 412, 112 – 121, 2015.
- Quiquet, A., Dumas, C., Ritz, C., Peyaud, V., and Roche, D. M.: The GRISLI ice sheet model (version 2.0): calibration and validation for multi-millennial changes of the Antarctic ice sheet, *Geoscientific Model Development Discussions*, 2018, 1–35, <https://doi.org/10.5194/gmd-2018-105>, 2018.
- Raspoet, O. and Pattyn, F.: Estimates of basal and englacial thermal conditions of the Antarctic ice sheet, *J. Glaciol.*, xx, xx–xx, 2025.
- Reeh, N.: Parameterization of melt rate and surface temperature on the Greenland ice sheet, *Polarforschung*, 59, 113–128, 1989.
- Reeh, N.: Parameterization of melt rate and surface temperature in the Greenland ice sheet, *Polarforschung*, 59, 1991.
- Reese, R., Albrecht, T., Mengel, M., Asay-Davis, X., and Winkelmann, R.: Antarctic sub-shelf melt rates via PICO, *The Cryosphere*, 12, 1969–1985, <https://doi.org/10.5194/tc-12-1969-2018>, 2018a.
- Reese, R., Winkelmann, R., and Gudmundsson, G. H.: Grounding-line flux formula applied as a flux condition in numerical simulations fails for buttressed Antarctic ice streams, *The Cryosphere*, 12, 3229–3242, <https://doi.org/10.5194/tc-12-3229-2018>, 2018b.
- Reijmer, C. H., van den Broeke, M. R., Fettweis, X., Ettema, J., and Stap, L. B.: Refreezing on the Greenland ice sheet: a comparison of parameterizations, *The Cryosphere*, 6, 743–762, <https://doi.org/10.5194/tc-6-743-2012>, 2012.
- Rignot, E., Mouginot, J., and Scheuchl, B.: Ice Flow of the Antarctic Ice Sheet, *Science*, 333, 1427–1430, 2011.

- Ritz, C.: Time Dependent Boundary Conditions for Calculation of Temperature Fields in Ice Sheets, IAHS Publ., 170, 207–216, 1987.
- Ritz, C.: Un Modèle Thermo-Mécanique d’Evolution pour le Bassin Glaciaire Antarctique Vostok-Glacier Byrd: Sensibilité aux Valeurs des Paramètres Mal Connus, PhD Thesis, Univ. J. Fourier, 1992.
- Robinson, A., Goldberg, D., and Lipscomb, W. H.: A comparison of the stability and performance of depth-integrated ice-dynamics solvers, *The Cryosphere*, 16, 689–709, <https://doi.org/10.5194/tc-16-689-2022>, 2022.
- Rommelaere, V. and Ritz, C.: A thermomechanical model of ice-shelf flow, *Annals of Glaciology*, 23, 13–20, 1996.
- Schmidtko, S., Heywood, K. J., Thompson, A. F., and Aoki, S.: Multidecadal warming of Antarctic waters, *Science*, 346, 1227–1231, <https://doi.org/10.1126/science.1256117>, 2014.
- Schoof, C.: The effect of cavitation on glacier sliding, *Proc. R. Soc. Lond. A*, 461, 609–627, <https://doi.org/10.1098/rspa.2004.1350>, 2005.
- Schoof, C.: Ice sheet grounding line dynamics: Steady states, stability, and hysteresis, *Journal of Geophysical Research: Earth Surface*, 112, n/a–n/a, <https://doi.org/10.1029/2006JF000664>, f03S28, 2007.
- Schoof, C.: Ice-sheet acceleration driven by melt supply variability, *Nature*, 468, 803–806, 2010.
- Seroussi, H., Nowicki, S., Payne, A. J., Goelzer, H., Lipscomb, W. H., Abe-Ouchi, A., Agosta, C., Albrecht, T., Asay-Davis, X., Barthel, A., Calov, R., Cullather, R., Dumas, C., Galton-Fenzi, B. K., Gladstone, R., Golledge, N. R., Gregory, J. M., Greve, R., Hattermann, T., Hoffman, M. J., Humbert, A., Huybrechts, P., Jourdain, N. C., Kleiner, T., Larour, E., Leguy, G. R., Lowry, D. P., Little, C. M., Morlighem, M., Pattyn, F., Pelle, T., Price, S. F., Quiquet, A., Reese, R., Schlegel, N.-J., Shepherd, A., Simon, E., Smith, R. S., Straneo, F., Sun, S., Trusel, L. D., Van Breedam, J., van de Wal, R. S. W., Winkelmann, R., Zhao, C., Zhang, T., and Zwinger, T.: ISMIP6 Antarctica: a multi-model ensemble of the Antarctic ice sheet evolution over the 21st century, *The Cryosphere*, 14, 3033–3070, <https://doi.org/10.5194/tc-14-3033-2020>, 2020.
- Stokes, G.: On the theories of internal friction of fluids in motion, *Trans. Cambridge Philos. Soc.*, 8, 287–305, 1845.
- Sun, S., Cornford, S. L., Moore, J. C., Gladstone, R., and Zhao, L.: Ice shelf fracture parameterization in an ice sheet model, *The Cryosphere*, 11, 2543–2554, <https://doi.org/10.5194/tc-11-2543-2017>, 2017.
- Tsai, V. C., Stewart, A. L., and Thompson, A. F.: Marine ice-sheet profiles and stability under Coulomb basal conditions, *Journal of Glaciology*, 61, 205–215, <https://doi.org/10.3189/2015JoG14J221>, 2015.

- Tulaczyk, S. M., Kamb, B., and Engelhardt, H. F.: Basal Mechanics of Ice Stream B, West Antarctica. I. Till Mechanics, *J. Geophys. Res.*, 105, 463–481, 2000.
- van der Wel, N., Christoffersen, P., and Bougamont, M.: The influence of subglacial hydrology on the flow of Kamb Ice Stream, West Antarctica, *Journal of Geophysical Research: Earth Surface*, 118, 97–110, <https://doi.org/10.1029/2012JF002570>, 2013.
- Van Pelt, W. J. and Oerlemans, J.: Numerical simulations of cyclic behaviour in the Parallel Ice Sheet Model (PISM), *Journal of Glaciology*, 58, 347–360, <https://doi.org/10.3189/2012JoG11J217>, 2012.
- Walder, J. S. and Fowler, A.: Channelized Subglacial Drainage over a Deformable Bed, *J. Glaciol.*, 40, 3–15, 1994.
- Weertman, J.: Effect of a Basal Water Layer on the Dimensions of Ice Sheets, *Journal of Glaciology*, 6, 191–207, <https://doi.org/10.3189/S0022143000019213>, 1966.
- Wilner, J. A., Morlighem, M., and Cheng, G.: Evaluation of four calving laws for Antarctic ice shelves, *The Cryosphere*, 17, 4889–4901, <https://doi.org/10.5194/tc-17-4889-2023>, 2023.
- Winkelmann, R., Martin, M. A., Haseloff, M., Albrecht, T., Bueler, E., Khroulev, C., and Levermann, A.: The Potsdam Parallel Ice Sheet Model (PISM-PIK) Part 1: Model description, *The Cryosphere*, 5, 715–726, 2011.
- Wright, A., Wadham, J., Siegert, M., Luckman, A., Kohler, J., and Nuttall, A.-M.: Modeling the refreezing of meltwater as superimposed ice on a high Arctic glacier: A comparison of approaches, *Journal of Geophysical Research*, 112, <https://doi.org/10.1029/2007JF000818>, 2007.
- Zoet, L. K. and Iverson, N. R.: A slip law for glaciers on deformable beds, *Science*, 368, 76–78, <https://doi.org/10.1126/science.aaz1183>, 2020.